

# Bandwidth coverage of niobium based superconducting tunnel devices

Chris Franciscus Jessica Lodewijk

*Cover:*

(Front) Artist's impression of heterodyne mixing in a superconducting tunnel device. The image is a color-edited scanning electron micrograph of a device, developed in the research of this thesis.

(Back) "Weren't you searching for aliens?" has been a recurring question of family and friends who vaguely remembered that my research had something to do with telescopes and astronomy. However, this thesis describes research into the superconducting detectors that allow astronomers to "look for aliens". Model: Kareltje.

# **Bandwidth coverage of niobium based superconducting tunnel devices**

## **Proefschrift**

ter verkrijging van de graad van doctor  
aan de Technische Universiteit Delft,  
op gezag van de Rector Magnificus prof. dr. ir. J.T. Fokkema,  
voorzitter van het College voor Promoties,  
in het openbaar te verdedigen op maandag 2 februari 2009 om 10.00 uur

door

**Chris Franciscus Jessica LODEWIJK**

natuurkundig ingenieur  
geboren te Hulst.

Dit proefschrift is goedgekeurd door de promotor:

Prof. dr. ir. T. M. Klapwijk

Samenstelling van de promotiecommissie:

Rector Magnificus,	voorzitter
Prof. dr. ir. T. M. Klapwijk	Technische Universiteit Delft, promotor
Prof. dr. ir. L. P. Kouwenhoven	Technische Universiteit Delft
Prof. dr. H. P. Urbach	Technische Universiteit Delft
Prof. dr. W. Wild	ESO & Rijksuniversiteit Groningen
Prof. dr. H. W. Zandbergen	Technische Universiteit Delft
Prof. dr. J. Zmuidzinias	California Institute of Technology, Pasadena, Verenigde Staten
Dr. ir. A. M. Baryshev	SRON & Rijksuniversiteit Groningen
Prof. dr. ir. H. S. J. van der Zant	Technische Universiteit Delft, reservelid



*Published by:* C. F. J. Lodewijk

*Printed by:* Ponsen & Looijen, Wageningen, the Netherlands

An electronic version of this thesis, including color figures, is available at:  
<http://www.library.tudelft.nl/dissertations/>

Casimir PhD Series, Delft-Leiden, 2008-10

ISBN: 978-90-8593-048-8

Copyright © 2008 by C. F. J. Lodewijk

All rights reserved. No part of the material protected by this copyright notice may be reproduced or utilized in any form or by any means, electronic or mechanical, including photocopying, recording, or by any information storage and retrieval system, without written permission from the author.

Printed in the Netherlands.

*Voor mijn ouders, grootouders en Sandra*



# Preface

Yes, finally, it's done. Four and a half years of hard work, until late hours and in weekends, doubts about the right choices or the future in general; but also fun, meeting lots of interesting people, going to conferences in foreign countries, and the rewarding feeling that all the efforts did make a difference.

After finishing my Master's research project in the Quantum Transport (QT) group at Delft University of Technology, in mid 2003, I decided I wasn't ready yet to be molded into a company employee. Instead, I really liked the challenges of designing something, developing a process to realize it, and measuring its properties to analyze the underlying physical processes. Doing a PhD research would be an ideal way to cultivate my needs. But first, to widen my horizon, I arranged a three-month internship at Harvard University in Boston (USA).

The internship at Harvard lived up to my expectations, and after returning to the Netherlands, I started to look for a PhD position, while working temporarily as a research assistant at QT. There, after a tip from my graduation professor Leo Kouwenhoven, I became aware of the interesting research that was being done in the Nanophysics (NF) group of Teun Klapwijk, 'upstairs' at the third floor of the Applied Physics building in Delft. Teun had relocated his group from Groningen to Delft a few years before, but still maintained tight connections with the Groningen department of the SRON Netherlands Institute for Space Research and the Kapteyn Astronomical Institute. Together, they were developing detectors for sub-millimeter astronomical observations: in Delft, from the broader viewpoint of device physicists, in Groningen, as instrument scientists for very well-defined projects, like HIFI (the Heterodyne Instrument for the Far-Infrared) and ALMA (the Atacama Large Millimeter/submillimeter Array).

I soon became very enthusiastic about a project involving the development of SIS junctions for Band 9 of ALMA. Not only did this project have all the facets of research and development that I wanted, but in addition, it was very application-driven: ALMA needed good working detectors. The fact that the application was astronomy-related only increased my enthusiasm. After a few discussions, I convinced Teun to hire me as a PhD student, starting in May 2004. The results of the research in the four years thereafter are described in this Thesis.

Many people have made a contribution to this thesis, directly and indirectly. First of all, I have to thank my promotor, Teun Klapwijk, who was also my daily

supervisor. Thanks to your advise, patience, and profound knowledge, I was able to finish this thesis. Your analysis (of results, reports, or persons) is very critical, but always fair. Also, you never restricted discussions to physics alone; I sincerely hope for you that there is one tunneling experiment that will fail, namely, the one under your house!

The collaboration with ‘Groningen’ has been an important part of the research. In particular, Andrey Baryshev has taught me a lot about modeling of microstriplines, but also about microwaves, heterodyne mixing, and FTS measurements. Your enthusiasm always provided a spark. If it wasn’t for the stubborn regulations of the university, you would have been my co-promotor. Further, I learnt from you that alcohol fits perfectly in a vegetarian diet.

The very next person that I am greatly indebted to, is Tony Zijlstra. Not only did you always make sure that all the cleanroom equipment was up and running, you also participated very actively in the research. All the nice results that have been obtained with AlN tunnel barriers, would not have been possible without your development of the process! Very rightfully, you are the first author of our APL article.

In the first year of my PhD, Matthias Kroug has taught me everything I needed to know about SIS device fabrication. I’m very grateful to have had such a skillful ‘instructor’!

For about two and a half years, Denis Loudkov was part of our ‘SIS team.’ You served partly as my *de facto* supervisor, and we’ve had many useful discussions.

Patricio Mena was an important part of the Band 9 team in Groningen. He has performed many FTS and noise temperature measurements, and he was the driving force behind the sideband-separating mixer development. Congratulations with your assistant-professorship in Chile!

Shaojiang Zhu, you’re getting to know your way around the group and the cleanroom. I wish you lots of success continuing the project!

Gao, you were always prepared to give advise, or have a discussion about, well, anything. Your office was also *the* place to get the proceedings of the ISSTT, of *any* year.

Thanks to Tom de Kruijff and Vasili Sechnikov for preparing the TEM specimens, and Frans Tichelaar for the TEM analysis. Your images helped us better understand our devices!

I have enjoyed discussions in Delft or elsewhere with Sven Rogge, Jaap Caro, Alberto Morpurgo (exchanging insults), Sebastian Goennenwein, Kate Orlova, Franz Czeschka, Jacob Kooi, Akira Endo, Tom Cecil, Shen-Cai Shi, Edward Tong and the late Marc Feldman.

Thanks to Ton Bastein for leading the Nano-Instrumentation ‘flagship,’ Paul Schuddeboom for always being present at the user’s committee meetings, and Wilfried Boland for being, as an astronomer, very appreciative of the work we’re doing in Delft.

I’ve had the pleasure of supervising three students in their graduation-project.

---

Omid Noroozian was a very skillful student, originally from Electrical Engineering. You were always very eager to learn, both in the cleanroom and in the lab. I have no doubts you will have lots of success with the PhD you're pursuing at Caltech! Elfi van Zeijl has done the first FTS measurements in Delft of our devices, and she was always very enthusiastic. You have found a job at TNO, good luck there! Robbert-Jan Dikken was a student from TH Rijswijk, and he successfully build a new FTS setup in Delft. You decided to continue your studies by starting your Master's in Delft. I hope you will be successful there as well!

My fellow PhD students created a great atmosphere to work in, both on an intellectual level as socially: Merlijn Hajenius, Frank Meijer, Monica Craciun, Ruth de Boer, Ruurd Keizer, Hon-Tin Man, Saverio Russo, and Paul Sniijders all have graduated. Further, there are Rami Barends, Gabri Lansbergen, Tarun Bansal, Nathan Vercruyssen, Rik Hortensius, and Alibey Ozturk. Frank was my first roommate, soon followed by Rami, and for a while also Gabri (before he 'fled' to another group). Rami, I've always said that sharing a room with you for almost four years *on itself* earned me the right to graduate. Besides that, we've gone to conferences together in Seattle, Pasadena, Göteborg (with the famous "Toyota Picnic incident"), and Chicago (and probably other places), and somehow, you never stopped to annoy me! But, as it seems to happen so often, I'm afraid time will erase the bad memories, and only the good will remain. That will be an interesting experience! Gabri (ja, m'n boekje is af!), you were always ready for some 'klemmen.' Speaking of which, I really enjoyed the Oktoberfest-trip to Munich, together with Gabri, Rami, Tarun and Nathan, although I would have preferred a little more sleep... Merlijn, we had great adventures with our Ford Mustang convertible in Florida (also a few days together with Jochem), (en ja, ik heb nog steeds nachtmerries over muggen!), and I will never forget how you managed to be just one minute late for that boat-trip in Göteborg!

Apart from PhD students, there were also Master's students Martin, Dagmar, Carlijn, Maurits, Joost, Ivo, Ilona, Omid, Xi, Elfi, Tim, Pieter, Remco, and Amar, and they all contributed to the nice atmosphere and joined on the occasional nights of eating and/or drinking, as well as some of the B.Sc. students.

The supporting staff is there to take away a lot of problems you don't want to be dealing with, and they deserve a lot of credit for that. For the more technical issues, there were (besides Tony, whom I mentioned before,) Ben (help with measurements and dicing), Niels (who was very helpful with the FTS measurements in Delft that Elfi and Robbert-Jan were doing, as well as serving dubiously looking Chinese tea every day), Mascha (thanks for always fixing the bonding machine!), Jan (idem), and Ron in the Physics building, and at DIMES (the 'other side'), Arnold, Anja, Roel, Marc en Marco always had time to give advise. Furthermore, in Groningen, Brian, Ronald, Gerrit, Jan, Leo, Michela, and Jeffrey, thanks for all the advise, especially Ronald about "how to build your own FTS," and the others thanks for mounting and measuring (DC/FTS/noise temperature) tons of devices! For paperwork, booking flights, and financial stuff, Monique, Maria,

Daphne, Kristel and Irma were there to help us out, as well as for creating a nice atmosphere in the group.

Fortunately, my life didn't end at the doors of the Physics building. I thank my 'Huischgenoten' at the DGW37, originally Bart, Christian, Marnix and Mathijs, but also the older and newer ones: Pepijn, Michiel, Mark, Martin, Freek, Joost and Sanne, for the nice atmosphere after working hours, and the many trips going sailing, skiing or just visiting an old roommate. I'm also glad I got to know Marieke, Monica, and Yohana. Pepijn, you're always available to go for a drink in Delft!

I thank my volleyball teammates of Ariston H1 (Christian, Marco, Mark, Pepijn, Serge, Sidney, and Tjaard) and H2 (Aleks, Erik, Frank, Paul, Roelof, Sander, Thomas, and Willem), at the beginning of this season transformed into Kratos '08 H5, for the sporty challenges and good times in general.

Further, I am grateful to have a huge amount of friends from my 'old town' Hulst, and former volleyball club Morres. Most of us are now living all over the Netherlands, and we see each other much less than I would like. Ivo, Freek (both "Heren 2 Middenmannen"), Jos, Guus, Ewout, Frank, Marc, Martin, Evert-Jan, Jeremy, Ca(rolien), Marieke, Linda, Marjolein, Wendy, Kim, and everybody I forget to mention, the presence of just *a few* of you was always enough to have a great time, anywhere, whether it was in Mallorca, Turkey, at Nature One, Peelpush, during Carnaval, or just somewhere on the Tour de Hollandia!

Nothing in my life would have been possible without the unconditional love and support of my parents, Louise and Roger. Bedankt voor alles! I also would like to thank the rest of my family, and especially my grandparents, for continuously supporting me.

The last person I would like to thank, is the most important person in my life. Sandra, thank you for your love, you give purpose to my life. Thanks for always being able to cheer me up and for your endless understanding. Ik hou van je.

Chris Lodewijk  
December 2008

# Contents

<b>1</b>	<b>Introduction</b>	<b>1</b>
1.1	Sub-millimeter observations . . . . .	2
1.2	Band 9 of ALMA . . . . .	3
1.3	SIS junctions . . . . .	4
1.4	Outline of this Thesis . . . . .	6
	References . . . . .	7
<b>2</b>	<b>Heterodyne mixing with superconducting tunneljunctions</b>	<b>9</b>
2.1	Superconductivity and tunneljunctions . . . . .	10
2.1.1	Superconductivity . . . . .	11
2.1.2	Superconductivity under influence of high frequency radiation	16
2.1.3	Superconducting tunneljunctions . . . . .	18
2.1.4	Response to external radiation . . . . .	27
2.2	Coupling applied radiation to a tunneljunction . . . . .	30
2.2.1	Schematic representation . . . . .	30
2.2.2	AC and DC (quantum) tunneling currents . . . . .	31
2.2.3	Matching of embedding impedence to junction impedance . . . . .	32
2.3	Mixing process and noise temperature . . . . .	34
2.3.1	Direct response of a tunneljunction . . . . .	34
2.3.2	Mixer properties and gain . . . . .	36
2.3.3	Noise contribution of the mixing element . . . . .	39
2.3.4	Sideband separating . . . . .	41
2.4	Conclusion . . . . .	42
	References . . . . .	43
<b>3</b>	<b>Requirements for tunneljunctions based on ALMA Band 9 (602 - 720 GHz)</b>	<b>45</b>
3.1	Choice of Band 9 . . . . .	46
3.2	ALMA Band 9 specifications . . . . .	47
3.2.1	Description of Band 9 Cartridge . . . . .	48
3.2.2	General requirements . . . . .	48
3.2.3	Functional requirements . . . . .	49

3.2.4	Performance requirements . . . . .	49
3.3	Motivation for bandwidth requirements . . . . .	50
3.3.1	Water absorption: atmospheric window . . . . .	50
3.3.2	Astronomically important spectral lines . . . . .	50
3.3.3	Bandwidth analysis . . . . .	51
3.4	Motivation for noise temperature requirements . . . . .	54
3.4.1	Integration time . . . . .	54
3.4.2	Flux density sensitivity . . . . .	55
3.4.3	Noise temperature and device properties . . . . .	56
3.5	Conclusion . . . . .	58
	References . . . . .	58
<b>4</b>	<b>Niobium technology</b>	<b>61</b>
4.1	Device layout . . . . .	62
4.2	Motivation for choice of materials . . . . .	63
4.2.1	Substrate: quartz . . . . .	63
4.2.2	Junction electrodes: niobium . . . . .	64
4.2.3	Microstripline: Nb - SiO <sub>2</sub> - Nb . . . . .	65
4.2.4	Contact pads: gold . . . . .	67
4.2.5	Considerations for other materials . . . . .	68
4.3	Fabrication process . . . . .	69
4.3.1	Substrate preparation . . . . .	69
4.3.2	Ground plane definition . . . . .	70
4.3.3	Junction definition . . . . .	72
4.3.4	Dielectric layer . . . . .	73
4.3.5	Topwire and contact pads . . . . .	75
4.4	Final remarks . . . . .	77
	References . . . . .	78
<b>5</b>	<b>From aluminum oxide to aluminum nitride tunnel barriers</b>	<b>83</b>
5.1	Tunnel barriers in SIS junctions . . . . .	84
5.1.1	The importance of transparent tunnel barriers . . . . .	84
5.1.2	The uniformity of tunnel barriers . . . . .	85
5.2	Realization of tunnel barriers for SIS mixers . . . . .	88
5.2.1	AlO <sub>x</sub> tunnel barriers . . . . .	89
5.2.2	Previous work on AlN tunnel barriers . . . . .	89
5.2.3	AlN tunnel barriers in this work . . . . .	91
	References . . . . .	94
<b>6</b>	<b>Optimizing superconducting matching circuits for Nb SIS mixers operating around the gap frequency</b>	<b>99</b>
6.1	Introduction . . . . .	100

---

6.2	Matching circuit model and antenna impedance . . . . .	100
6.3	Materials and devices . . . . .	104
6.4	Test results . . . . .	106
6.5	Conclusions and discussion . . . . .	107
	References . . . . .	108
<b>7</b>	<b>Epitaxial aluminum-nitride tunnel barriers grown by nitridation with a plasma source</b>	<b>111</b>
7.1	Introduction . . . . .	112
7.2	Uniformity of tunnel barriers . . . . .	112
7.3	Barrier realization procedure . . . . .	113
7.4	Reproducibility of results . . . . .	113
7.5	Analysis of barrier uniformity . . . . .	115
7.6	Conclusion . . . . .	117
	References . . . . .	117
<b>8</b>	<b>Bandwidth limitations of Nb/AlN/Nb SIS mixers around 700 GHz</b>	<b>121</b>
8.1	Introduction . . . . .	122
8.2	Properties of Nb microstriplines . . . . .	123
8.3	Bandwidth of SIS mixers . . . . .	124
8.4	Bandwidth evaluation . . . . .	127
8.5	Noise temperature . . . . .	129
8.6	Conclusion . . . . .	130
8.7	Final remarks . . . . .	131
	References . . . . .	131
	<b>Summary</b>	<b>135</b>
	<b>Samenvatting</b>	<b>139</b>
	<b>Curriculum Vitae</b>	<b>143</b>
	<b>List of refereed publications</b>	<b>145</b>
	<b>List of conference papers</b>	<b>147</b>



# Chapter 1

## Introduction

When his father asks him where he is coming from, after arriving at home very late at night, the Dutch comedian Hans Teeuwen counters: “Where are we coming from, where are we going to, what kind of questions are those, in the middle of the night?” [1]. You see, even an absurdist Dutch comedian considers the origin (and fate) of mankind not to be explained lightly. On the other hand, from early history people from all over the world have always been very much interested in the first of those questions: “Where are we coming from?” and more specifically, what is the origin of our universe? With the aid of astronomy and astrophysics, this becomes: How did the universe form, and how did the early universe evolve? How did the stars form? How did planetary systems form and evolve?

## 1.1 Sub-millimeter observations

The answers we are looking for, can be found in the presence of certain molecular compounds in early stars and planetary systems. This presence can be investigated by looking at electromagnetic radiation that comes from the vibrational and rotational transitions of specific molecules. When a molecule ‘jumps’ to a lower lying energy state, it emits a photon that contains an energy equal to the difference between the two states. Because this difference is very well defined, the emission line in the electromagnetic spectrum is very sharp and bright.

Photons, or electromagnetic radiation in general, can be associated with a frequency. The emission lines from far-away planets and stars we want to observe have frequencies that typically run from 100 GHz to a few THz. This part of the spectrum is usually called the ‘far-infrared,’ or also ‘sub-millimeter.’ The latter because of the wavelength of the radiation in vacuum, which is smaller than 1 mm for frequencies larger than 300 GHz. For comparison, radiation that can be detected by the human eye - visible light - has a wavelength between 400 and 700 nm, roughly a factor 2000 smaller.

If we are standing on the surface of the earth and we are looking at planets and stars, which are beyond the atmosphere, radiation has to pass a large column of air before it reaches us. For visible light, this is not a big problem, as we can see some stars even with our naked eye. But if we want to observe objects from outer space in the far-infrared, we will suffer from this large column of air, because there is a large amount of water in it. Water has all kinds of vibrational and rotational absorption lines located at various frequencies in the far-infrared. As a result, the atmosphere is opaque for a large part of the far-infrared spectrum. Consequently, if we want to do sub-millimeter observations, we have to come up with a ‘trick.’

Obviously, the best trick to overcome the opaqueness of the atmosphere, is to get out of that atmosphere! Preparations are in the final stage to perform sub-millimeter observations from a satellite in orbit around the earth. For example, the Heterodyne Instrument for the Far-Infrared (HIFI) [2, 3] is one of the three

instruments that will be mounted on the Herschel Space Observatory satellite, which is currently planned to be carried into space early 2009 [4]. But, there are also many disadvantages to space based observations, such as the high costs and risks of launching a satellite, the limited lifetime of the instrument after launch and the impossibility of repairing or upgrading the instrument. Further, the spatial resolution of astronomical observations is determined by the number and the size of telescope dishes, both limited for space observations due to the high costs of launching.

Another trick is to stay on the ground, but be very careful at which location the observations are performed. This means that a place has to be found that has as little water as possible in the air above it. Dry places - that is, with a low humidity of the air - are therefore a good candidate, but also high altitude places, because they simply have less air, and thus also less water, above them. The amount of water that is contained in the atmosphere above a certain place is quantified by the precipitable water vapor (*pwv*), which is the depth of the water, if it all condenses from the atmosphere. Taking out spatial and temporal variations, the average *pwv* on earth is about 25 mm [5]. But, there are also locations that combine dryness with high altitude, resulting at times in a *pwv* down to 1 mm.

One of these places is the Atacama Desert in Chile, South-America. It owes its dryness to the mountains that surround it, shielding it from almost all rainfall. Combined with a high altitude, this results in a nearly negligible amount of water in the atmosphere. For this reason, the region has drawn the attention of the astronomical community. For example, the European Southern Observatory (ESO) has its Very Large Telescope (VLT) array on the top of the Cerro Paranal mountain (2635 m). But even Atacama has different levels of 'dryness': its most extreme place is the Llano de Chajnantor, a plateau in the Atacama desert at about 5000 m above sea level, where the *average* precipitable water vapor column is around 2 mm and in wintertime the *pwv* is often lower than 1 mm [6].

## 1.2 Band 9 of ALMA

To finally be able to answer many of the questions about the origin and evolution of the early universe, a huge research instrument is being developed: the Atacama Large Millimeter/submillimeter Array (ALMA) [7, 8]. The project to build this instrument involves the collaboration of Europe, the USA and Japan to construct up to 80 telescopes, most of them with a 12 m diameter, that can be used as an interferometer, permitting high spatial resolution imaging of objects far away. ALMA will allow for spectroscopy measurements, so that, with interferometry, the local distribution of specific frequency sources at stars or planets can be investigated. Both by its over-a-billion dollar budget and by its scientific importance, it is the biggest ground based astronomy project in history. An

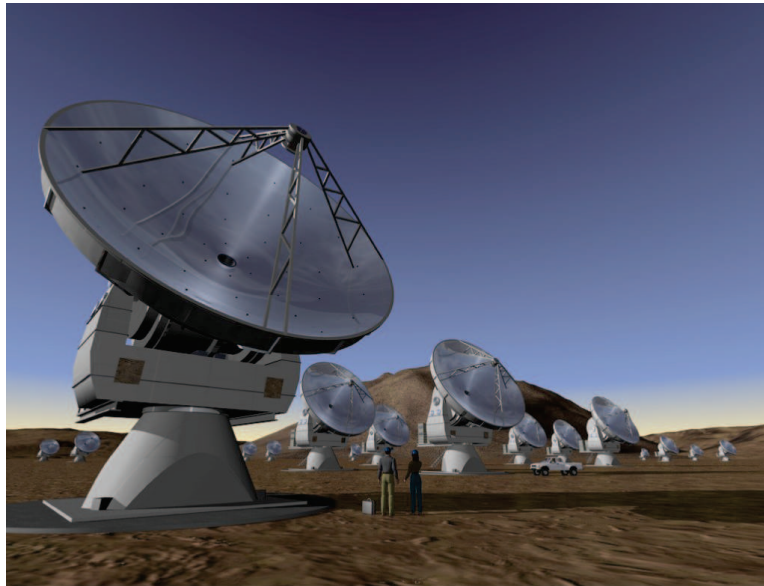


**Figure 1.1:** Artist's impression of future ALMA telescopes.

artist's impression of ALMA is shown in Fig. 1.1.

In spite of the excellent conditions, the atmosphere above the Llano de Chajnantor is still not completely transparent. At some frequencies, water absorption is so strong, that even the slightest bit of water in the air blanks almost all radiation. Therefore, the wide range of frequencies that will be studied by ALMA, 30 to 950 GHz, has been divided into 10 smaller bands, determined by the windows in the atmospheric transmission. An overview of these bands is given in Fig. 1.2. In this work, we have focused on Band 9 of ALMA, which runs from 602 GHz to 720 GHz. Via a joint discussion of Dutch astronomers and instrument scientists, coordinated through the Dutch Research School for Astronomy (NOVA), it has been selected as the best fit between the Dutch astronomical agenda and the Dutch instrument science. Choosing Band 9 would allow 'early' science for the Dutch astronomers. More detailed technological and scientific reasons behind the choice of this band will be explained in Section 3.1.

### 1.3 SIS junctions

After determining at which frequencies we want to observe, with which kind of telescope configuration and what the ideal location for the observatory is, we face one last problem: how to detect sub-millimeter radiation? To solve this problem, the fields of astronomy, optics, microwave engineering and nanotechnology join forces. After the astronomical signal is captured by the telescope's mirror, it is transferred by keen optical and microwave engineering to a chip which contains

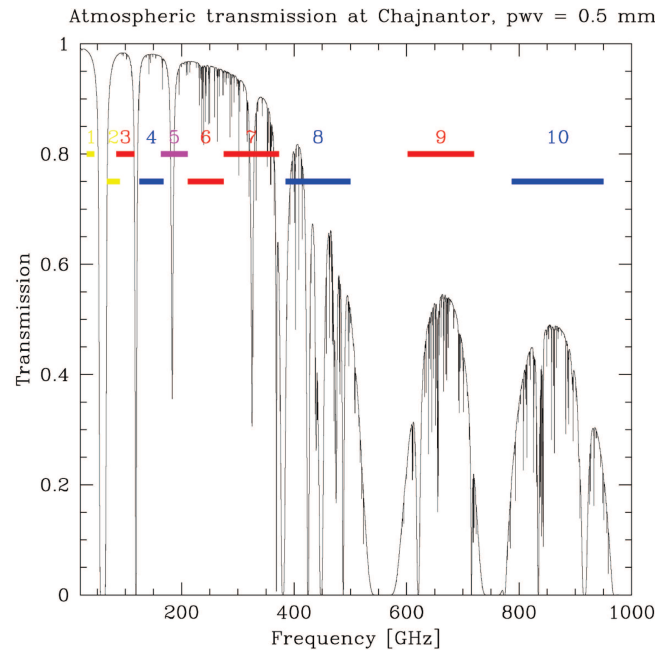


**Figure 1.2:** Atmospheric transmission at the Llano de Chajnantor plateau (the future ALMA site) for a precipitable water vapor (pwv) of 0.5 mm (full line). Bars with numbers indicate the different bands of ALMA: Band 1 (31.3 - 45.0 GHz), 2 (67 - 90 GHz), 3 (84 - 116 GHz), 4 (125 - 163 GHz), 5 (163 - 211 GHz), 6 (211 - 275 GHz), 7 (275 - 373 GHz), 8 (385 - 500 GHz), 9 (602 - 720 GHz), and 10 (787 - 950 GHz). The bands 3, 6, 7, and 9 are the bands with the highest priority, which will be developed before the others. One of these high priority bands is Band 9, the frequency band of this work.

the most essential part of the set-up: the detector. This detector relies on a circa 1 nanometer thick insulating layer, making its fabrication truly *nanotechnology*.

In fact, the main part of the sub-millimeter detector constitutes a superconductor-insulator-superconductor (SIS) junction, which combines two important concepts of physics: quantummechanical tunneling and superconductivity. Moreover, the SIS junction is used as a heterodyne mixer, which transfers the detailed spectroscopic information from a high frequency to a much lower, manageable frequency. In this Thesis, we study the development both of SIS junctions and their application for ALMA Band 9. In particular, we focus on the development of SIS junctions that can be used as heterodyne mixers with a high sensitivity over a wide frequency range around Band 9. Astronomical observations for an exploratory project (called Atacama Pathfinder Experiment, APEX) near the future site of ALMA, obtained with SIS junctions that have been developed in the research of this Thesis, are shown in Fig. 1.3.

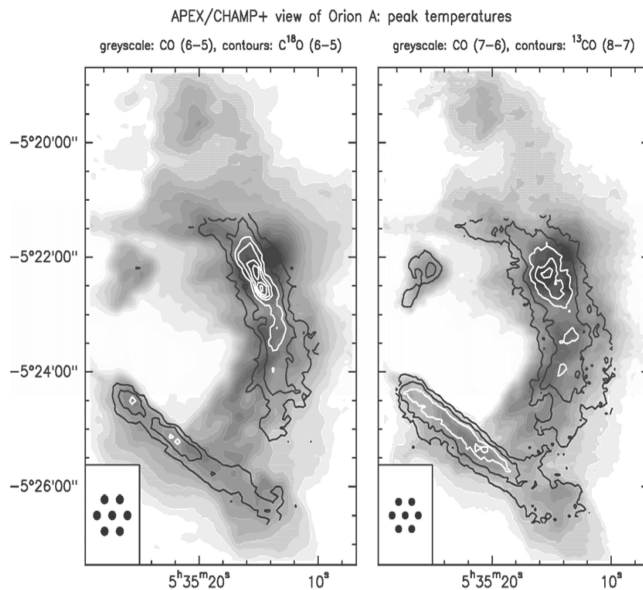


**Figure 1.3:** Emission of warm gas in the Orion A Molecular Cloud, observed with the Carbon Heterodyne Array of the Max Planck Institute (CHAMP+) on the Atacama Pathfinder Experiment (APEX) at a frequency of 691 GHz (left panel), obtained with SIS junctions developed in the research described in this Thesis, and at 806 GHz (right panel). Data are taken on-the-fly, with fast (1 Hz) sampling. One image is composed of about  $700 \times 10^3$  spectra. Courtesy R. Güsten, Max Planck Institute for Radioastronomy, Bonn, Germany, reproduced from Ref. [9]

## 1.4 Outline of this Thesis

This work uses the basic principles of superconductivity and quantummechanical tunneling. In Chapter 2, we will explain what a superconductor is and how tunneling works. Also in Chapter 2, it will be made clear how an SIS junction is used as a heterodyne mixer to detect the astronomical signal. In Chapter 3, the motivation for the requirements of ALMA Band 9, relevant for this work, is given.

In Chapter 4 the technological aspect is addressed: the on-chip realization of the SIS *device*. Chapter 4 will reason the choice of materials, superconducting and dielectric, and explain the practical details of device fabrication. In Chapter 5, it is explained how the standard technology of aluminum oxide tunnel barriers has been replaced by aluminum nitride barriers.

Chapter 6 presents a theoretical and experimental analysis of the optimization of superconducting tuning circuits for SIS detectors. In Chapter 7, it is argued that we can grow epitaxial AlN tunnel barriers by plasma nitridation with a remote plasma source. These AlN tunnel barriers have been applied in real devices and show very promising results, presented in Chapter 8 together with a

critical analysis of the limiting factors to the bandwidth of SIS devices.

The reader of this Thesis will not find out where he or she came from, but we will explain how we have contributed to the development of heterodyne SIS detectors that allow us to answer that question (in a more general context) in the future.

## References

- [1] Translated from: H. Teeuwen, *Dat dan weer wel*, Hummelinck Stuurman Producties, The Netherlands (2002).
- [2] T. de Graauw and F. P. Helmich, “Herschel-HIFI: The heterodyne instrument for the far infrared”, in *SP-460 The promise of the Herschel Space Observatory*, Eds. G. L. Pilbratt, J. Cernicharo, A. M. Heras, T. Prusti, and R. A. Harris, Noordwijk, The Netherlands: ESA Pub. Div., 45 (2001).
- [3] Website: <http://www.sron.nl/divisions/lea/hifi/>
- [4] Website: <http://sci.esa.int/science-e/www/object/index.cfm?fobjectid=34695>
- [5] D. L. Randel, T. H. Vonder Haar, M. A. Ringerud, G. L. Stephens, T. J. Greenwald, and C. L. Combs, “A new global water vapor dataset”, *Bull. Am. Meteorological Soc.*, Vol. **77**, 1233 (1996).
- [6] R. Bustos, G. Delgado, L.-Å. Nyman, and S. Radford, “52 years of climatological data for the Chajnantor area”, *ALMA Memo 333* (2000). A list of ALMA Memos can be found at the website: <http://www.alma.nrao.edu/memos/index.html>
- [7] A. Wootten, “The Atacama Large Millimeter Array (ALMA)”, online: <http://arxiv.org/abs/astro-ph/0209630> (2002).
- [8] J. Kanipe, “High and dry”, *Nature*, Vol. **439**, 526 (2006).
- [9] R. Güsten, *et al.*, “Submillimeter heterodyne arrays for APEX”, accepted for the Proceedings of the SPIE Conference on Astronomical Instrumentation (2008).



## Chapter 2

# Heterodyne mixing with superconducting tunneljunctions

The purpose of the superconducting tunneljunctions, which are the subject of this research, is to investigate the frequency spectrum of astronomical objects. These SIS junctions are part of an ALMA receiver that has been designed for the frequency range of Band 9: 602 to 720 GHz. The astronomical signals are detected by operating the SIS junction as a heterodyne mixer. Mixing is a process which occurs when radiation of different frequencies is absorbed by a device with a non-linear current-voltage characteristic, in our case the SIS junction. If this happens, the output of the device will consist of signals having frequency components which are the sums and differences of the incoming frequencies, and their multiples.

Using the principle of heterodyne mixing, a signal from the sky can be combined with a signal with a known frequency, called the local oscillator (LO). This combination is then led to the detector, which produces the difference and sum signals. If a low pass filter is used, only the difference signal will be left. This signal is called the Intermediate Frequency (IF) signal. The IF signal still contains all the information from the original astronomical signal, but it is ‘downconverted’ in frequency. This lower frequency signal can be amplified and processed, in other words, it allows the original signal to be detected.

How well such a receiver performs, depends on the amount of noise it produces, which can be represented by the (receiver) noise temperature,  $T_n$  or  $T_{rec}$ . The lower  $T_n$ , the better the performance of the receiver. We use SIS junctions as heterodyne mixers, because of their low noise properties: the current-voltage characteristic of an SIS junction is ‘very’ non-linear and it allows the use of low loss superconducting electrodes.

In this chapter, we will explain what superconductivity and quantummechanical tunneling are, how they are combined in SIS junctions, and what the effect of external radiation is (Section 2.1). Furthermore, the coupling of applied radiation to a tunneljunction will be explained (Sect. 2.2) and finally we will go into the explanation of the actual mixer process and the noise temperature (Sect. 2.3).

## 2.1 Superconductivity and tunneljunctions

In 1908, the Dutch scientist Heike Kamerlingh Onnes was the first to liquify helium-4. A few years later, in 1911, he was studying the resistance of solid mercury at cryogenic temperatures, using liquid helium as a refrigerant, when he found that this resistance instantly vanished below a temperature of 4.2 K, the boiling point of helium. This phenomenon has become known as *superconductivity*. Over the years, lots of other materials, both elements and compounds, have been found to be superconducting below a specific temperature, called the critical temperature ( $T_c$ ).

Quantum tunneling is a process in which a particle can penetrate a potential barrier with a higher energy than its own. In classical mechanics, this is not possible, and total reflection (or zero transmission) at the barrier is predicted.

In quantum mechanics on the other hand, a particle is described by a wave function and its behavior by the Schrödinger equation, which allows a nonzero transmission of the barrier.

In this Section, we will give a more detailed introduction of superconductivity in the context of this work. We will also discuss quantummechanical tunneling and how these two are combined in superconducting tunneljunctions. In view of the application of SIS junctions for detection of astronomical signals, we will explain the influence of external radiation on both superconductors in general and SIS junctions in particular.

### 2.1.1 Superconductivity

Superconductivity is characterized by the complete disappearance of the electrical resistance of a material when it is cooled below its critical temperature  $T_c$ . Superconductivity is caused by a small attractive force between free electrons in a metal. In a conventional, low  $T_c$  superconductor (LTS), this attractive force is controlled by electron-phonon interaction. When a metal becomes superconducting, electrons form pairs with opposite spin and momentum, called Cooper pairs. The paired electrons create a superconducting condensate, with many Cooper pairs in one macroscopic quantum state. The distance over which these pairs are correlated is called the coherence length  $\xi$ . Because  $\xi$  is much larger than the average distance between the electrons in the condensate, one Cooper pair overlaps many others, creating one correlated state over the whole metal. The single ground state where all Cooper pairs are condensed into is situated at the Fermi energy ( $E_F$ ). In this ground state, the pairs transport electrical charge without dissipation of energy. A detailed microscopic theory has been formulated by Bardeen, Cooper and Schrieffer [1] and is usually called the BCS theory.

The minimum excitation energy to break a Cooper pair into two separate ‘quasiparticles’ is the superconducting gap energy  $2\Delta$ , where  $\Delta$  is the energy per excitation. Excitations are deliberately called *quasiparticles* here, instead of ‘electrons,’ because they are in a superconductor always in an excited state, and over time they will pair up to decay into the ground state Cooper pairs. The superconducting gap is also apparent from the density of excited states, or quasiparticle density of states  $N_s$ .  $N_s$  can be written as

$$\frac{N_s(E)}{N(0)} = \begin{cases} \frac{E}{\sqrt{E^2 - \Delta^2}} & (|E| > \Delta) \\ 0 & (|E| < \Delta), \end{cases} \quad (2.1)$$

where  $E$  is the energy relative to  $E_F$ , and  $N(0)$  is the normal state density of states at  $E_F$ . This equation shows that  $N_s$  is zero in superconductors at the Fermi level ( $E = 0$ ), where the Cooper pairs are; for increasing  $E$ , it remains zero below  $\Delta$ , shooting up to infinity at  $E = \Delta$ , and from there going down

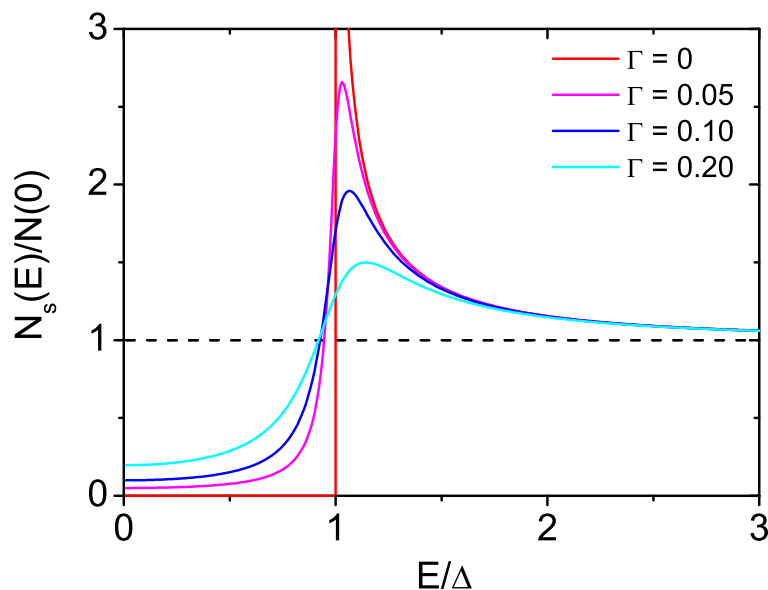


**Figure 2.1:** Density of states in the superconducting (full lines) compared to the normal (dashed line) state, for different quasiparticle-lifetime broadening parameters  $\Gamma$  [2]. The curve for  $\Gamma = 0$  shows the BCS density of states.

towards  $N(0)$  at  $E \gg \Delta$ . The behavior of Eq. 2.1 is illustrated in Fig. 2.1 with the  $\Gamma = 0$  curve.

If one takes into account the finite recombination time for two quasiparticle excitations to recombine into a Cooper pair, a broadening parameter  $\Gamma$  can be introduced to add an imaginary part to the energy [2]:

$$\frac{N_s(E, \Gamma)}{N(0)} = \Re \left\{ \frac{E - i\Gamma}{\sqrt{(E - i\Gamma)^2 - \Delta^2}} \right\}. \quad (2.2)$$

As a result,  $N_s$  will not have a singularity at  $E = \Delta$ , but instead a finite maximum. This is illustrated in Fig. 2.1 for various values of  $\Gamma$ .

The quasiparticle density of states can be probed by superconductor - superconductor tunneling, as in an SIS. The infinite density of states at  $E = \Delta$  causes a non-linearity in the current-voltage characteristic, which makes it perfectly suitable for use as a heterodyne mixer. We will discuss this in detail in Subsection 2.1.3 and further in Section 2.3.

Superconductivity is most renowned for the perfect conductivity it shows, which exists only below a critical temperature,  $T_c$ . Another characteristic is perfect *diamagnetism* for bulk superconductors: a magnetic field is both excluded from entering a superconductor and expelled from a superconductor as it is cooled through  $T_c$ . This is the reversible Meissner effect, after its discoverer Meissner [3].

An applied magnetic field does not disappear sharply at the edge of a superconductor, but is screened exponentially with a typical length that is called penetration depth,  $\lambda$ .  $\lambda$  is minimum at zero temperature, and diverges towards infinity if  $T$  approaches  $T_c$ . The theoretical limiting value for the penetration depth for a pure superconductor with local electrodynamics is called the *London* penetration depth,  $\lambda_L$ . A superconductor is in the local limit when  $\lambda > \xi$ , meaning that the current density  $\mathbf{j}(\mathbf{r})$  at a location  $\mathbf{r}$  in the superconductor is proportional to the vector potential  $\mathbf{A}(\mathbf{r})$  at that same spot. Whether a superconductor is pure or ‘dirty’ depends on the mean free path  $\ell$ : a dirty superconductor has a short  $\ell$ , whereas a pure superconductor has a long  $\ell$ .

The penetration of a superconductor by a magnetic field depends on the ratio between  $\lambda$  and  $\xi$ , as we will explain below. The magnitude of  $\lambda$  and  $\xi$  is connected to  $\ell$ , in the Ginzburg-Landau limit of  $T$  close to  $T_c$ :

$$\lambda(T) = \begin{array}{cc} \text{pure} & \text{dirty} \\ \frac{\lambda_L(0)}{\sqrt{2(1-T/T_c)}} & \lambda_L(0) \sqrt{\frac{\xi_0}{2.66\ell(1-T/T_c)}} \end{array} \quad (2.3)$$

$$\xi(T) = \begin{array}{cc} \text{pure} & \text{dirty} \\ 0.74 \frac{\xi_0}{\sqrt{1-T/T_c}} & 0.855 \sqrt{\frac{\xi_0 \ell}{1-T/T_c}} \end{array}. \quad (2.4)$$

The ratio of the penetration depth and the coherence length is called the Ginzburg-Landau (GL) parameter [4]:

$$\kappa = \frac{\lambda}{\xi}. \quad (2.5)$$

For typical pure non-local superconductors, with  $\xi_0 \gg \lambda_L$ , it follows from Eqs. 2.3 and 2.4 that  $\kappa \ll 1$ . In this case, the superconductor is called a *type I superconductor*. The Meissner effect was observed in this type of superconductors, and it implies the existence of a certain magnetic field, above which superconductivity will be destroyed, because it becomes thermodynamically less favorable. The field is called the (thermodynamic) critical magnetic field  $H_c$ .  $H_c$  is dependent on temperature  $T$ , according to the empirically found relation

$$H_c(T) \approx H_c(0)(1 - (T/T_c)^2), \quad (2.6)$$

which is visualized in Fig. 2.2. This Figure can be interpreted as a phase diagram: in the region below the curve, the metal is in the superconducting state, outside, it is normal.

On the other hand, we can also consider superconductors that have a large  $\kappa$ , which corresponds to  $\xi < \lambda$ , a superconductor in the local limit. A dirty superconductor is by definition in the local limit, but also a pure superconductor can be local because of its material parameters. For temperatures very near  $T_c$ , when

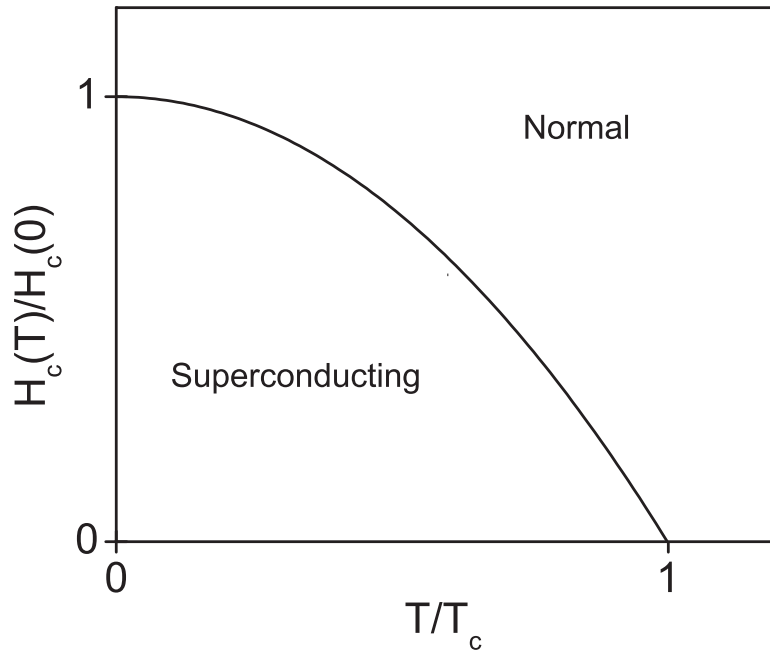


**Figure 2.2:** Thermodynamic critical magnetic field of a type I superconductor as a function of temperature.

$\lambda$  increases to infinity, all superconductors become local. If  $\kappa > 1/\sqrt{2}$ , a superconductor is called a *type II superconductor*, following Abrikosov [5]. In this type of superconductors, instead of an instantaneous breakdown of superconductivity at a critical magnetic field  $H_c$ , there is a continuous increase in magnetic flux penetration, starting at a lower critical field  $H_{c1}$  and reaching the externally applied value at an upper critical field  $H_{c2}$ . This flux penetration is possible because of the entrance of Abrikosov vortices into the superconductor at  $H_{c1}$ . Such vortices can be interpreted as small supercurrents circulating around quasi-normal cores at their center, each carrying a quantum of flux  $\Phi_0 = h/2e$ .

Type I superconductors are usually metal elements, such as aluminum (Al), tin (Sn) or lead (Pb). Type II superconductors are predominantly metal alloys, like niobium titanium (NbTi) or magnesium carbon nickel ( $\text{MgCNi}_3$ ) and high  $T_c$  superconductor (HTS) ceramics, such as yttrium barium copper oxide (YBCO). Only a few elements are a type II superconductor, and one of them is niobium (Nb), the superconductor that is being used in this work. Further, most thin superconducting films are type II superconductors, if one takes into account an effective perpendicular penetration depth  $\lambda_{\perp}$  defined as

$$\lambda_{\perp} = \frac{\lambda^2}{d}, \quad (2.7)$$

where  $d$  is the film thickness.

Also  $\Delta$  depends on temperature, with its maximum value  $\Delta(0)$  at  $T = 0$  and

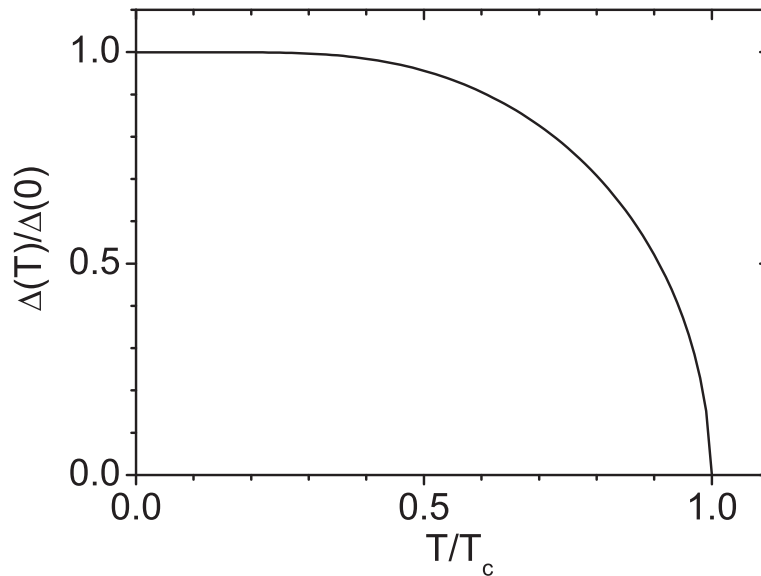


**Figure 2.3:** Numerical calculation of gap energy  $\Delta(T)$  as a function of temperature, normalized to  $\Delta(0)$  and  $T_c$ , respectively.

decreasing to zero at  $T = T_c$ . This dependence can be calculated numerically with the BCS theory, using the relation

$$\frac{1}{N(0)\beta} = \int_0^{\hbar\omega_c} \frac{\tanh[\sqrt{\epsilon^2 + \Delta^2}/2k_B T]}{\sqrt{\epsilon^2 + \Delta^2}} d\epsilon, \quad (2.8)$$

where  $\epsilon$  is the excitation energy over which the integral runs,  $k_B$  is Boltzmann's constant,  $\hbar$  is Planck's constant  $h$  divided by  $2\pi$ ,  $\beta$  is a constant representing the electron-phonon interaction, and  $\omega_c$  is the cutoff (angular) frequency of this interaction potential (which is of the order of the phonon spectrum cutoff frequency, corresponding to the Debye energy). From this relation, also the theoretical BCS ratio between  $\Delta(0)$  and  $T_c$  can be found:

$$\Delta(0) = 1.764k_B T_c. \quad (2.9)$$

The numerically computed temperature dependence of  $\Delta$  (from Eq. 2.8) is shown in Fig. 2.3.

A very good introduction to superconductivity is given in the book by Tinkham [6]. Here, we have given a short, qualitative explanation for superconductivity in the context of this thesis. We have introduced the quasiparticle density of states, which determines the electric behavior of SIS junctions. Further, we have shown the difference in magnetic field dependence between type I and type II superconductors. The latter are used in this work.

### 2.1.2 Superconductivity under influence of high frequency radiation

Detectors based on SIS junctions use the tunnel process itself as a detection principle (Section 2.3). However, losses may occur by absorption of radiation in the superconducting films that connect them.

The first experimental work in this subject area of superconductivity has been done by Glover and Tinkham [7], who were the first to show the superconducting energy gap with far-infrared absorption measurements on superconductors. Mattis and Bardeen [8] theoretically derived expressions for the complex conductivity  $\sigma = \sigma_1 - i\sigma_2$ , as defined by Glover and Tinkham [9], normalized to the normal state conductance  $\sigma_n$ :

$$\begin{aligned} \frac{\sigma_1}{\sigma_n} = & \frac{2}{\hbar\omega} \int_{\Delta}^{\infty} dE (f(E) - f(E + \hbar\omega)) \frac{E^2 + \Delta^2 + \hbar\omega E}{\sqrt{E^2 - \Delta^2} \sqrt{(E + \hbar\omega)^2 - \Delta^2}} \\ & + \frac{1}{\hbar\omega} \int_{\Delta}^{\hbar\omega - \Delta} dE (1 - 2f(\hbar\omega - E)) \frac{\hbar\omega - E^2 - \Delta^2}{\sqrt{E^2 - \Delta^2} \sqrt{(\hbar\omega - E)^2 - \Delta^2}}, \end{aligned} \quad (2.10)$$

and

$$\frac{\sigma_2}{\sigma_n} = \frac{1}{\hbar\omega} \int_{\Delta - \hbar\omega, -\Delta}^{\Delta} dE (1 - 2f(E + \hbar\omega)) \frac{E^2 + \Delta^2 + \hbar\omega E}{\sqrt{E^2 - \Delta^2} \sqrt{(E + \hbar\omega)^2 - \Delta^2}}, \quad (2.11)$$

where  $\omega$  is the angular frequency of the AC signal or the applied electromagnetic radiation and  $f(E)$  is the Fermi-Dirac distribution function:

$$f(E) = \frac{1}{1 + e^{E/k_B T}}. \quad (2.12)$$

Expressions 2.10 and 2.11 are also applicable to absorption of electromagnetic radiation and were found to be in agreement with the work of Glover and Tinkham [7].

The surface impedance of a conductor  $Z_s(\omega)$  is defined as

$$Z_s(\omega) = \frac{E_x(0, \omega)}{\int_0^{\infty} J_x(z, \omega) dz}, \quad (2.13)$$

where  $E_x(0, \omega)$  is the electric field parallel at the surface of the conductor and  $J_x(z, \omega)$  is the current density in the conductor at a depth  $z$ . This formula is generally applicable to both normal and superconducting metals. For superconductors, the behavior of  $Z_s$  depends on the ratio  $\xi/\lambda_{eff}$ : if  $\xi/\lambda \ll 1$ , the superconductor is said to be in the local (or *dirty*) limit, where current density  $J$  and electric field  $E$  are related according to  $\mathbf{J} = \sigma \mathbf{E}$ , with  $\sigma$  the conductivity.

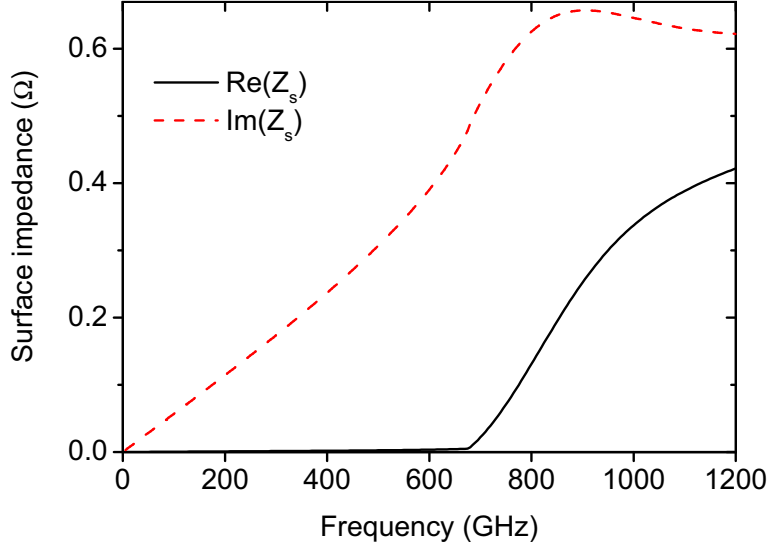


**Figure 2.4:** Real and imaginary part of the surface impedance  $Z_s$  of a layer of Nb with a thickness of 200 nm, normal conductivity of  $2.4 \times 10^7$  S/m and gap energy 2.8 meV, at a temperature of 4.2 K.

If this is the case, Eq. 2.13 can be solved for a superconductor with thickness  $d$  using Maxwell's equations  $\nabla \times \mathbf{E} = -\partial \mathbf{B} / \partial t$  and  $\nabla \times \mathbf{B} = \mu_0(\mathbf{J} + \epsilon_0 \partial \mathbf{E} / \partial t)$ , with  $\mathbf{E}$  the electric field,  $\mathbf{B}$  the magnetic flux density,  $t$  time,  $\mu_0$  the magnetic permeability of free space,  $\mathbf{J}$  the current density and  $\epsilon_0$  the permittivity of free space. If we assume  $E_x(z, \omega) = E_x(z)e^{i\omega t}$  and  $\mathbf{B} = \mathbf{B}_0(z)e^{i\omega t}$  and that the displacement current is negligibly small ( $\omega\epsilon_0 \ll \sigma$ ), this yields:

$$Z_s(\omega) = \sqrt{\frac{i\omega\mu_0}{\sigma}} \coth\left(\sqrt{i\omega\mu_0\sigma d}\right). \quad (2.14)$$

Niobium, the superconductor that is primarily being used in this work, is a type II superconductor, which is in the local limit ( $\xi/\lambda \approx 0.05$  [10]), so Eq. 2.14 applies. In Fig. 2.4, a calculation is shown for a Nb film with a thickness of 200 nm, which is a typically used value. It can clearly be seen that  $\Re\{Z_s\}$ , which represents the surface resistance  $R_s$  (or in other words the losses in the film), is very small for low frequencies, but shoots up at a threshold value. This threshold is the gap frequency  $f_{gap}$ , defined as  $f_{gap} = 2\Delta/h$ , and can be interpreted as the minimum frequency for a photon to break a Cooper pair into two quasiparticles. If we take  $2\Delta=2.8$  meV for Nb,  $f_{gap}$  is about 677 GHz.

The surface impedance will turn out to be important to calculate the transmission efficiency of electromagnetic waves by a superconducting microstripline. This will be addressed in Chapter 6.

### 2.1.3 Superconducting tunneljunctions

The detectors that are being used in this work are superconducting tunnel junctions. We will explain what tunneling is, and discuss some basic properties of STJs.

#### Tunneling

In Quantum Mechanics, a particle is described by its wavefunction and the equation that describes the motion of a particle is called the Schrödinger equation. Its most general time-dependent version reads

$$H\Psi = i\hbar \frac{\partial \Psi}{\partial t}, \quad (2.15)$$

where  $H$  is the Hamiltonian of the particle,  $\Psi$  is its wavefunction, and  $t$  indicates time. The Hamiltonian is a representation of the total energy of the system. The wavefunction is defined such that the square of its absolute value represents the probability density of finding the particle at a given position in space:

$$P_\Omega = \iiint_\Omega |\Psi(x, y, z)|^2 dx dy dz, \quad (2.16)$$

where  $P_\Omega$  is the probability to find the particle in the volume  $\Omega$  and  $x, y, z$  are spatial coordinates.

If we consider a particle in a three dimensional potential landscape, 2.15 becomes

$$-\frac{\hbar^2}{2m} \nabla^2 \Psi + U\Psi = i\hbar \frac{\partial \Psi}{\partial t}, \quad (2.17)$$

where  $m$  is the mass of the particle and  $U$  is a function describing the potential landscape. If the particle, for simplicity, is allowed to move only in one dimension, and we look for stationary solutions, we get

$$-\frac{\hbar^2}{2m} \frac{\partial^2 \Psi(x)}{\partial x^2} + U(x)\Psi = E_0\Psi(x), \quad (2.18)$$

with  $x$  indicating the position along the movement of the particle and  $E_0$  the allowed eigenvalue(s) of the particle energy.

To explain the phenomenon of tunneling in more detail, we will consider a particle with energy  $E_0$ , moving along a potential landscape  $U(x)$ , which is zero for  $x < 0$ , has a fixed value  $U_0$  for  $0 < x < a$ , and is again zero for  $x > a$ , as shown in Fig. 2.5. If the energy barrier height,  $U_0$ , is larger than  $E_0$ , it is classically impossible for a particle entering from the left to penetrate into the region  $x > 0$ , let alone  $x > a$ . Quantummechanically, however, one must solve

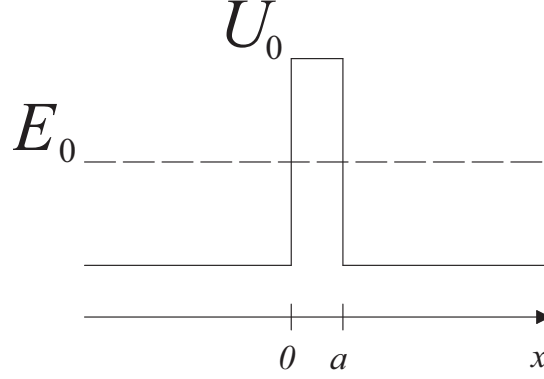


**Figure 2.5:** Potential landscape  $U(x)$  for the tunneling of a particle with energy  $E_0$  through a barrier with thickness  $a$ .

Schrödinger's Eq. 2.18 to find out the behavior of the system. Doing this, we find for  $x < 0$

$$\Psi(x) = C_1 e^{i\frac{\sqrt{2mE_0}}{\hbar}x} + C_2 e^{-i\frac{\sqrt{2mE_0}}{\hbar}x}, \quad (2.19)$$

where  $C_1$  and  $C_2$  are the amplitudes of the wave moving in positive and negative  $x$ -direction, respectively. Solving Eq. 2.18 in the other two regions, we find

$$\Psi(x) = C_3 e^{\frac{\sqrt{2m(U_0-E_0)}}{\hbar}x} + C_4 e^{-\frac{\sqrt{2m(U_0-E_0)}}{\hbar}x} \quad \text{for } 0 < x < a \quad (2.20)$$

$$\Psi(x) = C_5 e^{i\frac{\sqrt{2mE_0}}{\hbar}x} + C_6 e^{-i\frac{\sqrt{2mE_0}}{\hbar}x} \quad \text{for } x > a, \quad (2.21)$$

with the  $C_i$  the amplitudes of the various propagating waves. Note that the exponents in 2.19 and 2.21 are the same. If we now consider again a particle which comes from the left, we can assume that  $C_1 = 1$ , which is the incoming wave,  $C_2 = a_r$ , the reflected wave, and  $C_5 = a_t$ , the transmitted wave.  $C_6 = 0$ , there is no incoming wave from the right. Using these assumptions, we can find expressions for  $a_r$  and  $a_t$  if we apply the boundary conditions for continuity and differentiability of  $\Psi$  at  $x = 0$  and  $x = a$ .

Using Eq. 2.16, we find that  $|a_t|^2$  represents the transmission probability of a particle tunneling through the barrier. Finally, this yields

$$T_P = |a_t|^2 = \frac{1}{1 + \frac{U_0^2 \sinh^2\left(\frac{\sqrt{2m(U_0-E_0)}}{\hbar}a\right)}{4E_0(U_0-E_0)}}, \quad (2.22)$$

where  $T_P$  is the transmission probability. The result 2.22 is nonzero, which shows that a particle can penetrate a barrier, even if its energy is lower. This is called (quantummechanical) tunneling.

If we look at the result 2.22 from the point of view of the tunnel barriers used in this work, we can note a few things. First,  $U_0$  is the band gap or barrier height of the barrier material, typically 6 to 8 eV.  $E_0$  can be interpreted as the Fermi energy  $E_F$ , 5.32 eV for niobium [11]. The barrier thickness  $a$  is about 1 nm, so that  $\frac{\sqrt{2m(U_0-E_0)}}{\hbar}a \gg 1$  and Eq. 2.22 can be written as:

$$T_P = \frac{16E_0(U_0 - E_0)}{U_0^2} \exp\left(-\frac{\sqrt{2m(U_0 - E_0)}}{\hbar}2a\right). \quad (2.23)$$

Taking  $U_0 = 7$  eV, we find  $T_P \approx 5 \times 10^{-6}$ . However, it should be noted that Eq. 2.22 was derived for a one-dimensional, ideal (purely theoretical) system. This has a few very important consequences.

First, in a real tunneling barrier, the system has three dimensions, which makes the barrier thickness ( $a$ ) different if specular tunneling is assumed (where the angle of incidence on the barrier plays a role) or if diffusive tunneling is assumed. As a result, the transmission probability will have to be adjusted.

Secondly, a tunneling barrier is made of an about 1 nanometer thick physical system of stacked atoms. Since 1 nm corresponds to about 5 atoms, the barrier thickness is clearly not a well-defined quantity. Due to the exponential dependence, this has a large effect on the tunneling probability: for example, if we take  $a = 0.8$  nm,  $T_P = 7 \times 10^{-5}$ , if  $a = 1.0$  nm,  $T_P = 5 \times 10^{-6}$ , and if  $a = 1.2$  nm,  $T_P = 4 \times 10^{-7}$ . Further, also the barrier height  $U_0$  is not necessarily constant over the barrier, resulting in a similar variation.

Clearly, the tunneling probability will have a high spatial non-uniformity. This should always be realized when working with devices using a tunneling barrier, like tunneljunctions.

### Characteristics of SIS junctions

Having explained that tunneling *in general* is possible, we will explain the behavior of SIS junctions, where quasiparticles and Cooper pairs can tunnel through the insulating barrier. One can derive the net quasiparticle current through the junction barrier from the so-called Fermi Golden Rule. This Rule is a general approach to calculate the transition rate from one state to the other, which is assumed to be described by a tunneling Hamiltonian. We find for the quasiparticle current  $I_{qp}^0$  as a function of applied voltage  $V$

$$I_{qp}^0(V) = \frac{e}{h} \int_{-\infty}^{\infty} T'_P N_{s1}(E) N_{s2}(E + eV) (f(E) - f(E + eV)) dE, \quad (2.24)$$

where  $e$  is the charge of an electron,  $N_{s1}$  and  $N_{s2}$  are the quasiparticle densities of states of the superconductors on both sides of the barrier, and  $T'_P$  is the transmission probability of Eq. 2.22 for quasiparticles, adjusted to take into

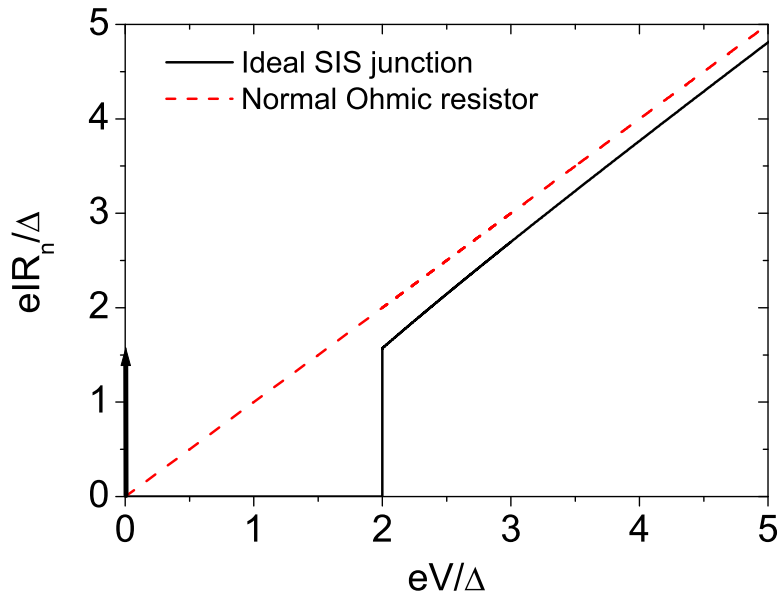


**Figure 2.6:** Current-voltage ( $IV$ ) characteristic of an ideal SIS junction at 0 K, compared with a normal Ohmic resistor, both with normal resistance  $R_n$ . The arrow at  $V = 0$  indicates the maximum of the critical current  $I_c$ .

account the three-dimensional nature and the non-uniformity of the barrier. The subscript ‘0’ of  $I_{qp}^0$  refers to the absence of radiation, here added to avoid confusion in Subsection 2.1.4. For small temperatures and voltages, only the terms around the Fermi level ( $E = 0$ ) are significant. In that case  $T_P'$  can be considered independent of  $E$  and taken out of the integral.

If we use the quasiparticle density of states  $N_s$  of Eq. 2.1 for both superconducting electrodes to calculate the current through an SIS junction at zero temperature, we obtain its ideal  $IV$ -characteristic at 0 K (Fig 2.6).

There are a few requirements for an SIS  $IV$ -characteristic to be ‘ideal.’ First, the higher order tunneling processes, like multiple Andreev reflections (see Chapter 5) are ignored. There are no single-electron energy states for energies  $|E| < \Delta$ . Further, the superconductors at both electrodes have a density of quasiparticle states which is infinite at the edge of the energy gap:  $N_s(|\Delta|) \rightarrow \infty$ . This translates into a broadening parameter  $\Gamma = 0$  (Subsection 2.1.1).

For easier understanding of the SIS  $IV$  characteristic, the ‘semiconductor model’ has been developed. This is illustrated in Fig. 2.7. In the semiconductor model, there is a filled density of states below the superconducting gap, or ‘valence band,’ and an empty density of states beyond the gap, the ‘conduction band.’ Quasiparticles can tunnel through the barrier, which is in the middle, if filled states on one side align horizontally with empty states on the other. The semiconductor model is justified by realizing that for quasiparticles, the tunneling probability is  $(u^2 + v^2)T_P = T_P$ , since  $u^2 + v^2 = 1$ , where  $u$  and  $v$  are the BCS

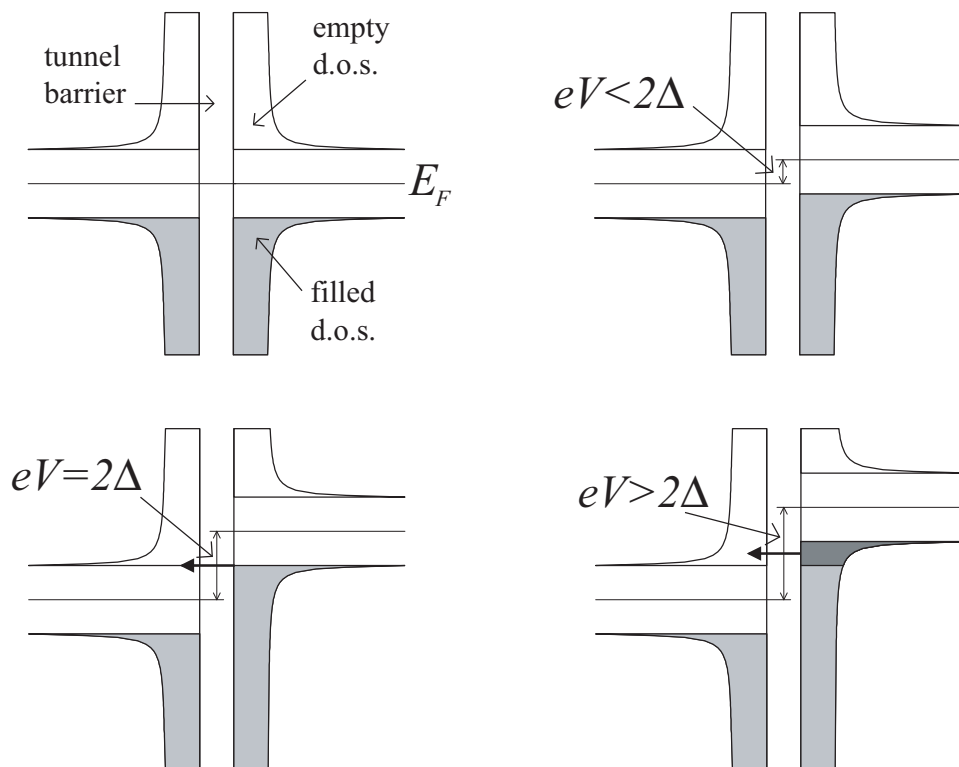


**Figure 2.7:** Quasiparticle tunneling through an SIS junction, explained by the semiconductor model. (Top left) The semiconductor model: gray areas represent filled densities of states (d.o.s.), white areas empty d.o.s. in the two superconductors, which are separated by the tunnel barrier in the middle. The thin lines show the Fermi energy ( $E_F$ ) level in each superconductor. This panel shows the model for a bias voltage  $V = 0$ : both  $E_F$  are aligned. (Top right) For  $eV < 2\Delta$ , no quasiparticle tunneling is possible. (Bottom left) At  $eV = 2\Delta$ , we see the onset of quasiparticle tunneling, indicated by the black arrow. (Bottom right) For  $eV > 2\Delta$ , an increasing number of states becomes available for tunneling, indicated by the darker gray area.

coherence factors.

We will now explain the shape of the 0 K  $IV$  dependence (Fig. 2.6), ignoring for a moment the current at  $V = 0$  (see below), using the semiconductor model for quasiparticle tunneling (Fig. 2.7).

Between  $V = 0$  and  $V = 2\Delta/e$ , illustrated with the semiconductor model in the top right panel of Fig. 2.7, there is no quasiparticle-current, because of the empty density of quasiparticle states in the superconducting gap. Moreover, there are also no occupied states in the conduction band (above the gap) or unoccupied states in the valence band (below the gap) as a consequence of the absence of thermal excitations. At finite temperatures, the current in this regime, often called the subgap current ( $I_{sg}$ ), becomes nonzero.

At  $V = 2\Delta/e$ , referred to as the gap voltage  $V_g$ , there is a finite discontinuity (a ‘jump’) in the current. This can be understood from the bottom left panel of Fig. 2.7, where we see that the densities of states of the two electrodes are now offset in energy with respect to each other such that there are available states for quasiparticles to tunnel into. In fact, the singularity at  $E = \Delta$  results in a filled infinite density of states which aligns with an empty infinite density of states and thus the step-like behavior.

For biases  $V > 2\Delta/e$ , corresponding to the bottom right panel of Fig. 2.7, the current increases with increasing voltage. For a large bias ( $V \gg 2\Delta/e$ ), the number of quasiparticle states that become available for tunneling increases linearly, and hence,  $I$  approaches the normal resistor value  $V/R_n$ . Equivalently, the differential resistance  $\partial V/\partial I$  approaches  $R_n$ .

In Fig. 2.6, there is also a current at zero bias ( $V = 0$ ), known as the DC Josephson current, or supercurrent  $I_s$ , which has a maximum value equal to the critical (Josephson) current  $I_c$ . This current is due to tunneling of Cooper pairs through the barrier, and hence does not follow from the quasiparticle current equation 2.24. Due to its two-particle nature, it is proportional to  $T_P^2$ .

Josephson predicted theoretically that there is an effective supercurrent  $I_s$  through a barrier, depending on the phase difference,  $\phi$ , between the phase of the wavefunction of the two electrodes [13, 14]:

$$I_s = I_c \sin \phi. \quad (2.25)$$

This effect is called the DC Josephson effect. Because of Eq. 2.25, the supercurrent at  $V = 0$  is a fraction of  $I_c$ , in a real measurement. Ambegaokar and Baratoff have shown [12] that there is a relation between the normal resistance, the superconducting energy gap and the critical current of a SIS junction, given by:

$$I_c = \frac{\pi\Delta(T)}{2eR_n} \tanh\left(\frac{\Delta(T)}{2k_B T}\right). \quad (2.26)$$

$I_c$ , as described in Eq. 2.26, is the maximum supercurrent the junction can support.

If a voltage  $V$  is applied, Josephson further deduced that the phase difference would evolve according to

$$\frac{\partial\phi}{\partial t} = \frac{2eV}{\hbar}. \quad (2.27)$$

As a consequence, this leads to an alternating current with an amplitude of  $I_c$  and a frequency  $f_J = 2eV/h$ :

$$I_s(t) = I_c \sin\left(\frac{2eVt}{\hbar} + \phi_0\right), \quad (2.28)$$

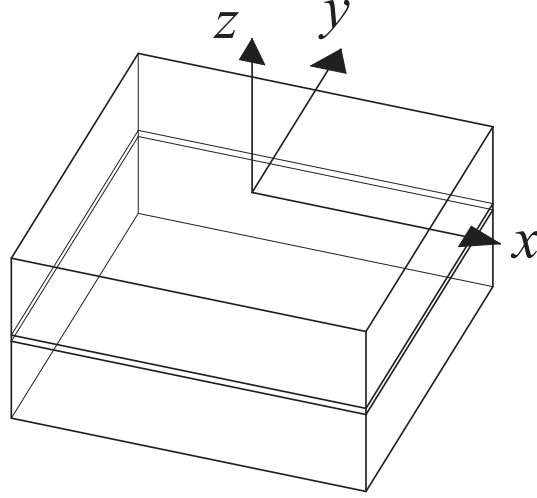


**Figure 2.8:** Schematic three-dimensional picture of an SIS junction, with cartesian coordinates  $x$ ,  $y$  and  $z$ , used for the calculation of the effect of an applied magnetic field on the Josephson current.

with  $\phi_0$  the initial phase difference between the electrodes. This effect is known as the AC Josephson effect. As a consequence, if no magnetic field is applied (see next part of this Subsection), there will always be a time averaged supercurrent in the SIS  $IV$  characteristic for  $|V| < V_g$ .

### Effect of a magnetic field on the DC Josephson current

In this work, the Josephson current is an unwanted ‘byproduct’ of an SIS junction, which hinders its performance as a heterodyne detector. Therefore,  $I_s$  will have to be as small as possible, preferably *zero*. Here, we explain how this is achieved by applying an appropriate magnetic field such that  $I_s$  is in a minimum.

To consider the effect of an applied external magnetic field,  $\mathbf{B}$ , we first define the gauge-invariant phase difference between the electrodes [6] as

$$\gamma \equiv \phi - \frac{2\pi}{\Phi_0} \int \mathbf{A} \cdot d\mathbf{s}, \quad (2.29)$$

where  $\Phi_0 = h/2e$  is the magnetic flux quantum and  $\mathbf{A}$  is the vector potential of the magnetic field:  $\mathbf{B} = \nabla \times \mathbf{A}$ . If we now consider a SIS junction in the  $(x, y)$  plane, with currents in the  $z$  direction, as shown in Fig. 2.8, we can write for  $\gamma$  [15]:

$$\nabla_{x,y}\gamma = \left( \frac{2\pi d}{\Phi_0} \mathbf{B} \times \mathbf{n}_z \right), \quad (2.30)$$

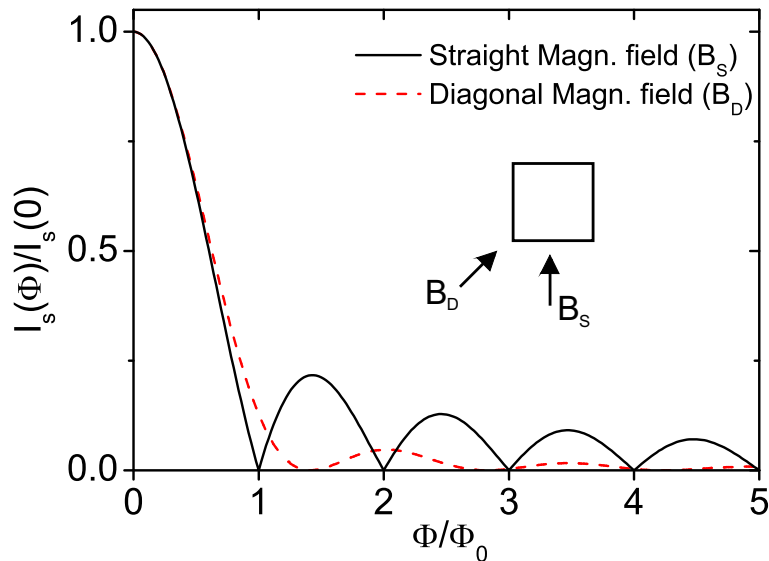


**Figure 2.9:** Factor  $I_s(\Phi)/I_s(0)$  by which the maximum Josephson current of a square SIS junction is reduced as a function of the magnetic flux  $\Phi = BdL$ , with  $L$  the length of the junction's sides. The full line shows the result for  $\mathbf{B}$  aligned with one of the sides, the dashed line for  $\mathbf{B}$  aligned with one of the diagonals, i.e. under a  $45^\circ$  angle with the sides.

with  $d = 2\lambda + t_{bar}$  and  $\lambda$  the effective London penetration depth of the superconductors of the electrodes, and  $t_{bar}$  is the barrier thickness;  $\mathbf{n}_z$  is the unit vector perpendicular to the junction ( $z$ -direction). The critical current *density*,  $J_c$  can be defined as:

$$I_c = \iint_{A_j} J_c(x, y) dx dy, \quad (2.31)$$

with  $A_j$  the junction area. For a junction with a homogeneous current density, this reduces to  $J_c = I_c/A_j$ . The confinement of the critical currents near the edges of the junction is governed by the Josephson penetration depth  $\lambda_J$ :

$$\lambda_J = \sqrt{\frac{\Phi_0}{2\pi\mu_0 d J_c}}. \quad (2.32)$$

In this work, a typical value is  $J_c = 10 \text{ kA/cm}^2$ , for niobium, with  $\lambda \approx 100 \text{ nm}$  [10], which yields a  $\lambda_J$  of about  $3.6 \text{ }\mu\text{m}$ . Hence, if the lateral dimensions of the junction are (much) smaller than  $\lambda_J$ , we can assume that the current distribution inside the junction is uniform.

The effect on the Josephson current is calculated by assuming that the magnetic field is pointed in the  $y$ -direction:  $\mathbf{B} = (0, B, 0)$ . Equation 2.30 then

becomes

$$\frac{d\gamma}{dx} = \frac{2\pi d}{\Phi_0} B \quad \text{and} \quad \frac{d\gamma}{dy} = 0, \quad (2.33)$$

which can be integrated to yield

$$\gamma(x) = \gamma_0 + \frac{2\pi d}{\Phi_0} Bx. \quad (2.34)$$

If we realize that Eq. 2.31 is in fact a special case of the formula for the effective supercurrent,

$$I_s = \iint_{A_j} J_c(x, y) \sin(\gamma(x)) dx dy, \quad (2.35)$$

this can be integrated over  $y$  to be rewritten, using Eq. 2.34, as

$$I_s = \int J_{c,x}(x) \sin\left(\gamma_0 + \frac{2\pi d}{\Phi_0} Bx\right) dx, \quad (2.36)$$

where  $J_{c,x} \equiv \int J_c(x, y) dy$  is the critical current density per unit length of the  $x$ -direction. The shape of the junction and its alignment with respect to the magnetic field determine the format of  $J_{c,x}$ . For a rectangular junction with its sides  $L_x$  and  $L_y$  along  $x$  and  $y$ , respectively, and uniform  $J_c(x, y) = J_c$ , we can write  $J_{c,x} = L_y J_c$ . If we substitute this in 2.36, it follows that

$$I_s(\Phi) = I_c \sin(\gamma) \frac{\sin(\pi\Phi/\Phi_0)}{\pi\Phi/\Phi_0}, \quad (2.37)$$

where we have used the magnetic flux through the junction,  $\Phi = BdL_x$ . This means that by application of a magnetic flux, the maximum supercurrent is reduced from its zero-flux value  $I_c$  by a factor

$$\frac{I_s(\Phi)}{I_s(0)} = \left| \frac{\sin(\pi\Phi/\Phi_0)}{\pi\Phi/\Phi_0} \right|. \quad (2.38)$$

This  $\Phi, I_s$ -dependence is often called a ‘Fraunhofer pattern’ because of its analogy with the intensity versus position dependence of light after passing a narrow rectangular slit. It is illustrated in Fig. 2.9 by a full line.

Using Eq. 2.36, the dependence of  $I_s$  on  $\Phi$  can also be calculated for other junction dimensions and magnetic field directions. This has been done extensively in the book by Barone and Paterno [15]. One specific case is for a square junction ( $L_x = L_y$ ) and a magnetic field with magnitude  $B$  under a  $45^\circ$  angle with the junction sides ( $\mathbf{B} = (B/\sqrt{2}, B/\sqrt{2}, 0)$ ), which yields

$$\frac{I_s(\Phi)}{I_s(0)} = 2 \left| \frac{\sin\left(\frac{\pi\Phi}{\sqrt{2}\Phi_0}\right)}{\pi\frac{\Phi}{\Phi_0}} \right|^2. \quad (2.39)$$

This dependence is illustrated in Fig. 2.9 by a dashed line. From this Figure it can be seen that the desired minima in the Josephson current are more stable if the magnetic field is applied diagonally to the junction orientation. Because it is in our case easier to modify the junction shape than the direction of the magnetic field, we have realized this by rotating the junctions  $45^\circ$  in our design.

### 2.1.4 Response to external radiation

To understand the use of SIS junctions as detectors for high frequency electromagnetic radiation, we will explain how both the quasiparticle current and the Josephson supercurrent are influenced by external radiation. How this radiation is exactly coupled to the SIS junctions, will be described in Section 2.2.

#### Photon assisted tunneling

To explain the effect of applied external radiation on the quasiparticle current,  $I_{qp}$ , which determines the  $IV$  characteristic (except for  $I_c$ ), as the one shown in Fig. 2.6, we assume that the Josephson current has been suppressed with a magnetic field. If external radiation is applied, the junction is biased with an AC voltage  $V_{AC}$ :

$$V_{AC} = V_{DC} + V_r \cos \omega_r t, \quad (2.40)$$

where  $V_{DC}$  is the DC bias voltage,  $V_r$  the amplitude of the voltage due to the electromagnetic radiation and  $\omega_r$  its angular frequency.

Tien and Gordon [16] were the first to calculate  $I_{qp}(V_{DC})$  under applied radiation. Assuming the external radiation causes an adiabatic modulation of the quasiparticle energies in the superconductor, they have shown that the quasiparticle level at energy  $E$  effectively splits into many levels at  $E \pm n\hbar\omega_r$ , with probabilities given by  $(J_n(eV_r/\hbar\omega_r))^2$ , where  $J_n$  is a Bessel function of the first kind and order  $n$ . Using this modified density of states in Eq. 2.24, the quasiparticle current yields

$$I_{qp}(V_{DC}) = \sum_{n=-\infty}^{\infty} J_n^2(eV_r/\hbar\omega_r) I_{qp}^0(V_{DC} + n\hbar\omega_r/e), \quad (2.41)$$

where  $I_{qp}^0(V)$  is the current-voltage dependence without radiation. The argument of the Bessel function is often called the pump parameter  $\alpha$ :

$$\alpha = eV_r/\hbar\omega_r, \quad (2.42)$$

while applying radiation to an SIS junction is often referred to as *pumping*.

We see that according to Eq. 2.41, the original, radiation-less quasiparticle current is repeated with steps equal to  $\hbar\omega_r/e$  in voltage. Because of the very

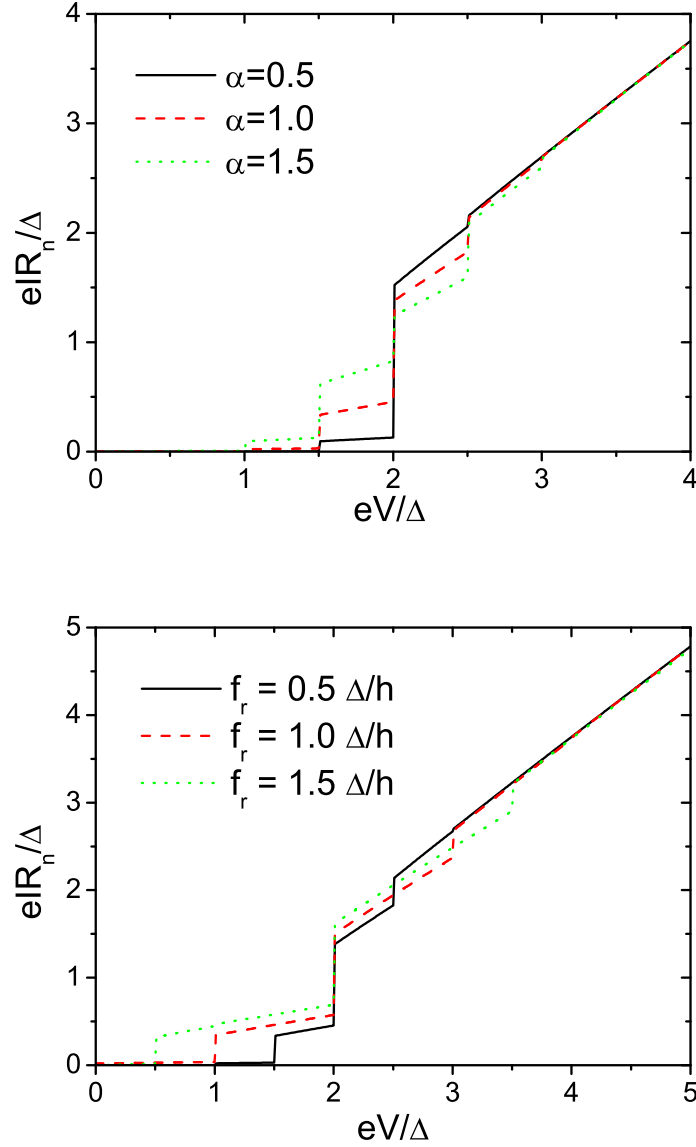


**Figure 2.10:** Effect of radiation on SIS quasiparticle  $IV$  characteristics (at 0 K). (Top)  $IV$  characteristics for  $\alpha$  equal to 0.5, 1, and 1.5, while  $f_r = 0.5\Delta/h$ . (Bottom)  $IV$  characteristics for  $f_r$  equal to 0.5, 1 and 1.5  $\Delta/h$ , while  $\alpha = 1$ .

non-linear onset of quasiparticle tunneling at the gap voltage, this results in a step-like  $IV$  characteristic, with the step size determined by the radiation frequency, and the step height determined by the pump parameter of the radiation. This is illustrated by the *pumped*  $IV$  curves in Fig. 2.10. The steps in the  $IV$  characteristic are often called *photon steps*.

This effect can be understood by realizing that quasiparticles can tunnel through the barrier at voltages smaller than  $V_g$  while absorbing one or more

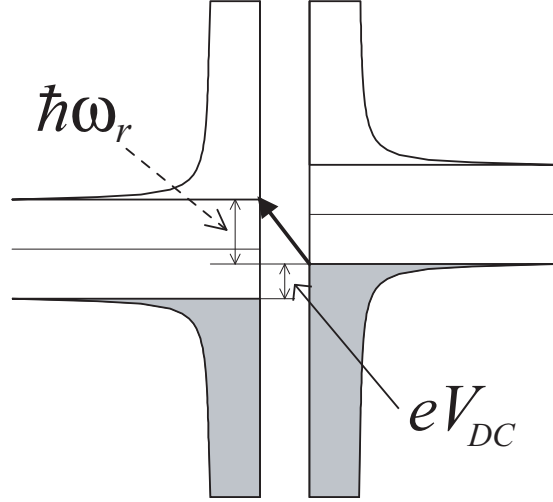


**Figure 2.11:** Semiconductor representation of photon assisted tunneling of quasiparticles from the valence band of one electrode to the conduction band of the other electrode (indicated by the black arrow) under absorption of a photon (dashed arrow) of energy  $\hbar\omega_r$ . The applied DC bias voltage relatively offsets the two Fermi levels with an energy  $eV_{DC}$ .

photons. These photons then provide the energy for a quasiparticle from the ‘valence band’ of one electrode to tunnel to the ‘conduction band’ of the other. Therefore, this effect is called *photon assisted tunneling*. This is illustrated with the semiconductor model in Fig. 2.11 for one photon.

### AC Josephson effect: Shapiro steps

If the Josephson current is not sufficiently suppressed with a magnetic field, the AC Josephson effect can ‘pollute’ the  $IV$  characteristic: if an SIS junction is irradiated with radiation of angular frequency  $\omega_r$ , the  $IV$  curve will show a constant-voltage step in the current for voltages

$$V_n = n \frac{\hbar\omega_r}{2e}. \quad (2.43)$$

These steps are called *Shapiro steps*, after their first observation by Shapiro [17]. Similar to quasiparticle-tunneling, they can be interpreted as the tunneling of a Cooper pair under the absorption of  $n$  photons of the applied radiation.

After inserting the ideal voltage bias of an irradiated SIS junction given in Eq. 2.40 into Eq. 2.27 and integrating, it follows that the supercurrent equals

$$I_s = I_c \sin \left( \phi_0 + \frac{2eV_{DC}}{\hbar} t + \frac{2eV_r}{\hbar\omega_r} \sin \omega_r t \right). \quad (2.44)$$

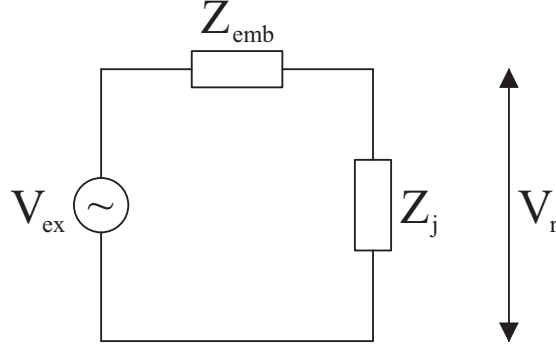


**Figure 2.12:** Schematic representation of an external radiation source  $V_{ex}$  coupled to an SIS junction with impedance  $Z_j$  via an embedding impedance  $Z_{emb}$ , generating a voltage  $V_r$  across the junction.

This expression, which contains a sine of a sine, can be expanded in terms of Bessel functions, yielding [6, 15]

$$I_s = I_c \sum_{n=-\infty}^{\infty} (-1)^n J_n(2eV_r/\hbar\omega_r) \sin(\phi_0 + (2eV_{DC}/\hbar - n\omega_r)t). \quad (2.45)$$

This leads to the conclusion that there is only a DC component to the supercurrent  $I_s$  if  $V_{DC}$  has a value  $V_n$  that satisfies Eq. 2.43. The maximum supercurrent is then given by

$$I_n = I_c J_n\left(\frac{2eV_r}{\hbar\omega_r}\right). \quad (2.46)$$

## 2.2 Coupling applied radiation to a tunneljunction

After Section 2.1, where we have provided a general description and the main characteristics of SIS junctions, we will now focus on the coupling of external radiation to a tunneljunction. From here on, we will assume that the Josephson supercurrent has been suppressed with a magnetic field, as described in Subsection 2.1.3. As a consequence, the  $IV$  curve will be like in Fig. 2.6, apart from  $I_c$ , which will be zero.

### 2.2.1 Schematic representation

To put the discussion about coupling between external radiation and an SIS junction into the right perspective, we will first discuss the physical system that we are using for our SIS detectors. At this stage, a schematic representation of

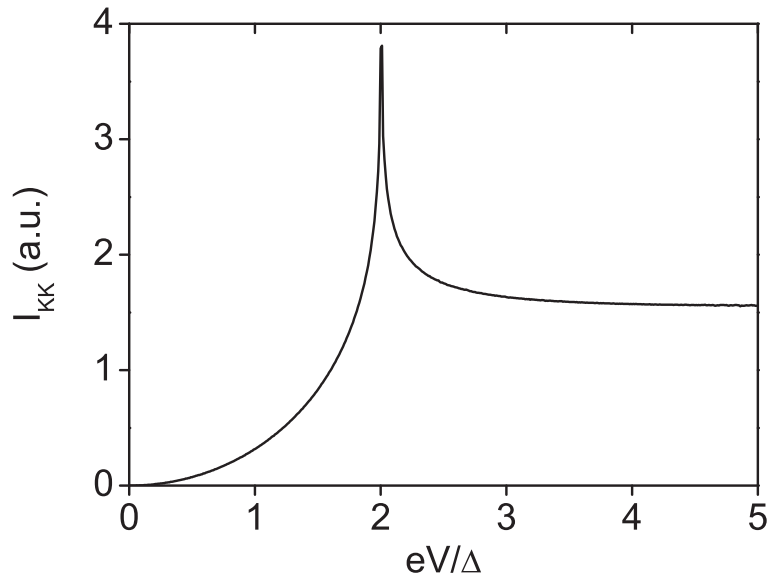


**Figure 2.13:** Calculated Kramers-Kronig transform of DC SIS ( $I_{qp}^0, V_{DC}$ ) curve.

the system will be sufficient. This representation is shown in Fig. 2.12.  $V_{ex}$  is the external radiation source that supplies our system. In this Section, it originates from a local oscillator (LO) source, but without loss of generality it can also come from a small astronomical signal we want to observe.

The external radiation is an electromagnetic wave, time-varying electric and magnetic fields  $\mathbf{E}(t)$  and  $\mathbf{B}(t)$ . These fields propagate through the system, and finally generate a voltage across the SIS junction, equal to  $V_r$ .

In our case, the radiation is caught by a *horn*, transmitted through a *waveguide* which has a dielectric *substrate* mounted across. The waveguide is terminated by a *backshort cavity*. The substrate has a superconducting antenna pattern on it, with a *probe point* for the insertion of the radiation. The radiation finally reaches the SIS junction via a superconducting *microstripline*. All these components, leading the signal from free space to the junction, respond in their specific way to the applied radiation, which can be represented by a single (frequency-dependent) *embedding impedance*  $Z_{emb}$ . The junction's RF impedance  $Z_j$  will be discussed in Subsection 2.2.2.

### 2.2.2 AC and DC (quantum) tunneling currents

In the previous Subsection it was mentioned that an SIS junction has a RF impedance  $Z_j$ , also called tunnel impedance. This impedance is complex, which is due to the real and imaginary parts of the tunneling current-amplitude  $I_{LO}$ . The actual current through the junction - irradiated with radiation of angular

frequency  $\omega_r$  - will be  $\Re\{I_{LO}e^{i\omega_r t}\}$ . We have

$$I_{LO} = I'_{LO} + iI''_{LO}, \quad (2.47)$$

where we find from the quantum mixer theory of Tucker and Feldman [18] and from Werthamer [19], that

$$I'_{LO} = \sum_{n=-\infty}^{\infty} 2n \frac{J_n^2(\alpha)}{\alpha} I_{qp}^0(V_{DC} + n\hbar\omega_r/e) \quad (2.48)$$

and

$$I''_{LO} = \sum_{n=-\infty}^{\infty} J_n(\alpha)(J_{n-1}(\alpha) - J_{n+1}(\alpha)) I_{KK}(V_{DC} + n\hbar\omega_r/e), \quad (2.49)$$

where  $\alpha$  has been defined in Eq. 2.42 and  $I_{KK}$  is the Kramers-Kronig transform of  $I_{qp}^0$ :

$$I_{KK}(V) = \text{P.V.} \frac{1}{\pi} \int_{-\infty}^{\infty} \frac{I_{qp}^0(V') - V'/R_n}{V' - V} dV'. \quad (2.50)$$

$I_{KK}$ , based on an ideal 0 K quasiparticle current  $I_{qp}$  (shown in Fig. 2.6), is plotted in Fig. 2.13. These equations show that for an SIS junction, to which an AC field of angular frequency  $\omega_r$  and voltage amplitude  $V_r$  has been applied, the AC tunnel current can be derived, if the DC tunnel current  $I_{qp}^0(V_{DC})$  is known.

The tunnel impedance is now defined as  $Z_j = V_r/I_{LO}$ . Using Eqs. 2.48 and 2.49, it is plotted in Fig. 2.14, for a radiation frequency of half the gap voltage and in the limit for a zero pump parameter  $\alpha$ . In this picture, the tunnel impedance is split up into tunnel resistance  $R_j$  and tunnel reactance  $X_j$ , with  $Z_j = R_j + iX_j$ . We see that  $Z_j$  features a complicated behavior as a function of DC bias voltage  $V$ .

### 2.2.3 Matching of embedding impedance to junction impedance

For a certain external radiation source ( $V_{ex}$  in Fig. 2.12), the pump parameter  $\alpha = eV_r/hf_r$  will be determined (through  $V_r$ ) by  $Z_{emb}$  and  $Z_j$ . Because the junction impedance  $Z_j$  is bias voltage dependent,  $\alpha$  will also be bias dependent. Therefore, the pumped  $IV$  curve will be different from the ones in Fig. 2.10, which are for a bias-independent  $\alpha$ . The power matching efficiency  $M$  between the embedding impedance and the tunnel impedance is given by

$$M = 1 - \left| \frac{Z_{emb} - Z_j^*}{Z_{emb} + Z_j^*} \right|^2. \quad (2.51)$$

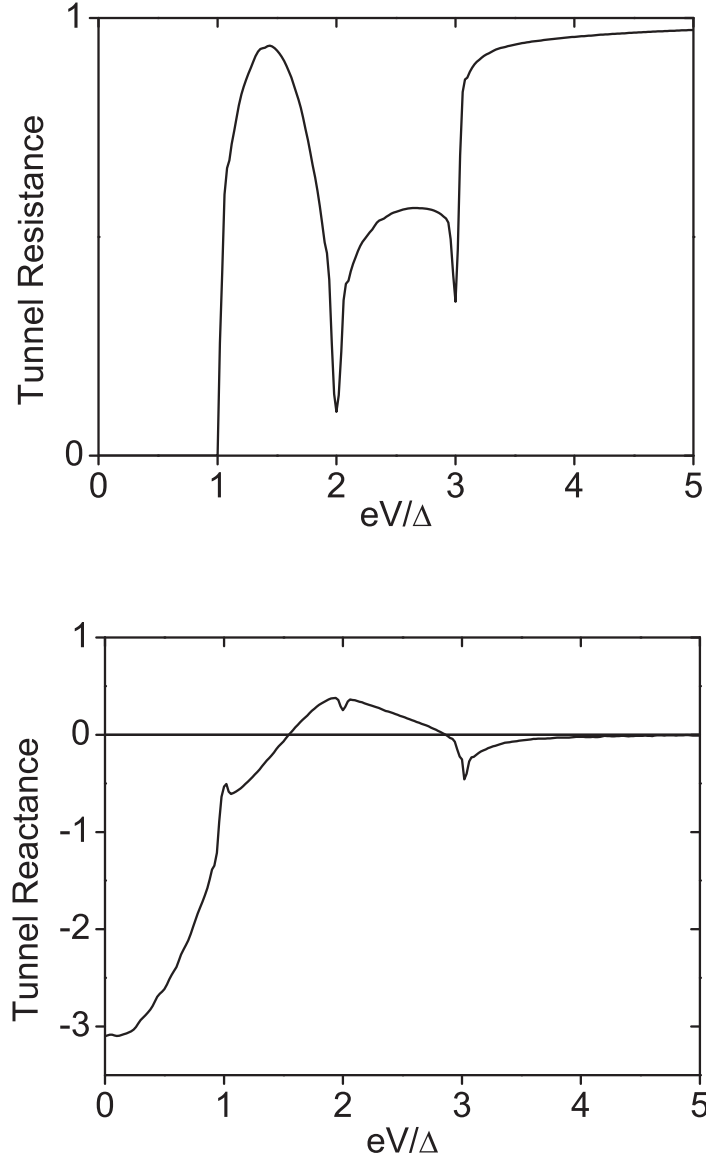


**Figure 2.14:** Calculated tunnel impedance  $Z_j$  split up in its real and imaginary parts, for a radiation frequency  $f_r = \Delta/h$  and  $\alpha \rightarrow 0$ . (Top) Real part, or tunnel resistance  $R_j = V_r/I'_{LO}$ , calculated using Eq. 2.48. (Bottom) Imaginary part, or tunnel reactance  $X_j = V_r/I''_{LO}$ , calculated from Eq. 2.49.

We see that  $Z_{emb}$  and  $Z_j$  are matched, when  $Z_{emb} = Z_j^*$ . In this case, the maximum available power  $P_{av}$ , which the radiation source can deliver, is transferred to the junction.  $P_{av}$  is then given by:

$$P_{av} = \frac{|V_{ex}|^2}{8R_{emb}}, \quad (2.52)$$

where  $R_{emb}$  is the real part of the embedding impedance.

In Fig. 2.14, we see that the tunnel reactance is negative at the beginning of the first photon step (at  $eV/\Delta = 1$ , since  $f_r = \Delta/h$ ), but changes sign about halfway in the step when the bias voltage is increased. As a consequence, the behavior of  $\alpha$  will depend on the sign of the embedding reactance  $X_{emb}$ . If  $X_{emb} < 0$ , we call the embedding ‘capacitive,’ if  $X_{emb} > 0$ , the embedding is ‘inductive.’

In Fig. 2.15 we show simulated curves for  $hf_r = \Delta$  and  $eV_{ex} = \Delta$ , demonstrating the influence of a capacitive and an inductive embedding on  $\alpha$  and the  $IV$  characteristic. These graphs are obtained using the calculated curves in Fig. 2.14 for  $Z_j$  and the voltage divider relation

$$V_r = V_{ex} \frac{Z_j}{Z_{emb} + Z_j} \quad (2.53)$$

to obtain  $\alpha (= eV_r/hf_r)$ , and this  $V_r$  substituted in Eq. 2.41 for the pumped  $IV$ .

For a capacitive embedding, the matching improves as the bias voltage is increased along the first photon step ( $1 < eV/\Delta < 2$  in Fig. 2.15), whereas for an inductive embedding, the matching is fine at first, but decreases dramatically. This is reflected in  $\alpha$ , and thus in the  $IV$  curve. A capacitive embedding causes a ‘normal’ photon step, but an inductive embedding causes an ‘abnormal’ photon step in the sense that its slope (the inverse of the differential resistance) can become negative.

It should be mentioned that the junction itself has a capacitance in parallel to  $Z_j$  which contributes to the embedding impedance. In practical applications, this capacitance is rather large, causing a large mismatch between embedding and junction impedance. As a result of this, the matching will not change significantly when the bias is changed, and  $\alpha$  will be independent of bias. In this case, the  $IV$  curve will not show the effects (such as the negative slope) that are illustrated in Fig. 2.15.

## 2.3 Mixing process and noise temperature

In the previous Section, we have described the coupling of a (strong) radiation source to a superconducting tunnel junction. We will now explain how a high frequency signal is converted to a lower frequency, using the SIS as a mixer, and how the mixer adds noise to the system. This Section is for the most part based on the quantum mixer theory, described by Tucker and Feldman [18].

### 2.3.1 Direct response of a tunneljunction

In the previous Sections we have seen that when an AC signal (with frequency  $f_r$  and voltage amplitude  $V_r$ ) is applied to an STJ, a change in the DC tunnel

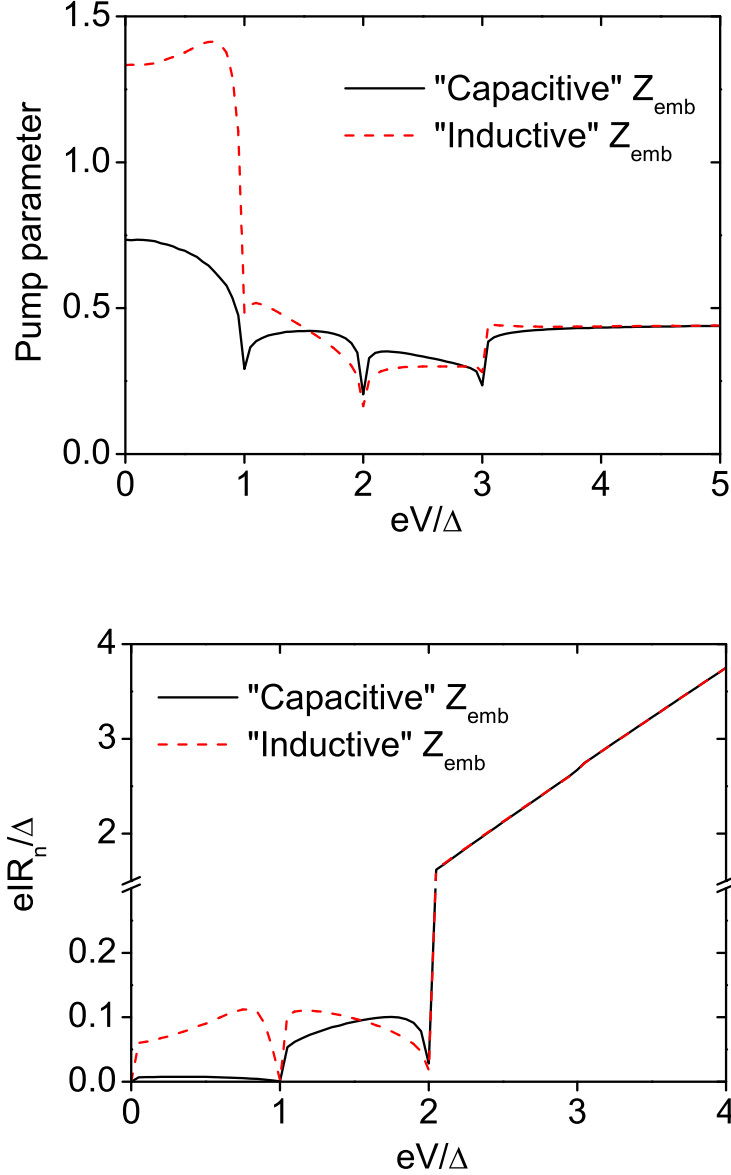


**Figure 2.15:** Influence of embedding impedance  $Z_{emb}$  on pump parameter  $\alpha$  and DC  $IV$  curve, for  $hf_r = eV_{ex} = \Delta$ . (Top)  $\alpha$  as a function of bias voltage for a capacitive embedding,  $Z_{emb,C} = R_n(1 - i)$  and an inductive embedding,  $Z_{emb,L} = R_n(1 + i)$ , based on the calculation of  $Z_j$ , shown in Fig. 2.14. (Bottom) DC  $IV$  characteristics for the same capacitive and inductive embedding, calculated using Eq. 2.41. Clearly, the inductive embedding leads to a negative slope of the photon step.

current  $I_{qp}$  can be observed,  $\Delta I_{DC} = I_{qp} - I_{qp}^0$ . If we look only at this DC current signal, we are using the SIS as a direct detector for radiation.

The current responsivity of a direct detector is defined as

$$R_i = \frac{\Delta I_{DC}}{P_{abs}}, \quad (2.54)$$

where  $P_{abs}$  is the radiation power absorbed by the detector. In our case,  $P_{abs} = \frac{1}{2}V_r I'_{LO}$ . Using Eq. 2.41 with the lowest order terms  $n = -1, 0, 1$  and approximating the Bessel functions with  $J_0(x) \sim 1 - x^2/4$  and  $J_n(x) \sim (\pm x/2)^n/n!$ , we find

$$\Delta I_{DC} = \frac{V_r^2}{4} \left( \frac{I_{qp}^0(V + \hbar\omega_r/e) - 2I_{qp}^0(V) + I_{qp}^0(V - \hbar\omega_r/e)}{(\hbar\omega_r/e)^2} \right). \quad (2.55)$$

Applying the same approximation to Eq. 2.48, we can write it as

$$I'_{LO} = V_r \left( \frac{I_{qp}^0(V + \hbar\omega_r/e) - I_{qp}^0(V - \hbar\omega_r/e)}{2(\hbar\omega_r/e)} \right). \quad (2.56)$$

Substituting Eqs. 2.55 and 2.56 into 2.54, we now find:

$$\begin{aligned} R_i &= \frac{e}{\hbar\omega_r} \left( \frac{I_{qp}^0(V + \hbar\omega_r/e) - 2I_{qp}^0(V) + I_{qp}^0(V - \hbar\omega_r/e)}{I_{qp}^0(V + \hbar\omega_r/e) - I_{qp}^0(V - \hbar\omega_r/e)} \right) \\ &\rightarrow \frac{1}{2} \frac{d^2 I_{qp}^0/dV^2}{dI_{qp}^0/dV} \quad (\text{classical limit}) \\ &\rightarrow \frac{e}{\hbar\omega_r} \quad (\text{quantum limit}). \end{aligned} \quad (2.57)$$

The ‘quantum limit’ is obtained by realizing that in the limit of a perfect detector,  $I_{qp}^0(V + \hbar\omega_r/e)$  is much larger than both  $I_{qp}^0(V)$  and  $I_{qp}^0(V - \hbar\omega_r/e)$ , which makes the fraction between the large parentheses approach unity. This result can also be qualitatively understood as a detector that responds with the tunneling of one electron (with charge  $e$ ) to each photon (with energy  $\hbar\omega_r$ ) that reaches it.

Eq. 2.57 also shows that  $R_i$  is zero for a linear element ( $d^2I/dV^2 = 0$ ) and that the responsivity becomes greater the ‘more non-linear’ the  $IV$  characteristic is. Further, it should be clear that a negative slope of the photon step due to an inductive embedding, as discussed in Subsection 2.2.3, is undesirable. The quantum mixer theory extends the classical mixer theory towards the quantum limit. This will be explained in the next Subsection.

### 2.3.2 Mixer properties and gain

If we want to know how the current through an STJ responds to more than one frequency (this is the actual mixing), we have to focus on frequencies that obey

$$f_m = f_{IF} + m f_{LO}, \quad (2.58)$$

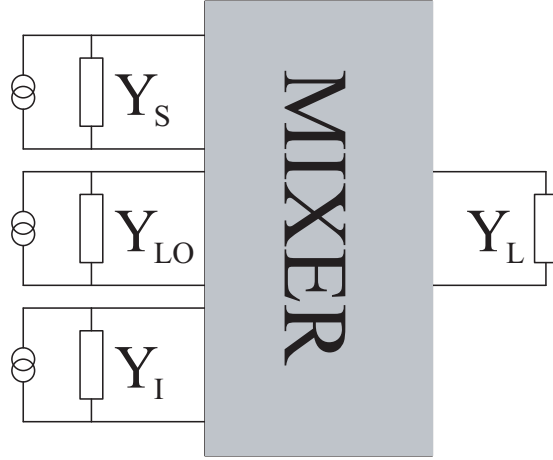


**Figure 2.16:** Schematic diagram of heterodyne mixing, approximated with three input ports (signal, LO and image), with internal admittances  $Y_S$ ,  $Y_{LO}$  and  $Y_I$ , and one output port (IF), with a load admittance  $Y_L$ .

where  $f_{IF}$  is the intermediate frequency,  $f_{LO}$  is the local oscillator frequency, and  $m$  is an integer. We will consider only  $m = -1, 0, 1$ , because we assume that higher frequencies will be shorted by the geometrical capacitance of the SIS junction. We then define  $f_{-1} = f_I$ , the image frequency or *lower sideband* (LSB) frequency, and  $f_1 = f_S$ , the signal or *upper sideband* (USB) frequency. Evidently,  $f_0 = f_{IF}$ . These frequencies can be shown in a four-port diagram (Fig. 2.16). The signal and image ports are connected to a current source with an internal admittance ( $Y_S$  and  $Y_I$ , respectively), similar to the source of the LO, which is now also represented as a current source with an internal admittance  $Y_{LO} = 1/Z_{emb}$ . The IF is terminated by a load admittance  $Y_L$ . The relations between the currents and voltages on these ports can be represented by a matrix equation

$$\begin{pmatrix} I_1 \\ 0 \\ I_{-1} \end{pmatrix} = \begin{pmatrix} Y_{11} + Y_S & Y_{10} & Y_{1-1} \\ Y_{01} & Y_{00} + Y_L & Y_{0-1} \\ Y_{-11} & Y_{-10} & Y_{-1-1} + Y_I \end{pmatrix} \begin{pmatrix} V_1 \\ V_0 \\ V_{-1} \end{pmatrix}, \quad (2.59)$$

where  $I_1$  and  $I_{-1}$  are the amplitudes of the equivalent current source of signal (USB) and image (LSB), respectively,  $V_1$ ,  $V_0$  and  $V_{-1}$  are the voltages across the ports, and the  $Y_{mm'}$  matrix elements describe the interaction of the tunneljunction with the different frequencies. In Eq. 2.59, the LO current is not included, because in mixer theory, the LO is assumed to be a very large signal, of which the USB and LSB signals are merely small modulations.

If we split up the matrix elements into a real and an imaginary part according

to  $Y_{mm'} = G_{mm'} + iB_{mm'}$ , it can be derived from mixer theory that

$$G_{mm'} = \frac{e}{2hf_{m'}} \sum_{n,n'=-\infty}^{\infty} J_n(\alpha)J_{n'}(\alpha)\delta_{m-m',n'-n} \left[ I_{qp}^0 \left( V_0 + \frac{h}{e}(n'f_{LO} + f_{m'}) \right) - I_{qp}^0 \left( V_0 + n'\frac{hf_{LO}}{e} \right) + I_{qp}^0 \left( V_0 + n\frac{hf_{LO}}{e} \right) - I_{qp}^0 \left( V_0 + \frac{h}{e}(nf_{LO} - f_{m'}) \right) \right] \quad (2.60)$$

and

$$B_{mm'} = \frac{e}{2hf_{m'}} \sum_{n,n'=-\infty}^{\infty} J_n(\alpha)J_{n'}(\alpha)\delta_{m-m',n'-n} \left[ I_{KK} \left( V_0 + \frac{h}{e}(n'f_{LO} + f_{m'}) \right) - I_{KK} \left( V_0 + n'\frac{hf_{LO}}{e} \right) + I_{KK} \left( V_0 + n\frac{hf_{LO}}{e} \right) - I_{KK} \left( V_0 + \frac{h}{e}(nf_{LO} - f_{m'}) \right) \right]. \quad (2.61)$$

These equations show that all elements  $Y_{mm'}$  can be determined once the DC  $IV$  dependence and its Kramers-Kronig transform are known.

The actual output signal is the power that is dissipated in the IF load,  $G_L|V_0|^2/2$ , where  $G_L$  is the load conductance ( $Y_L = G_L + iB_L$ ). To obtain  $V_0$ , the  $\mathbf{Y}$ -matrix has to be inverted into a  $\mathbf{Z}$ -matrix,  $\mathbf{Z} = \mathbf{Y}^{-1}$ , with matrix elements  $Z_{mm'}$ , so that the voltage  $V_0$  can be written as

$$V_0 = Z_{00} \sum_m \lambda_{0m} I_m, \quad (2.62)$$

where

$$\lambda_{mm'} = \frac{Z_{mm'}}{Z_{00}} \quad (2.63)$$

are the matrix elements of  $\mathbf{Z}$ , normalized to  $Z_{00}$ . Eq. 2.62 shows that a current source  $I_m$  (of frequency  $f_m$ ) at one of the input ports is equivalent to a fictitious current source  $\lambda_{0m}I_m$  (of frequency  $f_{IF}$ ) at the IF output, which is independent of the IF load  $Y_L$ . The sum of these fictitious current sources is related via the matrix element  $Z_{00}$  to the output voltage  $V_0$ . Using Eqs. 2.62 and 2.63, we find the IF output power:

$$P_{out} = \frac{G_L}{2}|V_0|^2 = \frac{G_L}{2} (|Z_{01}|^2|I_S|^2 + |Z_{0-1}|^2|I_I|^2), \quad (2.64)$$

with  $I_S = I_1$  the signal current source and  $I_I = I_{-1}$  the image current source. The available input power may be written as

$$P_{in} = \frac{|I_S|^2}{8G_S} + \frac{|I_I|^2}{8G_I}, \quad (2.65)$$

where  $G_S$  and  $G_I$  are the signal and image conductances, respectively.

The quantity  $G_{mix} = P_{out}/P_{in}$  is called the mixer (conversion) gain. We can distinguish two different types of mixer gain: the double sideband (DSB) and the single sideband (SSB) gain. In an experiment where a black body is used as a signal source, radiating at both the signal and the image port, we use the DSB gain. We then assume that both signal and image port deliver the same input power, so that we can write for the total input power

$$P_{in} = \frac{|I_S|^2}{4G_S} = \frac{|I_I|^2}{4G_I}. \quad (2.66)$$

The DSB mixer gain then follows by using Eq. 2.64:

$$G_{mix}^{DSB} = 2G_L (G_S|Z_{01}|^2 + G_I|Z_{0-1}|^2). \quad (2.67)$$

The SSB gain on the other hand is more useful in experiments where the signal is a narrow spectral line at the signal port, as in the application of our detectors for astronomy. We find the SSB mixer gain by taking  $I_I = 0$  in 2.64 and 2.65:

$$G_{mix}^{SSB} = 4G_L G_S |Z_{01}|^2. \quad (2.68)$$

### 2.3.3 Noise contribution of the mixing element

The noise in an SIS junction is a combination of shot noise of the tunnel current (due to the bias voltage and the LO irradiation), thermal fluctuations in the dissipative terminations of the IF ports, and ‘quantum noise’ due to quantization of the electromagnetic fields. This has been described in detail by Tucker and Feldman [18]. In addition, the shot noise can be larger due to (multiple) Andreev reflections of quasiparticles in the barrier [20].

The noise power at the IF port can be calculated using the  $\mathbf{Y}$ -matrix from Eq. 2.59 with its elements defined by Eqs. 2.60 and 2.61, and assuming noise sources emitting thermal and shot-noise at the different input ports. The result for the noise power per unit bandwidth dissipated at the IF port is

$$P_n = G_L \sum_{m,m'=-1}^1 Z_{0m} Z_{0m'}^* H_{mm'}, \quad (2.69)$$

where

$$H_{mm'} = e \sum_{n,n'=-\infty}^{\infty} J_n(\alpha) J_{n'}(\alpha) \delta_{m-m',n'-n} \left[ \coth \left( \frac{eV + n' h f_{LO} + h f_{m'}}{2k_B T} \right) I_{qp}^0 \left( V + n' \frac{h f_{LO}}{e} + \frac{h f_{m'}}{e} \right) + \coth \left( \frac{eV + n h f_{LO} - h f_{m'}}{2k_B T} \right) I_{qp}^0 \left( V + n \frac{h f_{LO}}{e} - \frac{h f_{m'}}{e} \right) \right] \quad (2.70)$$

are the elements of the current correlation matrix  $\mathbf{H}$ .

It can be shown that output noise power of Eq. 2.69 can be zero. This means that in this case a DC current, which appears due to the input power coming from an LO source, does not produce noise at the mixer output. The explanation for this is that the noise produced by the LO is correlated with the noise from the signal and image ports, and thus cancels at the IF. This situation means that the mixer itself does not add noise to the input signal.

However, zero noise due to the mixer does not mean that the noise in the output can be zero. There will always be a noise contribution from the zero-point fluctuations of the electromagnetic field,  $G_{mix}hf_{LO}/2$  [21].

### Noise temperature

It is common practice, especially in astronomy, to characterize the noise performance of a heterodyne system by a *noise temperature*,  $T_n$ . This  $T_n$  is defined as the noise power per unit bandwidth, divided by Boltzmann's constant  $k_B$  [22]. It is approximately equal to the temperature of a virtual black body radiator at the input of a system which produces the same amount of noise at the output as the system itself.

The radiation output of a black body at temperature  $T$  in a bandwidth  $\Delta f = f_f - f_i$  is given by Planck's law:

$$P_{bb,Pl} = \int_{f_i}^{f_f} \frac{hf}{e^{hf/k_B T} - 1} df. \quad (2.71)$$

In the Rayleigh-Jeans (RJ) limit ( $hf \ll k_B T$ ), this reduces to

$$P_{bb,RJ} = k_B T \Delta f. \quad (2.72)$$

We will now explain how the noise temperature of a heterodyne system is determined by measuring the output noise power of two black bodies at different temperatures  $T_{cl}$  (cold load) and  $T_{hl}$  (hot load). If we assume our system to be in the RJ limit (which is only justified in our case if we define the noise temperature as a convenient scaling of the noise power, like we did above (see also Ref. [22]), we can write the system output noise power of a black body radiator (of temperature  $T$ ) at the input as

$$P_{n,out} = Gk_B T \Delta f_{IF} + P_{n,sys} = Gk_B \Delta f_{IF} (T + T_n), \quad (2.73)$$

where  $G$  is the conversion gain,  $\Delta f_{IF}$  is the IF bandwidth,  $P_{n,sys}$  is the noise added by the system and  $T_n$  is its equivalent noise temperature. If we now would measure the output power of both the cold load ( $P_c$ ) and the hot load ( $P_h$ ), and divide one with the other, we get:

$$Y = \frac{P_c}{P_h} = \frac{Gk_B \Delta f_{IF} (T_{cl} + T_n)}{Gk_B \Delta f_{IF} (T_{hl} + T_n)} = \frac{T_{cl} + T_n}{T_{hl} + T_n}, \quad (2.74)$$

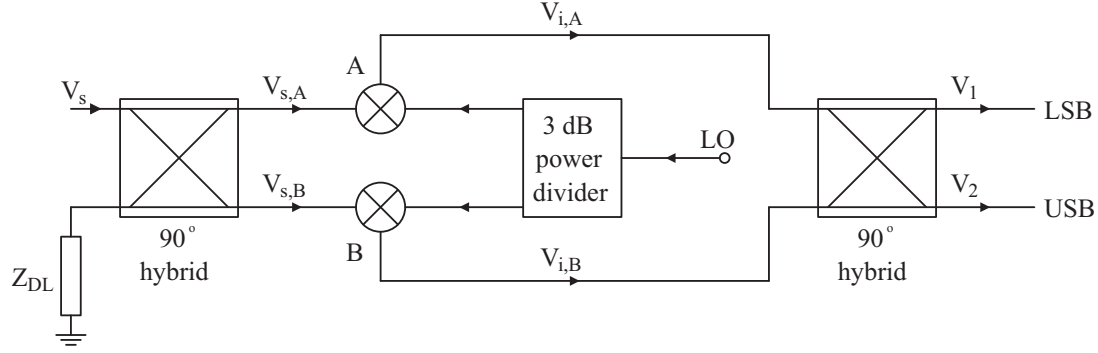


**Figure 2.17:** Schematic diagram of an image rejection mixer.  $Z_{DL}$  is a dumping load.

where the ratio  $Y$  is called the  $Y$ -factor. Eq. 2.74 yields immediately

$$T_n = \frac{T_{cl} - YT_{hl}}{Y - 1}. \quad (2.75)$$

### 2.3.4 Sideband separating

A heterodyne mixer converts a signal with angular frequency  $\omega_{LO} \pm \omega_i$ :

$$\hat{V}_s \cos[(\omega_{LO} \pm \omega_i)t + \zeta],$$

where  $\hat{V}_s$  is the voltage amplitude and  $\zeta$  is a phase offset, by mixing it with a local oscillator at  $\omega_{LO}$ , to a signal with angular frequency  $\omega_i$ :

$$g\hat{V}_s \cos[\omega_i t \pm \zeta],$$

where  $g$  is a mixer conversion factor. In a DSB mixer,  $\zeta$  is zero, and both USB and LSB are converted indistinguishably into a signal with frequency  $f_i$ , in the IF band. In an SSB mixer the phase  $\zeta$  is used in a smart way with two equal mixers to form an *image rejection mixer*. An SSB mixer has two outputs: one for the USB and one for the LSB.

The schematic for an image rejection mixer is shown in Fig. 2.17. Let us consider a signal  $V_s$  that consists of an upper and a lower sideband:

$$V_s = V_U \cos(\omega_{LO} + \omega_i)t + V_L \cos(\omega_{LO} - \omega_i)t, \quad (2.76)$$

where  $V_U$  and  $V_L$  are the amplitudes of upper and lower sideband, respectively. If the signal is now split up by a so-called  $90^\circ$  hybrid in (half) the original signal and (half) the signal with a  $90^\circ$  ( $= \pi/2$  rad) phase delay and subsequently fed to the mixers, the input to these mixers is:

$$V_{s,A} = \frac{V_U}{\sqrt{2}} \cos(\omega_{LO} + \omega_i)t + \frac{V_L}{\sqrt{2}} \cos(\omega_{LO} - \omega_i)t \quad (2.77)$$

$$V_{s,B} = \frac{V_U}{\sqrt{2}} \cos[(\omega_{LO} + \omega_i)t - \pi/2] + \frac{V_L}{\sqrt{2}} \cos[(\omega_{LO} - \omega_i)t - \pi/2], \quad (2.78)$$

for mixer A and B, respectively. Following the beginning of this Subsection, the IF outputs of the mixers are given by

$$V_{i,A} = \frac{gV_U}{\sqrt{2}} \cos[\omega_i t] + \frac{gV_L}{\sqrt{2}} \cos[\omega_i t] \quad (2.79)$$

$$V_{i,B} = \frac{gV_U}{\sqrt{2}} \cos[\omega_i t - \pi/2] + \frac{gV_L}{\sqrt{2}} \cos[\omega_i t + \pi/2]. \quad (2.80)$$

We finally obtain the LSB separately by combining  $V_{i,A}$  with a  $\pi/2$  phase delay of  $V_{i,B}$ :

$$\begin{aligned} V_1 &= \frac{g}{2} (V_U \cos[\omega_i t] + V_L \cos[\omega_i t] + V_U \cos[\omega_i t - \pi] + V_L \cos[\omega_i t]) \\ &= gV_L \cos[\omega_i t], \end{aligned} \quad (2.81)$$

and equivalently, the USB signal by combining  $V_{i,B}$  with a  $\pi/2$  phase delay of  $V_{i,A}$ :

$$\begin{aligned} V_2 &= \frac{g}{2} (V_U \cos[\omega_i t - \pi/2] + V_L \cos[\omega_i t + \pi/2] \\ &\quad + V_U \cos[\omega_i t - \pi/2] + V_L \cos[\omega_i t - \pi/2]) \\ &= gV_U \sin[\omega_i t]. \end{aligned} \quad (2.82)$$

We see that signal  $V_1$  corresponds to the LSB, and  $V_2$  to the USB. Hence, the two sidebands can be measured separately.

## 2.4 Conclusion

In this Chapter, we have given an introduction to the field of superconducting tunneljunctions applied as a heterodyne mixer. The properties of superconductors have been discussed, as well as the characteristics of SIS junctions. The heterodyne mixing process has been explained in some detail.

We have seen that SIS junctions can in principle be quantum-limited radiation detectors, making them theoretically the best heterodyne mixers available. The performance of SIS mixers is in reality not only limited by quantum mechanics, but also by the quality of the fabricated devices and the tuning of the embedding impedance to the junction impedance.

Nonetheless, SIS junctions are, for submillimeter wavelengths, the best heterodyne detectors that exist. Their performance is limited in frequency by the gap frequency of the superconducting electrodes in two ways. First, the mixer conversion gain degrades rapidly for frequencies beyond  $2f_{gap} = 4\Delta/h$ . Secondly, the superconducting microstrip lines (which are being used to tune the embedding to the junction impedance and compensate for the junction's capacitance) generate many losses above  $f_{gap} = 2\Delta/h$  because they act there as normal resistors, making the tuning very difficult.

The challenges in this work lay in the maximization of the coupling of an external electromagnetic wave-signal to an SIS junction. For ALMA Band 9, the detectors are required (see Chapter 3) to have a high sensitivity over the full band. Therefore, state-of-the-art SIS junctions have to be realized (Chapters 4 and 5). To increase the bandwidth of the detectors, we have studied the use of a new tunnel barrier material (Chapters 5, 7 and 8) and we have investigated the limitations of the superconducting matching circuit between the antenna and the junction (Chapters 6 and 8).

## References

- [1] J. Bardeen, L. N. Cooper, and J. R. Schrieffer, “Theory of superconductivity”, *Phys. Rev.*, Vol. **108**, 1175 (1957).
- [2] R. C. Dynes, V. Narayanamurti, and J. P. Garno, “Direct measurement of quasiparticle-lifetime broadening in a strong-coupled superconductor”, *Phys. Rev. Lett.*, Vol. **41**, 1509 (1978).
- [3] W. Meissner, and R. Ochsenfeld, “Ein neuer Effekt bei Eintritt der Supraleitfähigkeit”, *Naturwissenschaften*, Vol. **21**, 787 (1933).
- [4] V. L. Ginzburg and L. D. Landau, “On the theory of superconductivity”, *Zh. Eksperim. i Teor. Fiz.*, Vol. **20**, 1064 (1950).
- [5] A. A. Abrikosov, “Magnetic properties of superconductors of the second group”, *Zh. Eksperim. i Teor. Fiz.*, Vol. **32**, 1442 (1957).
- [6] M. Tinkham, *Introduction to superconductivity*, Second edition, McGraw-Hill, New York, USA (1996).
- [7] R. E. Glover, III, and M. Tinkham, “Transmission of superconducting films at millimeter-microwave and far infrared frequencies”, *Phys. Rev.*, Vol. **104**, 844 (1956).
- [8] D. C. Mattis, and J. Bardeen, “Theory of the anomalous skin effect in normal and superconducting metals”, *Phys. Rev.*, Vol. **111**, 412 (1958).
- [9] R. E. Glover, III, and M. Tinkham, “Conductivity of superconducting films for photon energies between  $0.3$  and  $40kT_c$ ”, *Phys. Rev.*, Vol. **108**, 243 (1957).
- [10] G. de Lange, J. J. Kuipers, T. M. Klapwijk, R. A. Panhuyzen, H. van de Stadt, and M. W. M. de Graauw, “Superconducting resonator circuits at frequencies above the gap frequency”, *J. Appl. Phys.*, Vol. **77**, 1795 (1995).
- [11] L. I. Berger, “Fermi energy and related properties of metals”, in *CRC Handbook of Chemistry and Physics, 88th Edition (Internet Version 2008)*, D. R. Lide, Ed., CRC Press/Taylor and Francis, Boca Raton, FL, USA.

- [12] V. Ambegaokar, and A. Baratoff, “Tunneling between superconductors”, Phys. Rev. Lett., Vol. **10**, 486 (1963); erratum, Vol. **11**, 104 (1963).
- [13] B. D. Josephson, “Possible new effects in superconductive tunnelling”, Phys. Lett., Vol. **1**, 251 (1962).
- [14] B. D. Josephson, “Supercurrents through barriers”, Adv. Phys., Vol. **14**, 419 (1965).
- [15] A. Barone and G. Paternò, *Physics and applications of the Josephson effect*, John Wiley & Sons, New York, USA (1982).
- [16] P. K. Tien and J. P. Gordon, “Multiphoton process observed in the interaction of microwave fields with the tunneling between superconductor films”, Phys. Rev., Vol. **129**, 647 (1963).
- [17] S. Shapiro, “Josephson currents in superconducting tunneling: the effect of microwaves and other observations”, Phys. Rev. Lett., Vol. **11**, 80 (1963).
- [18] J. R. Tucker and M. J. Feldman, “Quantum detection at millimeter wavelengths”, Rev. Mod. Phys., Vol. **57**, 1055 (1985).
- [19] N. R. Werthamer, “Nonlinear self-coupling of Josephson radiation in superconducting tunnel junctions”, Phys. Rev., Vol. **147**, 255 (1966).
- [20] P. Dieleman, H. G. Bukkems, T. M. Klapwijk, M. Schicke, and K. H. Gundlach, “Observation of Andreev reflection enhanced shot noise”, Phys. Rev. Lett., Vol. **79**, 3486 (1997).
- [21] M. J. Feldman, “Quantum noise in the quantum theory of mixing”, IEEE Trans. Magnetics, Vol. **MAG-23**, 1054 (1987).
- [22] A. R. Kerr, “Suggestions for revised definitions of noise quantities, including quantum effects”, IEEE Trans. Microwave Theory and Techn., Vol. **47**, 325 (1999).

## Chapter 3

# Requirements for tunneljunctions based on ALMA Band 9 (602 - 720 GHz)

The research described in this Thesis has been done in order to realize the best possible receivers for the 602 to 720 GHz band (Band 9) of the Atacama Large Millimeter Array (ALMA). In this Chapter, we will first explain why this band has been chosen (3.1), and secondly what the specifications for the receivers of this band are (3.2). After that, we will go deeper into the motivation for the requirements of bandwidth (3.3) and noise temperature (3.4).

### 3.1 Choice of Band 9

ALMA will be the leading instrument for studying the ‘cool’ universe: the radiation remnant of the Big Bang, the molecular gas and dust that are the building blocks of galaxies, stars, planetary systems, and also, life. This material has a typical temperature in the range of 3 to 100 K, which translates into the submillimeter to far infrared part of the electromagnetic spectrum: about 60 to 2000 GHz.

In fact, most of the energy in the universe lies in two thermal components: the cosmic background and the far infrared background. The spectra of these two are accessible from earth and lie within the ALMA frequency coverage. The peak of the spectral energy distribution for dusty objects in the distant universe becomes completely redshifted to submillimeter wavelengths. A number of current and future telescopes will operate at these wavelengths to exploit the enormous information that they conceal, but none will have the combination of sensitivity, resolution, and frequency coverage that ALMA will have [1].

The requirement for ALMA is that it will have the flexibility to support the investigations that will be proposed by scientists over the decades long lifetime of the instrument. However, the design and size of ALMA are determined by three primary scientific goals, that stand out in all the scientific planning, namely [2]:

1. *The ability to detect spectral line emission from CO or CII in a normal galaxy like the Milky Way at a redshift of  $z = 3$ , in less than 24 hours of observation.*
2. *The ability to image the gas kinematics in protostars and in protoplanetary disks around young Sun-like stars at a distance of 150 pc (roughly the distance of the star-forming clouds in Ophiuchus or Corona Australis), enabling the study of their physical, chemical and magnetic field structures and to detect the tidal gaps created by planets undergoing formation in the disks.*
3. *The ability to provide precise images at an angular resolution of 0.1 arcsec. Here the term ‘precise image’ means being able to represent, within the noise level, the sky brightness at all points where the brightness is greater than 0.1% of the peak image brightness.*

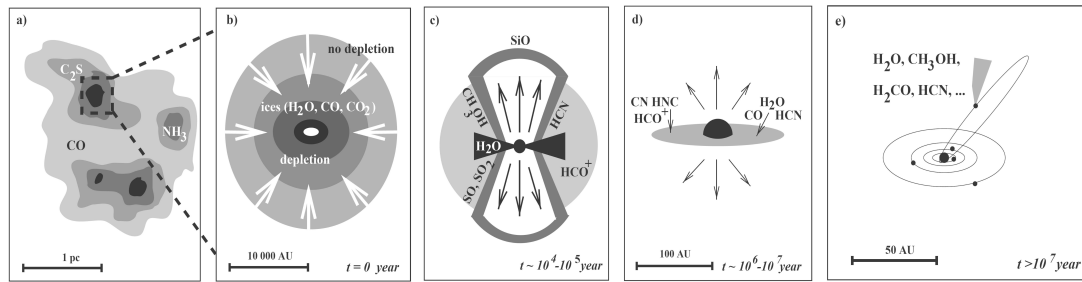


**Figure 3.1:** A schematic view of low-mass star formation. (a) Dark cloud cores, roughly 1 pc in size, gradually contract until (b) magnetic support is overcome and inside-out collapse begins at  $t = 0$ . (c) For  $\sim 10^4 - 10^5$  years, a phase of both high accretion and supersonic outflow occurs in deeply embedded protostars (young stellar objects). (d) Gradual clearing by the outflow leaves only the young T Tauri star and a residual protoplanetary accretion disk, which, on time scales of  $10^6 - 10^7$  years, leads to the formation of a mature planetary system (e). Characteristic molecules at each of these stages are indicated. Images and caption reproduced from Van Dishoeck and Blake [3].

In order to achieve those science goals, ALMA will cover the frequency range of 31 to 950 GHz, but a decreased atmospheric transmission of certain frequencies due to the presence of water causes this range to be divided into 10 bands. We focus on Band 9, from 602 to 720 GHz. The choice of this band has two reasons. First, the Dutch astronomical community has a large interest in interstellar chemistry during star formation [3]. For each of the stages of star formation, there are characteristic molecules (illustrated by Fig. 3.1), which have emission lines in the range of Band 9. Therefore, Band 9 has a huge scientific potential for Dutch astronomy [4, 5]. Secondly, there is a large experience in the Dutch consortium consisting of Delft University of Technology and SRON Netherlands Institute of Space Research with the development of SIS mixers for this frequency band [6, 7, 8] as well as ongoing research on adjacent bands for the HIFI project [9, 10].

The Band of choice being determined, we will discuss in the next Section the specifications the astronomers have set to accommodate their scientific proposals.

## 3.2 ALMA Band 9 specifications

The ALMA Band 9 has a well documented set of technical specifications, of which we will now list the ones with the biggest implications for the development of the SIS mixers for Band 9 [11].

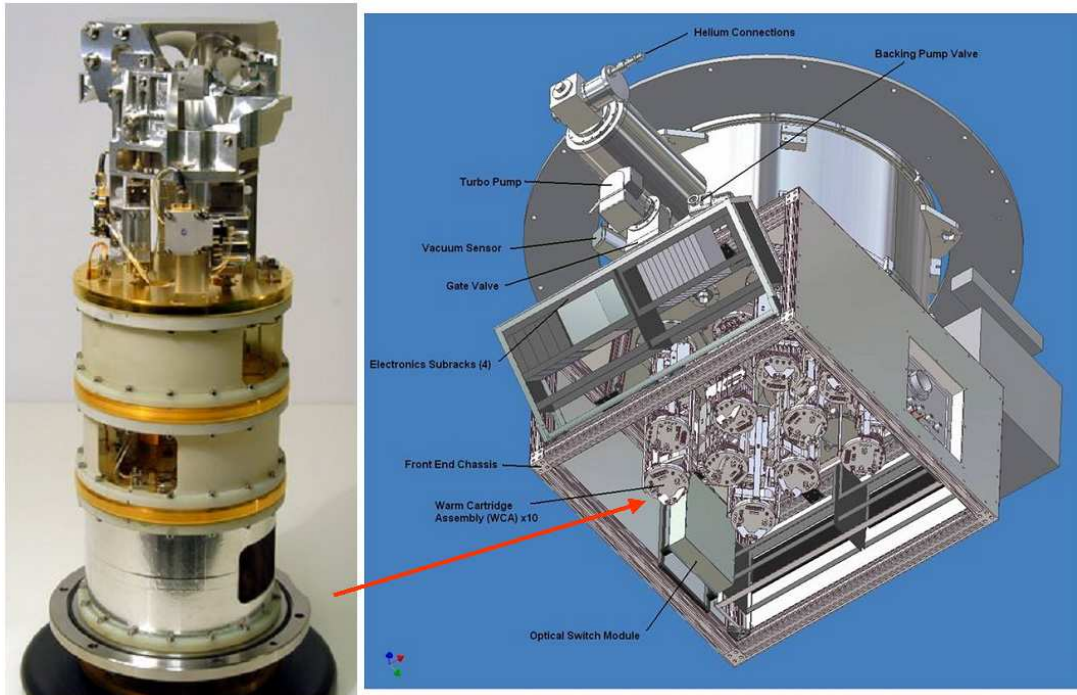


**Figure 3.2:** Left, photograph of Band 9 Cartridge (image courtesy R. Hesper, SRON Netherlands Institute for Space Research); right, schematic drawing (bottom view) of front end dewar with inserted cartridges (image courtesy National Radio Astronomy Observatory (NRAO), Charlottesville, USA). The arrow indicates one of the cartridges.

### 3.2.1 Description of Band 9 Cartridge

All the equipment for Band 9, constituting cold optics (feed horn, mirrors, polarizing grids), components to couple the LO to the mixers, IF amplifiers, sensors for monitoring, any type of necessary interconnects, and the two mixers (one per polarization direction), is referred to as the Band 9 *Cartridge*.

The Band 9 Cartridge is thus one of the receiver cartridges that populate the front end dewar. This is illustrated in Fig. 3.2.

### 3.2.2 General requirements

The following table lists two general requirements that are important for the development of SIS mixers.

Subject	Specification
Series production	The design shall be such that production and assembly costs are minimized to allow for a moderate form of series production.
Mechanical tuning	No mechanical tuning shall be used during operation.

### 3.2.3 Functional requirements

We will now tabulate the functional requirements that are important from SIS mixer point of view.

Subject	Specification
Mixer type	An SIS mixer shall be used as the frequency translating device.
Mixing scheme	Each polarization channel shall have a DSB mixing scheme. Both polarizations shall have the same mixing scheme.
RF input port	The RF input frequency shall range from 602 to 720 GHz.
LO input port	The LO input frequency shall range from 610 to 712 GHz.
IF output port	The IF bandwidth shall be 8 GHz DSB, centered at 8 GHz (consequently, from 4 to 12 GHz).
Polarization	Two polarizations shall be received, designated ‘Polarization 0’ and ‘Polarization 1,’ with each converted to a separate IF input.

### 3.2.4 Performance requirements

The performance of ALMA is characterized by its sensitivity. The official ALMA technical specification reads [2]:

*ALMA shall routinely obtain sub-milliJansky point source sensitivity at all observing frequencies, within ten minutes of integration time, under median atmospheric conditions*

We will analyze this requirement further in Subsection 3.4.2, but for the specification of the performance of the Band 9 Cartridge, it translates to a requirement for the noise temperature. The cartridge noise temperature specification is as follows:

Maximum DSB $T_n$ over 80 % of frequency range	168 K
Maximum DSB $T_n$ at any RF frequency	250 K

The cartridge noise temperature includes the noise contributions from dewar windows and IR filters and must take into account all the noise contributions up to the cartridge IF output ports. The following remarks apply to the table above:

- Frequency and frequency range as specified in Subsection 3.2.3;
- $T_n$  shall be calculated from the measurements, according to the Rayleigh-Jeans law;
- The noise powers shall be measured for an operating temperature of  $4 \pm 0.25$  K at the mixer block;
- The stated cartridge noise temperatures are based on an LO noise contribution of sideband noise no more than  $10 \text{ K}/\mu\text{W}$ .

### 3.3 Motivation for bandwidth requirements

The functional requirements, listed in Subsection 3.2.3, mostly concern the bandwidth of the mixer, at the RF, LO, and IF ports. In this Section, we will focus on the bandwidth at the RF input port, which ranges from 602 to 720 GHz. In the first two Subsections, we will explain how this bandwidth was determined, whereas in the third Subsection, we will discuss the considerations for an SIS mixer to meet this requirement.

#### 3.3.1 Water absorption: atmospheric window

Because of the very high sensitivity that ALMA will have, it is pointless to let the frequency coverage be determined by a certain list of critical transitions, that the instrument will aim for. There will literally be thousands of lines observable from millions of celestial objects. Thus, ideally, the whole range from 30 to 950 GHz should be covered.

However, since ALMA will be located on earth, the atmosphere has to be taken into account [4]. Molecules (most eminently, water and oxygen) in the earth atmosphere absorb certain frequencies strongly, making it practically impossible to observe anything from space at these frequencies. Oxygen blocks the frequency ranges 45 to 67 GHz and 116 to 125 GHz; ground state transitions of water obstruct transmission in the bands 373-385 GHz, 500-602 GHz, and 720-787 GHz. Therefore, the ALMA frequency range is divided into 10 bands, as shown in Fig. 1.2, which also shows the atmospheric transmission at the site. Band 9 (from 602 to 720 GHz), which we are focusing on, is thus set by the atmospheric water absorption at the adjacent frequency bands 500-602 GHz and 720-787 GHz.

#### 3.3.2 Astronomically important spectral lines

As mentioned in the previous Subsection, the planned sensitivity of ALMA enables the detection of thousands of spectral lines from millions of different objects. From an astrochemical point of view, all lines are equally important. Therefore, the frequency coverage of ALMA is only limited by the atmospheric transmission.

In Bands 9 and 10, the most important spectroscopic targets are the higher excitation transitions of abundant molecules and the fundamental transitions of lighter molecules. Dust emission from cool condensations and redshifted galaxies will provide important continuum targets.

The Atacama Pathfinder Experiment (APEX) is a modified ALMA prototype antenna which is operating as a single dish near the site of ALMA. It is doing exploratory science as a preparation for ALMA. A receiver from the Carbon Heterodyne Array of the Max Planck Institute (CHAMP+) can be installed on APEX to do 7 pixel observations in the atmospheric windows 602 - 720 GHz (CHAMP+ Low) and 780 - 950 GHz (CHAMP+ High). The CHAMP+ Low

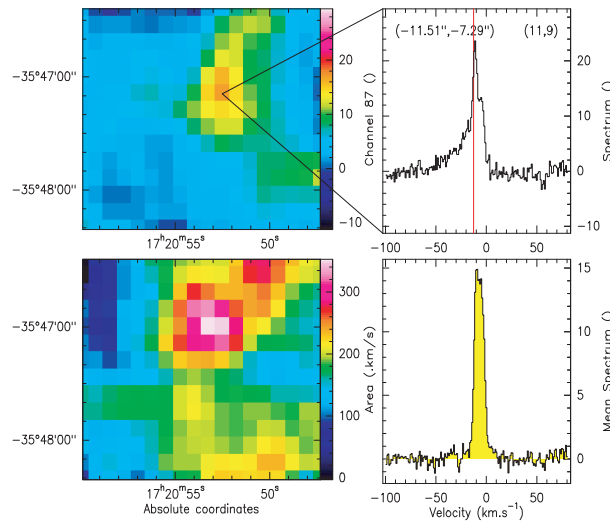


**Figure 3.3:** Preliminary results with CHAMP+ on APEX at a frequency of 691.47 GHz (CO 6-5 transition) in the celestial object NGC 6334 (also known as the Cat’s Paw Nebula or Bear Claw Nebula), obtained with devices developed in the research of this Thesis. Image courtesy of the Max Planck Institute for Radio-astronomy, Bonn, Germany.

window is equal to ALMA Band 9, and is using 2 times 7 mixers that have been developed in the research of this Thesis. Preliminary results with CHAMP+ on APEX (using our SIS junctions) are shown in Fig. 3.3, for the spectral line of the CO 6-5 transition.

To get an idea of what kind of spectrums could be observed for the whole range of Band 9 of ALMA, Fig. 3.4 shows a spectrum for the range of 607 to 725 GHz that has been taken with the Caltech Submillimeter Observatory (CSO) telescope, situated near the summit of mount Mauna Kea, on Hawaii.

### 3.3.3 Bandwidth analysis

From the point of view of the astronomer, Band 9 should range from 602 to 720 GHz, but the question remains if it is possible for an SIS mixer to have such a large bandwidth. This Subsection deals with the analysis of the bandwidth of an SIS detector.

In general, the achievable match between a capacitive device and a (resistive) source is limited by the  $RC$  product of the device, where  $R$  is its resistance, and  $C$  its capacitance. The lower  $RC$ , the higher the possible bandwidth  $\Delta f$ . More precisely [13],

$$\int_0^{\infty} \ln \left| \frac{1}{\rho_c(f)} \right| df \leq \frac{1}{2RC}, \quad (3.1)$$

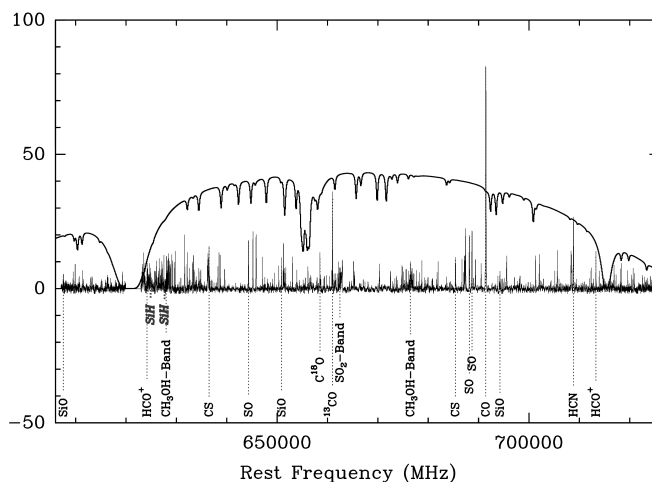


**Figure 3.4:** 607-725 GHz spectrum of Orion-KL obtained with the Caltech Submillimeter Telescope on Mauna Kea, Hawaii. Overlaid is a plot of the zenith atmospheric transmission for 1 mm precipitable water vapor at Mauna Kea. Reproduced from Schilke *et al.* [12].

where  $\rho_c$  is the reflection coefficient at the input of the device. The relation between  $\Delta f$  and  $RC$  becomes more obvious if one rewrites Eq. 3.1 for  $\rho_c = \rho_a$  for a frequency range  $f_1$  to  $f_2$  (with  $f_2 - f_1 = \Delta f$ ), and  $\rho_c = 1$  elsewhere:

$$\ln \left| \frac{1}{\rho_a} \right| \Delta f \leq \frac{1}{2RC}. \quad (3.2)$$

This equation is known as the Bode formula. It shows that, in order to define a bandwidth  $\Delta f$ , one simultaneously has to specify a maximum reflection coefficient  $\rho_a$  (or, equivalently, a minimum transmission coefficient), that the device is allowed (or required) to have in the band.

As it was briefly mentioned in Subsection 2.2.3, an SIS junction is electrically represented not only by a voltage (and radiation) dependent resistor, but also a capacitor. Hence, the bandwidth of an SIS detector is related to its  $RC$  product. The junction capacitance  $C_j$  is determined by the junction area  $A_j$ , and the barrier material and thickness ( $t_{bar}$ ), assuming a parallel plate capacitor:

$$C_j = \frac{\epsilon_0 \epsilon_r A_j}{t_{bar}} = C_s \times A_j, \quad (3.3)$$

with  $\epsilon_0$  the permittivity of free space and  $\epsilon_r$  the relative permittivity (dielectric constant) of the barrier material. For a given barrier with its physical properties, this defines a specific capacitance  $C_s$ .

For RF matching purposes, it is sufficient to represent the resistive behavior of an SIS junction by its normal state resistance  $R_n$ .  $R_n$  depends on the barrier

material, growth (see Chapters 5 and 7) and thickness. Simmons [14] derived a formula which is valid for low voltage biases  $V$ :

$$J_t = \frac{3\sqrt{2m\phi_0}}{2t_{bar}} \left(\frac{e}{h}\right)^2 V e^{-\frac{4\pi t_{bar}\sqrt{2m\phi_0}}{h}}, \quad (3.4)$$

where  $J_t$  is the tunnel current density,  $\phi_0$  is the energy barrier height of the barrier material and  $m$  is the mass of an electron. We see that the exponent in Eq. 3.4 is equal to the exponent of our derived Eq. 2.23, if we substitute  $t_{bar} = a$  and  $\phi_0 = U_0 - E_0$ . The difference in prefactor originates in the conversion from the tunneling probability of a particle in a one-dimensional system in Eq. 2.23 to the tunneling current density of a three dimensional system in Eq. 3.4.

For a junction with both  $\phi_0$  and  $t_{bar}$  homogeneous over the junction area  $A_j$ , Eq. 3.4 yields

$$R_n = \frac{2t_{bar}}{3A_j\sqrt{2m\phi_0}} \left(\frac{h}{e}\right)^2 e^{\frac{4\pi t_{bar}\sqrt{2m\phi_0}}{h}} = \frac{R_n A}{A_j}. \quad (3.5)$$

If we multiply a junction's  $R_n$  with its area  $A_j$ , we get the barrier specific resistance times area product  $R_n A$ .

We now see immediately that the  $R_n C_j$  product of an SIS junction depends on the barrier height and thickness, but not on the junction area, since the  $A_j$ 's of Eqs. 3.3 and 3.5 cancel out. In formula, we find

$$\begin{aligned} R_n C_j &= \frac{2\epsilon_0\epsilon_r}{3\sqrt{2m\phi_0}} \left(\frac{h}{e}\right)^2 e^{\frac{4\pi t_{bar}\sqrt{2m\phi_0}}{h}} \\ &= R_n A \times C_s. \end{aligned} \quad (3.6)$$

This also illustrates that  $R_n C_j$  is fully defined by the barrier properties  $R_n A$  and  $C_s$ . By decreasing  $t_{bar}$ ,  $R_n C_j$  decreases exponentially, in spite of the increase of  $C_s$ .

If we want a reflection coefficient not larger than 0.05, we find that for typical values of niobium - aluminum oxide - niobium SIS junctions,  $R_n A = 25 \Omega\mu\text{m}^2$  and  $C_s = 65 \text{ fF}/\mu\text{m}^2$ ,<sup>i</sup> the Bode formula 3.2 yields a maximum bandwidth of about 103 GHz. This indicates already that obtaining the required ALMA Band 9 bandwidth (118 GHz) is a challenging task.

To achieve a wider bandwidth with our SIS junctions, we have introduced a more reliable process to grow high critical current density AlN tunnel barriers than what has been available up to now (Chapters 5 and 7). Replacing the conventionally used AlO<sub>x</sub> barriers, this leads to devices with an unprecedented high performance over a very large bandwidth, discussed in Chapter 8.

<sup>i</sup>For a list of material parameters, relevant for this research, see Section 8.7.

### 3.4 Motivation for noise temperature requirements

The noise performance requirements, detailed in Subsection 3.2.4 are motivated from an astronomer's point of view and analyzed from the perspective of a device physicist.

#### 3.4.1 Integration time

There are many sources in the sky that ALMA aims to detect. The intensity of a source can be represented by a temperature,  $T_s$ , provided a well calibrated detector, with a known system noise temperature  $T_{n,sys}$ . For example, in Fig. 3.4, the spectral lines have  $T_s$  varying from less than 5 to more than 80 K.

It is evident that the minimum  $T_s$  that can be observed with a telescope (or multiple telescopes) depends on  $T_{n,sys}$ . But also, for a longer observation time, more sensitive measurements can be performed. The observation time is alternatively called *integration time*,  $t_{int}$ , because the source signal effectively gets integrated to obtain a better signal to noise ratio. This behavior is captured in the radiometer equation, which yields

$$\frac{\delta T_s}{SNR} = \frac{T_{n,sys}}{\sqrt{t_{int}\Delta f_{IF}}}, \quad (3.7)$$

where  $\delta T_s$  is the minimum source temperature, observed with a signal to noise ratio  $SNR$ , and  $\Delta f_{IF}$  the IF bandwidth.

To observe a specific source on the sky, astronomers usually integrate as long as necessary until the  $SNR$  is large enough (that is, at least 1, but preferably larger). If we rewrite Eq. 3.7 for  $SNR = 1$  as

$$t_{int} = \left( \frac{T_{n,sys}}{\delta T_s} \right)^2 \frac{1}{\Delta f_{IF}}, \quad (3.8)$$

we see that when  $T_{n,sys}$  is halved, only a quarter of the integration time is needed. Because of this quadratic behavior, even a small improvement of  $T_{n,sys}$  reduces the observation time considerably. Therefore, from an astronomer's point of view, the system noise temperature should be as low as possible. This greatly enhances the use through short observation times, and, as a consequence, more observations of different objects.

Improving the noise temperature of the SIS detectors is an economically wise choice, because to obtain similar results with a higher noise temperature, one would have to increase the size of the telescopes, a much more expensive route. Hence, a low noise temperature creates a big return on investment for the billion dollar instrument that ALMA is.

### 3.4.2 Flux density sensitivity

In astronomy, the brightness of a celestial source is represented by its *flux density*,  $S$ . It is defined as

$$S = \frac{P_s}{A_{col}\Delta f}, \quad (3.9)$$

where  $P_s$  is the measured power of the source at the observation site and  $A_{col}$  the total collecting area of the telescope system. The bandwidth  $\Delta f$  is either the bandwidth of an observed spectral line, or the IF bandwidth in the case of a continuum source. Although the SI unit of  $S$  is  $\text{Wm}^{-2}\text{Hz}^{-1}$ , astronomers usually use the unit Jansky (Jy), defined as

$$1 \text{ Jy} = 10^{-26} \frac{\text{W}}{\text{m}^2\text{Hz}}, \quad (3.10)$$

to work with more appropriate numbers. The performance requirement of Subsection 3.2.4 thus requires a routine sensitivity of ALMA of less than a mJy, or  $10^{-29} \text{ Wm}^{-2}\text{Hz}^{-1}$ .

For the flux density sensitivity,  $\Delta S$ , of an image made from interferometric array data, we can write [15]:

$$\Delta S = \frac{4\sqrt{2}k_B T_{n,sys}}{\gamma_g \eta_q \eta_a \pi D_{ant}^2 \sqrt{n_p [N_{ant}(N_{ant} - 1)/2]} t_{int} \Delta f}, \quad (3.11)$$

where  $\eta_a$  is the antenna aperture efficiency,  $\eta_q$  is the correlator quantization efficiency,  $D_{ant}$  is the antenna diameter,  $n_p$  is the number of simultaneously sampled polarizations and  $N_{ant}$  is the number of antennas in the array.  $\Delta f$  is defined as in Eq. 3.9.

Following Butler et al. [15], who analyze the parameters of Eq. 3.11 for the relevance of ALMA, we take  $N_{ant} = 64$ ,  $n_p = 2$ ,  $D = 12$ ,  $\eta_q = 0.95$ , and  $\eta_a = 0.48$  for a frequency of 675 GHz. They take a moderate  $t_{int} = 60$  s, and  $\Delta f = \Delta f_{IF} = 8$  GHz for a continuum source and  $\Delta f = f\Delta v/c$  for a spectral line with a velocity width  $\Delta v$ , which just leaves  $\Delta S$  dependent on  $T_{n,sys}$ .

$T_{n,sys}$  depends on the cartridge (or receiver) noise temperature, the temperature of the sky, the antenna, and the cosmic microwave background (CMB) radiation:

$$T_{n,sys} = T'_{rx} e^{\tau_0 m_a} + \eta_l T'_{atm} (e^{\tau_0 m_a} - 1) + (1 - \eta_l) T'_{sbr} e^{\tau_0 m_a} + T'_{cmb}, \quad (3.12)$$

with  $T'_{rx}$  the receiver noise temperature,  $\tau_0$  the opacity of the atmosphere at zenith,  $m_a$  is the airmass,  $\eta_l$  is the fraction of the antenna power that is received in the forward direction,  $T'_{atm}$  is the effective atmospheric temperature,  $T'_{sbr}$  is the effective temperature onto which the spillover falls, and  $T'_{cmb}$  is the CMB

**Table 3.1:** Flux density sensitivity, for continuum and for 1 km/s channel spectral line observations, for different precipitable water vapor values (pwv), all in 1 minute integration time.

pwv	0.35 mm	1.5 mm
$\Delta S_{cont}$	0.36 mJy	3.0 mJy
$\Delta S_{1km/s}$	22 mJy	180 mJy

effective temperature. The primes on the temperatures indicate that they are effective radiation temperatures, calculated with a Planck correction [16]:

$$T'_x = \frac{hf/k_B}{e^{hf/k_B T_x} - 1}, \quad (3.13)$$

where  $T_x$  is the physical temperature. Further it is assumed [15] that  $T_{sbr} = T_{amb} = 269$  K, the average surface temperature at the ALMA site, that  $T_{atm} = 70.2 + 0.72T_{amb}$  [17], resulting in  $T_{atm} = 264$  K, that  $T_{cmb} = 2.7$  K, and that the telescope elevation is  $50^\circ$ .

Butler et al. [15] now calculate the system noise temperature by taking an estimated *single* sideband noise temperature of  $T_{rx} = 4hf/k_B + 4$ , which is not completely correct for Band 9, where DSB mixers will be used, but it serves as a workable approximation. Thus,  $T_{rx} = 150$  K, which is in line with the specification given in Subsection 3.2.4.

The resulting calculated flux density sensitivities for different precipitable water vapor (pwv) values are listed in Table 3.1. A distinction is made between continuum observations in the entire 8 GHz IF band, resulting in a sensitivity  $\Delta S_{cont}$ , and spectral line observations in a velocity channel of 1 km/s, resulting in a sensitivity  $\Delta S_{1km/s}$ .

Clearly, for a continuum observation of a point source, sub-mJy sensitivities can be reached. This is even more the case for 10 minute integration times, decreasing the values in Table 3.1 with a factor  $\sqrt{10} \approx 3.2$ . Hence, the noise temperature specification of ALMA Band 9 ( $T_n < 168$  K for 80 % of the frequency range) is sufficient to comply to the general ALMA requirement for the sensitivity.

### 3.4.3 Noise temperature and device properties

The main question that remains for the device physicist, is how to realize SIS junctions that result in a cartridge noise temperature lower than 168 K, which is about  $5hf/k_B$ : a few times the quantum limit for a mixing device. In the design

of these devices, several aspects have to be taken into account, assuming that the transmission of the signal to the device has been maximized.

We can distinguish between aspects that influence the noise temperature because they affect the amount of signal that comes out of the device, and aspects that affect the noise itself, generated in the system.

First, the signal is influenced by the antenna design of the device: it has to be optimized to ensure that the incoming signal is well picked up by the RF feed point. A non-optimized design would reduce the transmission, effectively increasing the noise temperature.

Secondly, to reduce the noise of the system, the losses in the microstripline that transfers the signal to the SIS junction should be as low as possible. To minimize these losses, this line is usually made of a superconducting material, in our work typically niobium, in correspondence with the SIS electrodes, which are also made of niobium. For Band 9, this is of particular importance, because the gap frequency of niobium (about 680 GHz), beyond which increased losses occur, lays in the range 602 to 720 GHz. Less losses result in a lower  $T_n$ . To achieve a better result, we have studied the properties of the niobium microstriplines, which will be discussed in Chapters 6 and 8.

Furthermore, also the geometrical dimensions of the discussed microstripline have to be optimized, to tune the input impedance of the antenna to the SIS junction. This will determine not only the bandwidth of the mixer, but also the absolute value of the transmission efficiency of the signal to the junction. Because of the Bode limitation (Eq. 3.2), there is a tradeoff between bandwidth and transmission. A higher transmission efficiency decreases the noise temperature. We investigate the effect of the geometry of the microstriplines in Chapters 6 and 8.

Finally, the SIS junction itself plays a crucial role in the reduction of the noise temperature. A ‘real life’ SIS junction will differ from an ideal device, as has already been pointed out in Chapter 2. This non-ideality of SIS junctions will be discussed further in Chapter 5, but we will also spend a few words on it here. First of all, current can flow through the barrier at bias voltages lower than  $V_{gap}$ , due to thermal excitations of quasiparticles and higher-order tunneling processes, called multiple Andreev reflections (MAR) [18, 19]. These MAR cause the emergence of excess shot noise [20], increasing the noise temperature of the device. Further, *gap smearing* can occur, a broadening in voltage of the current-rise around the gap voltage, which can be due to a non-uniformity in the superconducting properties of the electrodes, or to a nonzero lifetime broadening parameter  $\Gamma$ . This effect will reduce the responsivity and therefore the amount of signal, effectively causing an increase of the noise temperature.

## 3.5 Conclusion

This Chapter discusses the technical requirements of ALMA Band 9 that are important for this work. We have seen that the matching of the bandwidth of the SIS junctions to Band 9 of ALMA requires knowledge and control of the properties of the junction and the tuning microstripline. There is a tradeoff between the maximization of the bandwidth of a device and the minimization of its noise temperature. This tradeoff should be well analyzed in order to obtain the optimum performance for Band 9. The next Chapters will concentrate on this subject.

## References

- [1] An overview of the science that will be done with ALMA can be found at the website: <http://www.eso.org/projects/alma/science/>
- [2] Transcribed from “ALMA scientific specifications and requirements”, initial version by B. Butler, S. Guillotereau, E. van Dishoeck, and A. Wootten, Doc. no. ALMA-90.00.00.00-001-A-SPE (2004).
- [3] E. F. van Dishoeck and G. A. Blake, “Chemical evolution of star-forming regions”, *Annu. Rev. Astron. Astrophys.*, Vol. **36**, 317 (1998).
- [4] A. Wootten, L. Snyder, E. van Dishoeck, and F. Owen, “MMA frequencies working group: frequency band considerations and recommendations”, ALMA Memo 213 (1998). A list of ALMA Memos can be found at the website: <http://www.alma.nrao.edu/memos/index.html>
- [5] E. Van Dishoeck, “From molecular clouds to planets: prospects for ALMA”, in *The origin of stars and planets: the VLT view*, Eds. J. Alves, W. Brandner, E. F. van Dishoeck, R. Mundt, H. Zinnecker, C. Lada, M. J. McCaughrean, R. Siebenmorgen, S. Wolf, and R. Neuhäuser, Springer, Berlin/Heidelberg, Germany, 67 (2002).
- [6] G. de Lange, C. E. Honingh, J. J. Kuipers, H. H. A. Schaeffer, R. A. Panhuyzen, T. M. Klapwijk, H. van de Stadt, and M. W. M. de Graauw, “Heterodyne mixing with Nb tunnel junctions above the gap frequency”, *Appl. Phys. Lett.* Vol. **64**, 3039 (1994).
- [7] G. de Lange, J. J. Kuipers, T. M. Klapwijk, R. A. Panhuyzen, H. van de Stadt, and M. W. M. de Graauw, “Superconducting resonator circuits at frequencies above the gap frequency”, *J. Appl. Phys.*, Vol. **77**, 1795 (1995).
- [8] G. de Lange, C. E. Honingh, J. J. Kuipers, H. H. A. Schaeffer, R. A. Panhuyzen, T. M. Klapwijk, H. van de Stadt, and M. W. M. de Graauw, “Characterization of a 680-760 GHz SIS waveguide mixer”, *Int. J. Infrared and Millimeter Waves*, Vol. **17**, 61 (1996).

- 
- [9] T. de Graauw and F. P. Helmich, “Herschel-HIFI: The heterodyne instrument for the far infrared”, in *SP-460 The promise of the Herschel Space Observatory*, Eds. G. L. Pilbratt, J. Cernicharo, A. M. Heras, T. Prusti, and R. A. Harris, ESA Pub. Div., Noordwijk, The Netherlands, 45 (2001).
- [10] B. D. Jackson, G. de Lange, T. Zijlstra, M. Kroug, J. W. Kooi, J. A. Stern, and T. M. Klapwijk, “Low-noise 0.8-0.96- and 0.96-1.12-THz superconductor-insulator-superconductor mixers for the Herschel Space Observatory”, *IEEE Trans. Microwave Theory and Techn.*, Vol. **54**, 547 (2006).
- [11] The technical specifications of ALMA Band 9 have been extracted from: G. H. Tan, “Band 9 cartridge technical specifications”, Doc. no. FEND-40.02.09.00-002-B-SPE (2007).
- [12] P. Schilke, D. J. Benford, T. R. Hunter, D. C. Lis, and T. G. Phillips, “A line survey of Orion-KL from 607 to 725 GHz”, *The Astrophysical Journal Supplement Series*, Vol. **132**, 281 (2001).
- [13] H. W. Bode, *Network analysis and feedback amplifier design*, Van Nostrand, New York, USA (1945).
- [14] J. G. Simmons, “Generalized formula for the electric tunnel effect between similar electrodes separated by a thin insulating film”, *J. Appl. Phys.*, **34**, 1793 (1963).
- [15] B. Butler and A. Wootten, “ALMA sensitivity, supra-Thz windows, and 20 km baselines”, ALMA Memo 276 (1999). See also Ref. [4].
- [16] B. L. Ulich and R. W. Haas, “Absolute calibration of millimeter-wavelength spectral lines”, *Astrophys. J. Supp. Ser.*, Vol. **30**, 247 (1976).
- [17] M. Bevis, S. Businger, T. A. Herring, C. Rocken, R. A. Anthes, and R. H. Ware, “GPS meteorology: remote sensing of atmospheric water vapor using the global positioning system”, *J. Geophys. Res.*, Vol. **97**, 15787 (1992).
- [18] T. M. Klapwijk, G. E. Blonder, and M. Tinkham, “Explanation of subharmonic energy gap structure in superconducting contacts”, *Physica B+C*, Vol. **109-110**, 1657 (1982).
- [19] A. W. Kleinsasser, R. E. Miller, W. H. Mallison, and G. B. Arnold, “Observation of multiple Andreev reflections in superconducting tunnel junctions”, *Phys. Rev. Lett.*, Vol. **72**, 1783 (1994).
- [20] P. Dieleman, H. G. Bukkems, T. M. Klapwijk, M. Schicke, and K. H. Gundlach, “Observation of Andreev reflection enhanced shot noise”, *Phys. Rev. Lett.*, Vol. **79**, 3486 (1997).



## Chapter 4

# Niobium technology

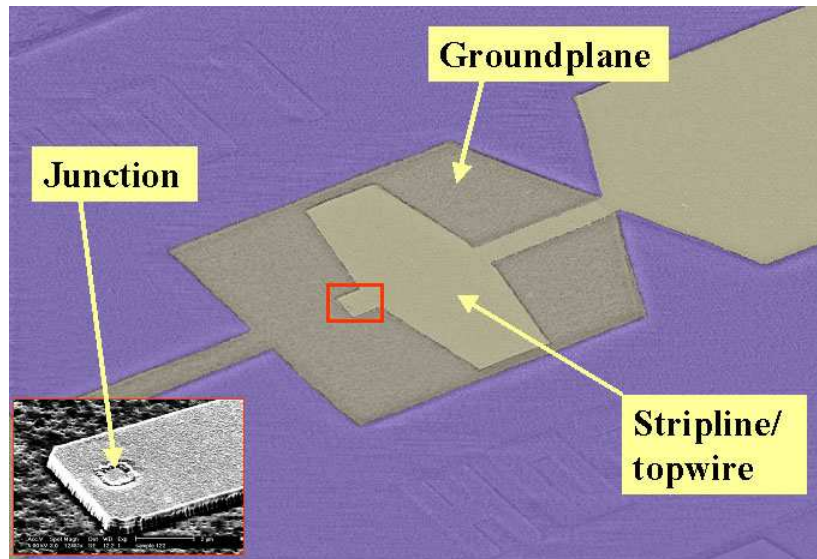


**Figure 4.1:** Scanning electron microscope (SEM) image (color-edited for better visibility) of a Nb/AIO<sub>x</sub>/Nb SIS device with a Nb/SiO<sub>2</sub>/Nb microstripline to tune out the geometrical capacitance of the junction. Groundplane and topwire are separated by SiO<sub>2</sub>. Inset: SEM image of (Nb/AIO<sub>x</sub>/Nb) SIS junction contacted by a Nb topwire.

In the previous Chapters, we have formulated the theoretical background of this work. We will now turn to the practical challenges that lay behind this theory: the development of both design and realization of SIS mixer devices. In this Chapter, we will focus on the realization of SIS devices. In Section 4.1, we will explain what we mean exactly by an SIS *device*, and discuss its layout. In Section 4.2 we motivate the choice of the various materials that are being used and Section 4.3 discusses the fabrication process. We will *not* go into the details of the tunneling barrier, since that is the subject of Chapter 5.

## 4.1 Device layout

In Fig. 4.1, a scanning electron microscope (SEM) image of an SIS device used in this work is shown. A device consists of a substrate, on which various materials have been deposited in well-designed patterns. Schematically, a device looks like the one in Fig. 4.2. In this Figure, the most important parts are labeled. A DC voltage bias is applied via the contact pads on the left and the right of the image. The high frequency signal couples into the device at the RF probe point and is transferred via the matching circuit (a microstripline) to the SIS junction. The IF filter blocks the RF signal from going to the leads.

The substrate is made of fused quartz. A 200 nm thick pattern of niobium (Nb) on the substrate is called the *ground plane*.

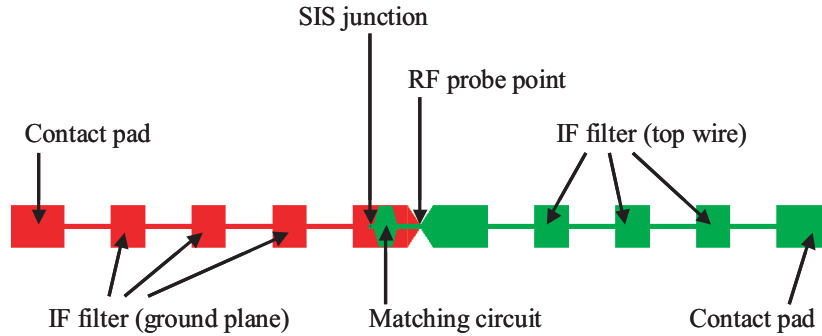


**Figure 4.2:** Schematic top view of an SIS device used in this work.

The top of the ground plane is a layer of about 5 - 7 nm of aluminum (Al), of which the upper 1 to 2 nm is oxidized or nitridized to form an insulating barrier of aluminum oxide ( $\text{AlO}_x$ ) or aluminum nitride (AlN). The 100 nm top electrode of the SIS is also made of Nb, and determines the junction size of about 0.4 to 1  $\mu\text{m}^2$ . The junction is the electrical connection to the 500 nm Nb *top wire*. Ground plane and top wire are separated by a 250 nm thick dielectric layer of silicon dioxide ( $\text{SiO}_2$ ). The top wire is designed such that it forms together with the ground plane and the dielectric a Nb -  $\text{SiO}_2$  - Nb microstripline to match the junction impedance to the antenna impedance at the RF probe point. The contact pads are made of approximately 50 nm gold (Au).

The positioning of the various layers is shown in Fig. 4.3, which gives a schematic cross-section of the SIS device, along its length. Compared to Fig. 4.2, the cross-section is taken horizontally, through the middle (where the junction is).

## 4.2 Motivation for choice of materials

In this Section, we have divided the materials of the device into four parts that we will discuss separately in the Subsections. In the last Subsection, we will consider the advantages and disadvantages of other materials that could be used.

### 4.2.1 Substrate: quartz

The substrate, which forms the ‘starting point’ from which a device is build, is made of fused quartz. Fused quartz is made by exposing naturally occurring quartz, which is a crystalline form of  $\text{SiO}_2$ , to high temperatures of about 2000°C. The substrate thickness for a finished device is 40  $\mu\text{m}$ , which is realized by thinning an originally 200  $\mu\text{m}$  thick substrate. Fused quartz as a substrate material is chosen for its low dielectric constant (3.75 at 20°C and 100 MHz) and low loss tangent (less than 0.0002 at 20°C and 1 MHz) [1]. Therefore, it is well suited to

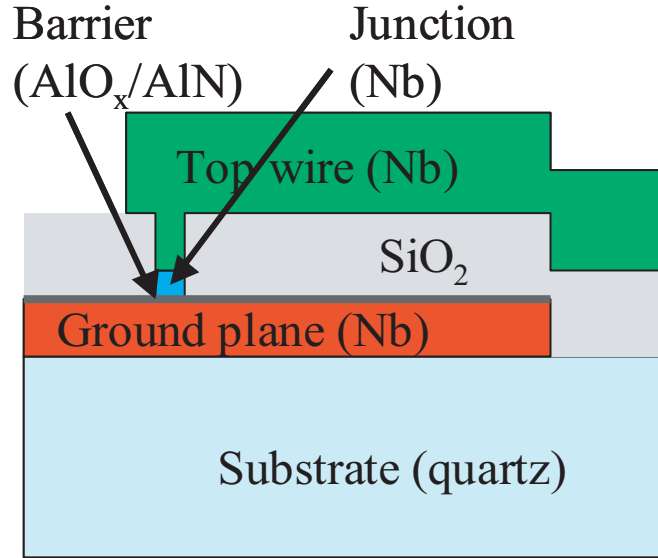


**Figure 4.3:** Schematic cross-section of an SIS device. The different layers are not drawn to scale with respect to each other.

minimize the substrate RF losses during mixer operation. Also, the thinning of a fused quartz substrate can be done by polishing it by hand. It has a low thermal expansion coefficient (about  $5.5 \times 10^{-7} \text{ K}^{-1}$  at  $20^\circ\text{C}$  [2]; *cf.* copper:  $165 \times 10^{-7} \text{ K}^{-1}$  at  $25^\circ\text{C}$  [3]), which is helpful for the mechanical stability while cooling it to temperatures as low as 4 K.

### 4.2.2 Junction electrodes: niobium

In this research, the junction electrodes are made of niobium. The bottom electrode is formed by the ground plane structure, the top electrode defines the junction size. Nb has a  $T_c$  of about 9.25 K [4], and is therefore superconducting at the temperature of liquid helium, 4.2 K. Using  $2\Delta(0) = 3.66k_B T_c$  rather than BCS formula Eq. 2.9 because of a stronger coupling between the electrons through the phonons [5], this gives  $2\Delta(0) = 2.92 \text{ meV}$ . At 4.2 K, solving Eq. 2.8 with this  $\Delta(0)$  yields  $2\Delta = 2.83 \text{ meV}$ . These values are for bulk niobium; in the next Subsection we will show measurements of  $T_c$  for thin films.

The most important reason to use Nb is its  $V_{gap} = 2\Delta(T)/e \approx 2.8 \text{ mV}$  at 4.2 K, which translates into a frequency  $f_{gap} = eV_{gap}/h \approx 680 \text{ GHz}$ . In principle, mixing is possible up to  $2f_{gap}$ , but in practice, losses in the tuning circuit increase considerably beyond  $f_{gap}$  (see, for example, Fig. 2.4). Still, devices with all Nb microstriplines have been demonstrated as a mixer for frequencies up to 840 GHz [6]. To circumvent the problem of losses at frequencies above  $f_{gap}$ , an alternative approach for the microstriplines is the use of superconductors with a higher  $f_{gap}$

(like niobium titanium nitride - NbTiN) and/or metals with a higher normal conductivity (e.g., Al). Heterodyne mixers using Nb/AlO<sub>x</sub>/Nb SIS junctions with NbTiN/SiO<sub>2</sub>/Al tuning circuits have been demonstrated for frequencies above 1100 GHz [7, 8], corresponding to  $1.6f_{gap}$ .

The uniformity of  $\Delta$  in the junction electrodes influences the sharpness of the  $IV$  curve near  $V_{gap}$ . The gap-rise also can become wider due to a nonzero lifetime broadening parameter  $\Gamma$ . Further, the gap width is affected by the local magnetic field and non-equilibrium effects in the electrodes, which can change the local temperature.

The behavior of the SIS junction obviously depends strongly on the nature of the tunneling barrier. In this Thesis, research has been done to replace AlO<sub>x</sub> by AlN to increase the bandwidth (Chapters 5, 7, and 8).

Other materials that are often used for SIS junction electrodes include niobium nitride (NbN) and niobium titanium nitride (NbTiN). (See Subsection 4.2.5.) Because of the technological maturity of the Nb process in our laboratories and the challenges of the ALMA project, Nb was preferred for the electrodes over other materials in order to minimize the risks. Also, for the frequency range of Band 9, Nb based junctions have the best performance.

### 4.2.3 Microstripline: Nb - SiO<sub>2</sub> - Nb

The microstripline transfers the RF signal from the RF probe point to the SIS junction. It is designed to match the antenna impedance to the junction impedance and consists of a ground plane, made of Nb, a dielectric layer of SiO<sub>2</sub> and a top wire of Nb. We study the properties of the microstriplines in detail in Chapter 6 and 8.

There are several reasons for the choice of Nb as the conducting material of the microstripline. First, because of the correspondence with the junction electrodes. The ground plane of the microstripline also serves as bottom electrode for the SIS junction. The top wire is a different layer than the top electrode of the SIS, but choosing the same material prevents for example the trapping of heat in the junction, which would occur if the top wire were made of a higher gap superconductor than niobium [9].

Secondly, the losses in the microstripline above  $f_{gap}$  decrease the SIS mixer performance, but are still low enough at the frequencies of our interest, up to 720 GHz. Below  $f_{gap}$ , the losses in the Nb ground plane and top wire have a negligible effect on the mixer performance. However, to make a proper design of the top wire geometry, the complete frequency dependent behavior of its surface impedance, calculated using Mattis-Bardeen theory for the complex conductivity [10], should be taken into account. We will address this in Chapter 6.

SiO<sub>2</sub>, deposited by RF magnetron sputtering from a SiO<sub>2</sub> target, has been chosen as the dielectric material of the microstripline because of its low loss tangent (0.0002 at 20°C and 1 MHz for the similar fused quartz [1]) and moderate



**Figure 4.4:** Bright field transmission electron micrograph [13] of a heterostructure of niobium, silicon dioxide, and niobium, on top of a (111) silicon substrate. This structure is the same as the microstripline that is being used in this work.

dielectric constant  $\epsilon_r \approx 3.8$  [6]. Further,  $\text{SiO}_2$  deposition equipment is readily available in our laboratories. Other groups have used thermally evaporated  $\text{SiO}$  [11], or epitaxially grown  $\text{MgO}$  (in combination with  $\text{NbN}$  as conducting material [12]).

A bright field transmission electron microscopy (TEM) image, showing a cross-section of the microstripline, can be found in Fig. 4.4 [13]. From this Figure, it can clearly be seen that the structure of the Nb which has been deposited on top of  $\text{SiO}_2$  is considerably different from the Nb deposited directly on the substrate. The  $\text{SiO}_2$  - Nb interface is very rough, and the grainsize of the Nb close to the  $\text{SiO}_2$  is smaller than further away.

As we will show (Chapters 6 and 8), we can predict the transmission efficiency of a microstripline if we choose in our simulations an equivalent high frequency normal conductivity  $\sigma_{RF} \approx 1 \times 10^7$  S/m, which is different from the generally used  $\sigma_{DC} \approx 2.5 \times 10^7$  S/m.

To validate this choice, we have measured four-point resistance ( $R$ ) - temperature ( $T$ ) profiles of Hall-bar devices. They were made of a bottom layer of 200 nm Nb, 250 nm  $\text{SiO}_2$  and a top layer of variable thickness that had the actual Hall-bar geometry. From the  $R(T)$  profiles we have extracted the DC normal conductivity  $\sigma_{DC}$  at 10 K and the  $T_c$  of the Nb films on top of  $\text{SiO}_2$ , as a function of thickness. The result is shown in Fig. 4.5. The relative error in the data is less than  $\pm 8$  %.

In the left graph of Fig. 4.5, we clearly see a sharp decrease of the conductivity in the films, starting at around 40 nm. In the right graph, we see a decrease in  $T_c$ , which indicates a decrease in the superconducting gap  $\Delta$ . From the conductivity measurements, we infer that the measured  $\sigma_{DC}$  is actually an average of the

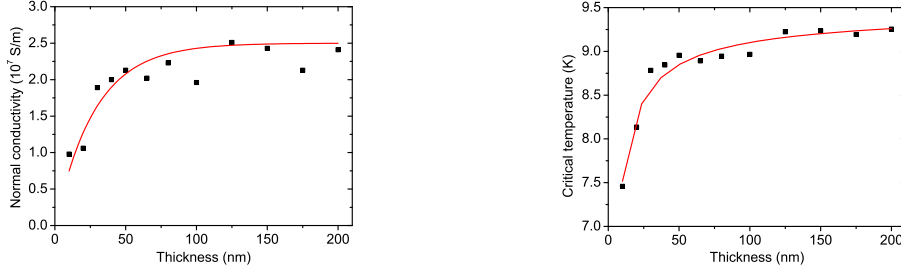


**Figure 4.5:** Variation of DC properties of a Nb film on top of  $\text{SiO}_2$  as a function of its thickness. Squares are measured values, averaged over 1-4 samples; full lines indicate a guide to the eye dependence. (Left) Normal state conductivity at 10 K. (Right) Critical temperature. Data collected by Noroozian [14].

position-dependent conductivity over the thickness of the film  $d$ :

$$\sigma_{DC} = \frac{\int_0^d \sigma(t') dt'}{d}. \quad (4.1)$$

Therefore, using  $\sigma_{DC}$  in the calculation of the surface impedance as if it were a constant, bulk material value, will not yield the right result. Hence, we have overcome this problem by introducing a  $\sigma_{RF}$ , as will be explained in Chapter 6.

The structure of the bottom conductor of the microstripline is affected when an anodization step is applied after junction definition (see Subsections 4.3.3 and 4.3.4). As a consequence, the equivalent high frequency normal conductivity of the bottom superconductor will also have a lower value than the bulk material. This effect will be analyzed in detail in Chapter 8.

In general, we can say that we have studied the properties of the superconducting microstriplines ( $\sigma_n$  and  $\Delta$  of top and bottom superconductor) in greater detail than what has been done in the past. A careful analysis reveals that one has to take into account all the processing steps in the choice of the material parameters, and cannot just take values based on different physical processes. For a list of the material parameters the research of this Thesis has led to, refer to Section 8.7.

#### 4.2.4 Contact pads: gold

The contact pads consist of 50 nm thick gold. Their purpose is to make electrical contact to the SIS device and allow the application of a (DC) voltage bias. This is done by making *wire-bonds* from the sample holder (or mixer holder) to the contact pads. Wire-bonds are thin (typically a few tens of  $\mu\text{m}$  in diameter) gold (or aluminum) wires that are welded to a metal surface, by a combination of heat, pressure and ultrasonic vibrations.

There are a few reasons why the contact pads are made of gold. First, gold is a good conductor (electrical resistivity of  $0.022 \mu\Omega\text{cm}$  [15]) and thus introduces very little parasitic resistance. Also, it is a noble metal, which almost does not oxidize, a good property for contact pads. Furthermore, the wire-bonds stick very well to gold, since they are made of gold themselves.

The contact pads are not shown in Fig. 4.3, but they are indicated in Fig. 4.2. At the side of the top wire, the contact pads are simply on top of the Nb, but at the ground plane side, there are *via*-holes in the  $\text{SiO}_2$  to make an electrical connection.

### 4.2.5 Considerations for other materials

To overcome problems with losses that could arise upon exceeding the gap frequency of Nb ( $\sim 680$  GHz), one might consider using higher gap superconductors. Two materials that have proven to be the most promising are NbN [16] and NbTiN [17].

NbN has a reported  $T_c$  up to 15.7 K and a  $V_{gap}$  of 5.9 mV, based on NbN/MgO/Nb SIS *IV* characteristics [18]. This corresponds to  $f_{gap} = 1.4$  THz. NbN initially appeared not to be a good replacement for Nb as the electrode material, because junctions with NbN, like NbN/MgO/NbN, have an excess shot noise due to multiple Andreev reflections [19]. Furthermore, NbN has a high surface resistance ( $60 \mu\Omega\text{cm}$  [18]) and low thermal conductivity ( $0.2 \text{ Wm}^{-1}\text{K}^{-1}$  at 20 K [20] *versus*  $1.17 \times 10^4 \text{ Wm}^{-1}\text{K}^{-1}$  for Al at 20 K [21]). However, recently Li *et al.* [22] have reported on the successful use of NbN/AlN/NbN SIS junctions combined with epitaxially grown NbN/MgO/NbN microstriplines for astronomical observations at a frequency (less demanding than in our research) of 500 GHz.

For NbTiN, measurements have indicated a  $T_c$  of 15.2 K, while SIS *IV*s indicate a gap voltage of 5.2 mV, corresponding to a  $f_{gap}$  of 1.2 THz [23]. NbTiN has a higher resistivity than Nb ( $\sim 60 \mu\Omega\text{cm}$ , depending on the deposition conditions [24] *versus*  $\sim 4 \mu\Omega\text{cm}$  - Subsection 4.2.3). Problems that need to be overcome include a higher surface roughness, making it harder to realize reproducible results, and the higher deposition temperature of NbTiN, potentially damaging the tunneling barrier.

To reduce the losses at higher frequencies, one may also consider using NbTiN in the microstripline. When the SIS electrodes are made of the lower gap Nb, this is not a good idea. In that case, heated quasiparticles from the Nb electrodes can not scatter into the leads, because there are no available states (the energy gap of the NbTiN is larger), and thus they need to lose energy by electron-phonon scattering, effectively locally increasing the temperature. This will result in a reduction of the gap voltage and a degradation of the mixer performance [9].

However, when the junction electrodes are made of NbTiN, a microstripline with NbTiN may be a good idea. No heating effects are expected to occur, since

there is no difference in gap energy. Still, the high deposition temperature of NbTiN is a problem that needs to be solved, since it will damage the tunneling barrier. Another potential problem is a poor nucleation of NbTiN on SiO<sub>2</sub>, which may reduce the effective gap energy of a NbTiN upper microstrip layer [7, 25].

To overcome heating effects due to trapping of heat in the junction electrodes, a good option is using a normal metal microstripline, such as Al [26, 27]. In this way, heated quasiparticles can diffuse out of the junction, without heating it. Further, although Al has a higher resistivity than Nb below the gap frequency of Nb, it has lower losses above circa 800 GHz, slightly depending on the purity of the Al.

A combination of the low losses of NbTiN and the reduction of heat trapping with Al has been offered by Jackson *et al.*, who combine a Nb/AlO<sub>x</sub>/Nb SIS junction with a NbTiN/SiO<sub>2</sub>/Al microstripline [7], to reach a DSB receiver noise temperature as low as 315 K at 980 GHz, corresponding to  $6.7 hf/k_B$ . A similar approach has been used by Kooi *et al.* [23], who have studied the use of different material combinations for the microstriplines.

## 4.3 Fabrication process

In this Section, we will describe all the processing steps that are necessary to realize the SIS devices studied in this research. Readers with little interest in device fabrication can choose to skip this Section.

### 4.3.1 Substrate preparation

Cylindrical fused quartz substrates with diameter of 2 in (50.8 mm) and a thickness of 250  $\mu\text{m}$  are used in this work. Before the different materials are patterned onto the substrate, it is first cleaned by putting it for 10 minutes in a beaker with hot acetone (at approximately 50 °C, just below the boiling point), which is placed in a standard *ultrasonic bath*. The ultrasonic bath is filled with water in which a standing wave is created by sonic vibrations. The standing wave is transferred via the acetone to the wafer, thus enhancing the cleaning process. An ultrasonic bath is a standard cleaning tool in device processing for microelectronics and nanotechnology.

After this, the wafer is transferred to the main (vacuum) processing chamber of a deposition system and cleaned on a microscopic level by an RF argon (Ar) *plasma clean* for 3 minutes, at a power of about 75 W and a pressure of  $8.4 \times 10^{-3}$  mbar (0.84 Pa). The purpose of this is to remove as much surface pollution from the substrate as possible. In this work, two different deposition systems have been used: initially, a Nordiko 2000 machine, at later stages a system from Kurt Lesker.

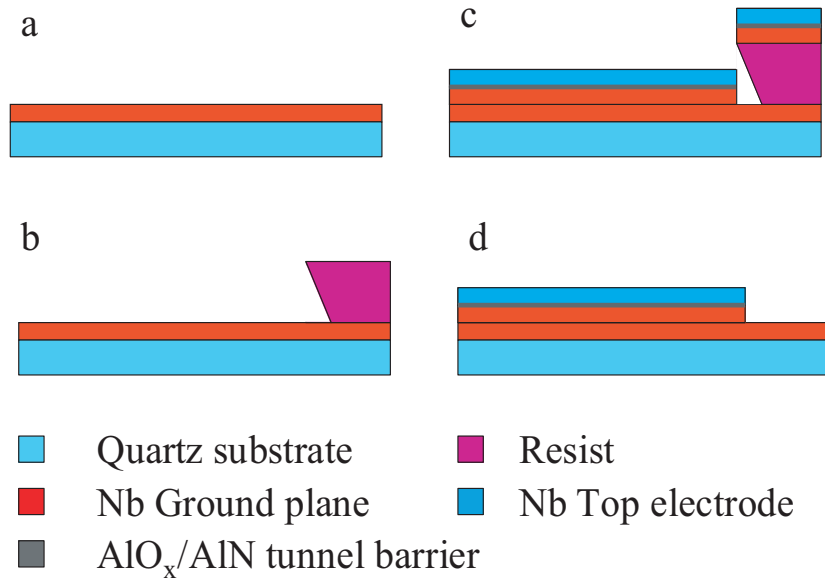


**Figure 4.6:** Schematic diagram of ground plane definition. (a) Deposition of monitor layer. (b) Photo-resist patterning, with undercut. (c) Trilayer deposition. (d) Ground plane lift-off.

Subsequently, a base layer of 100 nm Nb is deposited over the whole substrate by DC *magnetron sputtering*. This layer will serve to monitor the Nb etching at a later stage. Prior to sputtering, the reactor chamber is evacuated to a pressure typically lower than  $1 \times 10^{-7}$  mbar, after which the inert gas Ar is let in until a pressure of  $8.4 \times 10^{-3}$  mbar is reached. Then, a DC power of 630 W is applied, igniting a plasma of Ar<sup>+</sup> ions and electrons, resulting in a DC voltage of a few hundred volts. Due to this voltage, Ar ions are attracted by a Nb target and collide with it, thus releasing Nb atoms. These Nb atoms travel quasi-ballistically through the reactor chamber and stick to the substrate. A magnetic field around the target traps secondary electrons that are emitted from the target and increases the number of ionizing electron - Ar atom collisions. This will also increase the sputtering rate.

The substrate with a monitor layer of 100 nm Nb is shown schematically in panel a of Fig. 4.6.

### 4.3.2 Ground plane definition

After the deposition of the 100 nm Nb monitor layer, the ground plane pattern is defined by *optical lithography*. The substrate is covered with a circa  $2 \mu\text{m}$  thick layer of the photo-resist AZ5214E, selected for its resist wall profile which is well suited for lift-off (e.g., Ref. [28]), by depositing a few ml on it and spinning it for 1 minute at a speed of 5000 rpm. Then, the resist is baked at  $90^\circ\text{C}$  for 2 minutes to

dry out. Pattern definition is done by aligning the substrate under a quartz mask plate with a chromium pattern, which has been designed in-house and defined by e-beam lithography, and exposing them together to deep ultraviolet (DUV) light. The 500 W Hg-Xe lamp produces an intensity at the substrate of  $0.58 \text{ mW/cm}^2$ . Thus, the pattern on the mask plate is transferred to the UV-sensitive photo-resist on the substrate. In the case of the ground plane pattern, the exposure is 24 s. Subsequently, a post exposure bake (PEB) is applied for *image reversal*: the substrate is baked at  $120 \text{ }^\circ\text{C}$  for 20 s, making the previously exposed regions insoluble in developer and no longer light sensitive. The exposure is finished by an (uncritical) 135 s flood exposure, without the mask plate.

The ground plane patterning is completed by immersing the substrate for about 75 s in the developer MF-321 and rinsing it with water. Because of the image reversal, the ground plane pattern consists of a pattern of removed photo-resist. The development time determines the *undercut*: the degree to which the photo-resist is cut away on its edge. Undercut is needed to have smooth edges of the layer that is deposited afterwards. The substrate after photo-resist ground plane patterning is shown in panel b of Fig. 4.6.

We have also occasionally made use of a photolithography system with 350 W Hg lamp, which produced near ultraviolet (NUV) light. In that case, the mask exposure was 1.4 s, the PEB 30 s, the flood exposure 4 s and the development time 80 to 90 s.

The last step of the ground plane definition is the deposition of the *trilayer*: two layers of superconducting material with a tunnel barrier in between. To enhance the heat conduction, a few droplets of vacuum pump oil are put between the chuck of the deposition machine and the substrate.

First, the Nb monitor layer that is not covered with photo-resist, is plasma cleaned to remove the native oxide of Nb, which has emerged after exposure to air. Then, 100 nm Nb is deposited by DC magnetron sputtering, as described above. This is followed by the DC magnetron sputtering of circa 7 nm Al, at pressure of  $8.4 \times 10^{-3}$  mbar and a power of 100 W.

Subsequently, the tunnel barrier (either  $\text{AlO}_x$  or AlN) is grown.  $\text{AlO}_x$  grows ‘naturally’ in an oxygen atmosphere, but for AlN, a plasma is needed. (Chapter 5.)

The trilayer is finished by another layer of 100 nm Nb, deposited by DC magnetron sputtering. We note that the trilayer actually consists of 4 layers: Nb - Al - AlX - Nb, with X either  $\text{O}_x$  or N. Al is a normal metal at the operating temperature of SIS devices in this work, since it becomes superconducting only below its  $T_c$  of 1.2 K [4]. However, because the Al layer is so thin, about 7 nm, which is the same order of magnitude as the coherence length in Nb, the superconducting properties of the Nb extend into the Al. This is called the *proximity effect* [29]. Therefore, we do not really consider the Al as a separate layer, which justifies the term ‘trilayer.’ Nevertheless, the thickness of the Al layer *does* influence the SIS *IV* characteristic: if the Al is too thick, a so-called

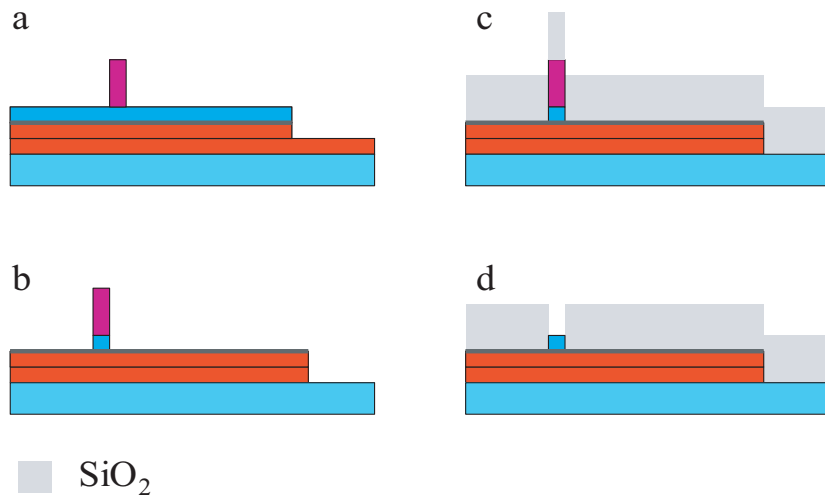


**Figure 4.7:** Schematic diagram of junction definition and SiO<sub>2</sub> deposition. For undefined colors, see Fig. 4.6. (a) E-beam resist pattern for junction. (b) Nb top electrode etch. (c) SiO<sub>2</sub> deposition. (d) SiO<sub>2</sub> self-aligned lift-off.

‘knee’-structure will appear at the gap voltage [30]. The substrate after trilayer deposition is schematically drawn in Fig. 4.6 (c).

The ground plane definition is finalized by performing a *lift-off*. The substrate is immersed in a beaker with hot acetone which is put in an ultrasonic bath. Thus, the photo-resist dissolves in the acetone and the trilayer remains on the substrate only on those places, where there was no resist. Because of the image reversal in the photolithography step, those places are equal to the ground plane pattern.

The substrate after the final processing step of the ground plane definition is shown in panel d of Fig. 4.6.

### 4.3.3 Junction definition

The next step is the definition of the junction top electrode. Since it has already been deposited as the top layer of the trilayer, this will require the removal of part of this top layer. To achieve this, we will have to define a junction pattern in resist.

Junctions are defined by *electron beam lithography*. This allows for a very accurate definition of the junctions, which are square and have areas in the range  $0.25 \mu\text{m}^2$  to  $1.0 \mu\text{m}^2$ . First, we deposit a layer of the negative e-beam resist SAL-601 of about  $1 \mu\text{m}$  by spinning at maximally 1500 rpm. Then the junction pattern is written with an electron beam by a Leica EBPG 5000 system (EBPG stands for electron beam pattern generator). A computer file, which is designed beforehand, specifies the pattern to be written. This file also includes details like the beam current (about 5 nA for small junctions), the beam step size (10 -

25 nm), the spot size on the substrate (about 30 nm in diameter) and the dose (typically  $20 \mu\text{C}/\text{cm}^2$ ). As a result, the junction area is defined very accurately, compared to optical lithography techniques [28]. This is important for a precise determination of the junction impedance and allows for a well designed matching circuit.

After e-beam writing, there is a PEB of 3 minutes at  $110^\circ\text{C}$  to obtain image reversal. Finally, the junction pattern is developed in MF-322 for about 5 to 8 minutes. The substrate with junction pattern is shown in panel a of Fig. 4.7. For junction sizes smaller than  $1 \mu\text{m}^2$ , the resolution of the SAL-601 resist causes the junctions to have somewhat rounded edges, although they have been designed as squares. This can be seen in the Top left panel of Fig. 4.10.

The resulting pattern will have straight edges, which means no undercut. This is necessary for the next step: *reactive ion etching* (RIE) of the top electrode. The substrate is transferred to a vacuum chamber and exposed to a plasma of sulfur hexafluoride ( $\text{SF}_6$ ) and oxygen ( $\text{O}_2$ ) at an RF power of 50 W and pressure of a few  $\mu\text{bar}$  for about 2 minutes. The  $\text{SF}_6$  molecules will become ionized and hit the substrate. There, they react with Nb to form etch products, like  $\text{NbF}_x$  or  $\text{NbSF}_x$  [31]. Part of these etch products is volatile and will be pumped away, others are solid and will stick to the walls of the plasma reactor. Because the substrate is electrically isolated, it becomes charged by absorbed electrons. Due to this charging, a voltage difference of about 200 to 250 V builds up, accelerating the ionized  $\text{SF}_6$  towards the substrate. The ‘delivery’ of the reactive ions is thus mostly vertical, which makes the etching very anisotropic. As a result, the size of the resist pattern is transferred very sharply to the top electrode.

To monitor the etch of the top electrode, a laser beam is pointed on the monitor layer and a combination of the incident and reflected light intensity is measured. During etching, the monitor layer will become thinner, causing a periodic modulation of the measured signal. When the monitor layer has been completely etched, the signal suddenly drops, because the laser is no longer reflected by the Nb, but is partially transmitted into the quartz substrate. Since the monitor layer thickness is equal to the top electrode thickness, this indicates that the top electrode also has been completely etched, and the process can be ended. The result of the junction etching step is drawn schematically in panel b of Fig. 4.7.

To obtain reproducible results, the plasma reactor is cleaned after each use for 2 hours with a pure  $\text{O}_2$  plasma at a pressure of  $50 \mu\text{bar}$  to remove remaining etch products.

#### 4.3.4 Dielectric layer

After the etching of the top electrode, the dielectric  $\text{SiO}_2$  layer will be deposited. However, before this is done, an intermediate step is performed. This intermediate step is either resist recessing or junction anodization. Recent measure-

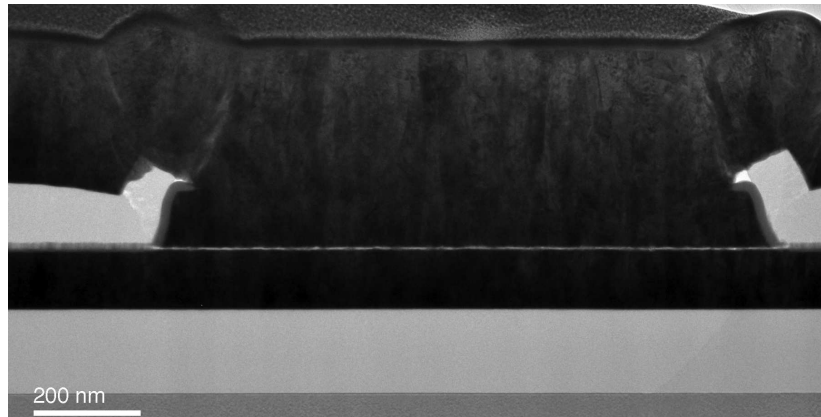


**Figure 4.8:** High resolution transmission electron micrograph of an anodized SIS junction (cross-section). The anodized layer can be recognized as a dark gray area at the sides of the junction. Darkest regions correspond to Nb, thin lighter area is the tunneling barrier [13].

ments have shown (see Chapter 8) that anodization has a degrading effect on the RF performance of an SIS device, and it is therefore not advisable to be used. Nonetheless, we will explain here what anodization is.

During *resist recessing*, the substrate is exposed to an  $O_2$  plasma at a pressure of about 0.2 mbar and a power of circa 30 W. This plasma etches the resist, but it does not etch the Nb. Because of the relatively high pressure, the reactive ions do not build up much extra vertical speed compared to horizontal speed, and hence, the etching is more isotropic than the top electrode etch. As a consequence, the resist pattern is made smaller. This helps to reduce short circuiting of the SIS junction, as will be explained below.

Junction *anodization* is an electrolytic passivation process to increase the thickness of the natural oxide layer on the substrate. This protects the SIS junction and prevents short circuits. During anodization, the edge of the junction top electrode becomes oxidized, as well as the Al layer and part of the ground plane Nb underneath the  $AlO_x$  or AlN. A TEM image of an anodized junction is shown in Fig. 4.8.

When the resist recess or the anodization has been done, the 250 nm  $SiO_2$  layer is deposited with *RF magnetron sputtering* at a pressure of 8 mbar and a power of 75 W. RF magnetron sputtering is similar to DC magnetron sputtering, but now, a RF voltage is applied to the system. The substrate after sputtering of the dielectric layer is shown in Fig. 4.7 (c) and in the top right panel of Fig. 4.10.

The next step is the self-aligned lift-off of the dielectric layer. To dissolve the junction resist pattern, the substrate is immersed in acetone for at least half a day (12 hours). Removing the resist will ‘open’ the junctions and expose them to the

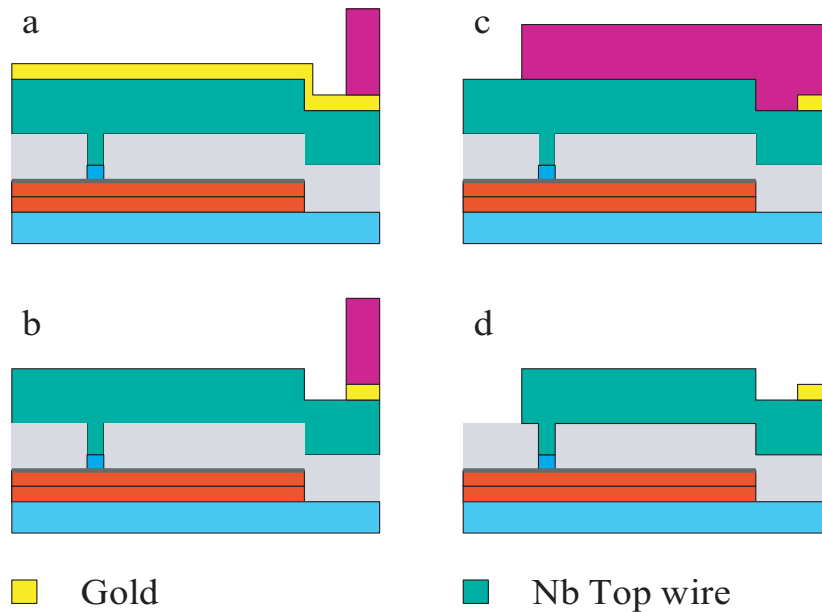


**Figure 4.9:** Schematic diagram of contact pads and top wire definition. For undefined colors, see Figs. 4.6 and 4.7. (a) Deposition of Nb for top wire and Au for contact pads; photo-resist for contact pattern. (b) Wet etch of Au to define contact pads. (c) E-beam resist for top wire pattern. (d) Top wire etch and removal of resist layer finish the SIS device.

environment, while the rest of the structure will remain covered by  $\text{SiO}_2$ . Because the junction holes that have to emerge are very small ( $1 \mu\text{m}^2$  or less), this lift-off process needs some extra treatment. First, after approximately 12 hours of rest, the acetone is heated to  $50 \text{ }^\circ\text{C}$  and the beaker is then put in an ultrasonic bath for 10 minutes (*ultrasonicated*). Then, the substrate is taken out and *brushed* very softly with a tissue, while keeping the surface wet with acetone. Brushing it too hard or too long will result in the removal of too much  $\text{SiO}_2$ , which may cause short circuits later on. After the brushing, the substrate is ultrasonicated for about 10 minutes in Positive Resists Stripper (PRS) 3000. Rinsing in water finishes this lift-off process. The resulting substrate is schematically drawn in Fig. 4.7 (d).

### 4.3.5 Topwire and contact pads

The final stage of the creation of an SIS device is the definition of top wire and contact pads. First, the top of the junction top electrode is cleaned by an Ar RF plasma in a vacuum chamber for 3 minutes. This step is essential to make a good contact to the junction, because it intends to remove the native oxide of the Nb. However, the side effect is that if too much  $\text{SiO}_2$  has been removed during

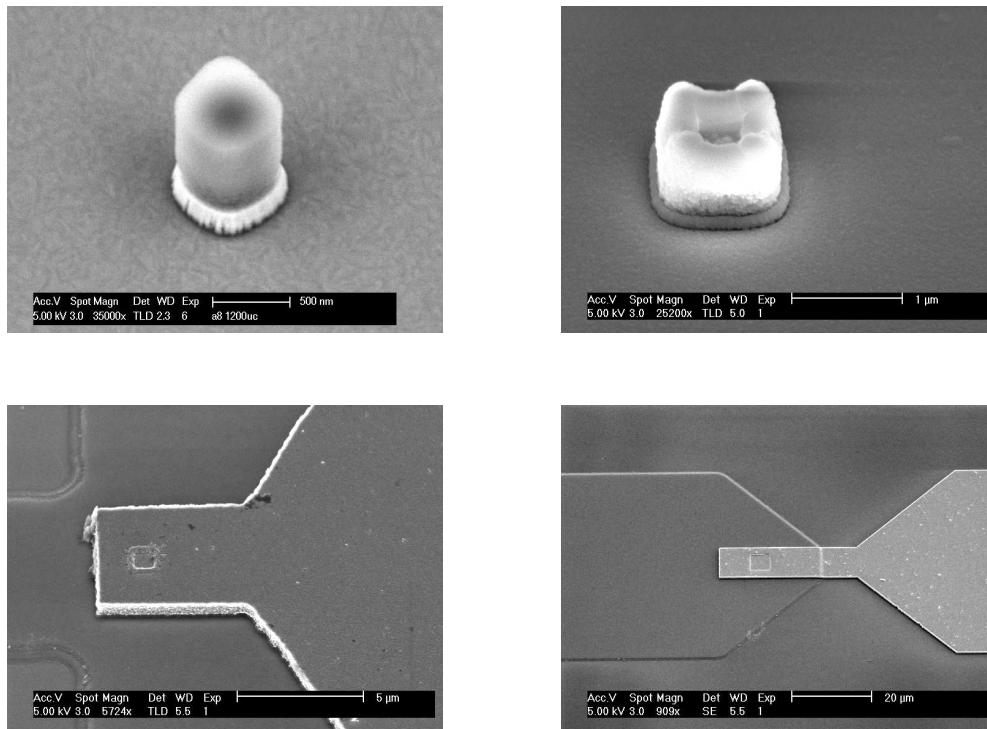


**Figure 4.10:** SEM images during different stages of device realization. (Top left)  $0.36 \mu\text{m}^2$  junction, rotated over  $45^\circ$ , after top electrode etching. The resist can be seen on top of the remaining top electrode. (Top right)  $1 \mu\text{m}^2$  junction, after  $\text{SiO}_2$  deposition. The junction resist has been recessed after top electrode etching, which can be seen by a step in height. (Bottom left)  $1 \mu\text{m}^2$  junction contacted by a top wire, after finishing all the processing steps. (Bottom right)  $25 \mu\text{m}^2$  junction used for DC testing.

its lift-off, the fragile tunnel barrier ( $\text{AlO}_x$  or  $\text{AlN}$ ) is exposed to the Ar plasma clean. As a result, the barrier will be etched away, and there will be an electrical connection parallel to the junction: a short circuit. Therefore, either the resist recess step (preventing the removal of too much  $\text{SiO}_2$ ) or the anodization step (protecting the tunneling barrier by making it much thicker) is necessary.

After RF cleaning, without breaking the vacuum, a layer of 500 nm Nb is deposited with DC magnetron sputtering. Again without taking the substrate out of the vacuum of the system, 50 nm Au is subsequently deposited by DC magnetron sputtering at a pressure of  $8 \times 10^{-3}$  mbar and a power of 110 W.

The next step is the definition of the contact pad pattern with optical lithography. Since the contacts will be etched out of the already deposited Au, no image reversal is needed during the lithography. Using the DUV light source, the AZ5214E resist is now exposed for 90 s and developed in MF-321 for 135 s. No PEB is applied. When using the NUV source, the exposure time was 2.8 s and the development time about 155 s. The substrate after deposition of Nb for

the top wire and Au for the contact pads, and after definition of the contact pad etching mask, is shown in Fig. 4.9 (a).

The Au wet etch is done in a solution of a buffer system of potassium iodide and iodide (KI/I<sub>2</sub>) in water. The substrate is immersed in the etchant for about 40 s, isotropically etching the Au, where it has not been covered with resist. The contact pad etch is drawn schematically in panel b of Fig. 4.9. After this has finished, the resist is removed by ultrasonicing in hot acetone for a few minutes.

Subsequently, the top wire etching mask is defined by e-beam lithography in SAL-601 resist. E-beam lithography is used because of the high alignment accuracy of the system, needed to align the matching circuit formed by the top wire to the 1  $\mu\text{m}^2$  junction. The top wire pattern in e-beam resist is shown in Fig. 4.9 (c).

To complete the SIS device realization, the top wire is etched with a RIE in a SF<sub>6</sub>/O<sub>2</sub> plasma at 50 W. This takes approximately 6 minutes, in steps of 2 minutes with a break of a few minutes in between to prevent heating of the substrate. The etching process is monitored by measuring the reflection off the top wire Nb that is being etched, similar to the monitor layer during top electrode etching.

Finally, the top wire resist pattern is removed by ultrasonicing in hot PRS 3000 for a few minutes. The finished SIS device with all its layers is drawn schematically in Fig. 4.9 (d).

## 4.4 Final remarks

To investigate the results during SIS processing, the substrate can be inspected by optical microscopy or by scanning electron microscopy (SEM). SEM pictures of different stages of the SIS device realization can be found in Fig. 4.10.

The SIS devices that have been made in this work have always been realized in batches: one batch, made on a 2 in wafer, contains eight sectors, and each sector has 88 devices, of which 7 are test devices (so in total, 704 devices of which 56 are test devices). In different sectors, very often variations are made in the design of the microstripline, the IF filter, the antenna, or in the size of the junction. In this way, many different predictions can be tested with one successfully realized batch.

The test devices are solely for DC measurements and hence do not have an antenna, tuning circuit or IF filter. Furthermore, there are test structures in the surroundings of the 8 sectors, as well as between them. Those test structures offer the possibility to measure the material parameters (resistivity, critical temperature) of different layers and monitor the various processing steps (in terms of e.g. undercut and alignment of different layers). The layout of a batch of SIS devices, together with all the test structures, is shown in Fig. 4.11.

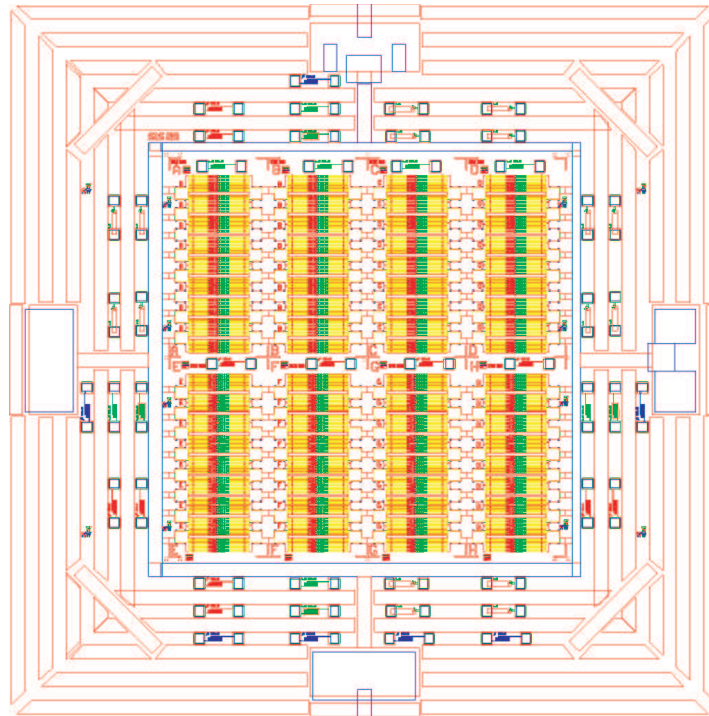


**Figure 4.11:** Final layout of a batch of SIS devices, together with test devices and structures.

## References

- [1] “Dielectric constants of glasses”, in *CRC Handbook of Chemistry and Physics, 88th Edition (Internet Version 2008)*, D. R. Lide, Ed., CRC Press/Taylor and Francis, Boca Raton, FL, USA.
- [2] “Physical constants of clear fused quartz”, in *CRC Handbook of Chemistry and Physics, 88th Edition (Internet Version 2008)*, D. R. Lide, Ed., CRC Press/Taylor and Francis, Boca Raton, FL, USA.
- [3] “Thermal and physical properties of pure metals”, in *CRC Handbook of Chemistry and Physics, 88th Edition (Internet Version 2008)*, D. R. Lide, Ed., CRC Press/Taylor and Francis, Boca Raton, FL, USA.
- [4] L. I. Berger and B. W. Roberts, “Properties of superconductors”, in *CRC Handbook of Chemistry and Physics, 88th Edition (Internet Version 2008)*, D. R. Lide, Ed., CRC Press/Taylor and Francis, Boca Raton, FL, USA.
- [5] D. K. Finnemore, T. F. Stromberg, and C. A. Swenson, “Superconducting properties of high-purity niobium”, *Phys. Rev.*, Vol. **149**, 231 (1966).
- [6] G. de Lange, J. J. Kuipers, T. M. Klapwijk, R. A. Panhuyzen, H. van de Stadt, and M. W. M. de Graauw, “Superconducting resonator circuits at frequencies above the gap frequency”, *J. Appl. Phys.*, Vol. **77**, 1795 (1995).

- 
- [7] B. D. Jackson, A. M. Baryshev, G. de Lange, J. R. Gao, S. V. Shitov, N. N. Iosad, and T. M. Klapwijk, “Low-noise 1 THz superconductor-insulator-superconductor mixer incorporating a NbTiN/SiO<sub>2</sub>/Al tuning circuit”, *Appl. Phys. Lett.*, Vol. **79**, 436 (2001).
- [8] B. D. Jackson, G. de Lange, T. Zijlstra, M. Kroug, J. W. Kooi, J. A. Stern, and T. M. Klapwijk. “Low-noise 0.8-0.96- and 0.96-1.12-THz superconductor-insulator-superconductor mixers for the Herschel Space Observatory”, *IEEE Trans. Microwave Theory and Techn.*, Vol. **54**, 547 (2006).
- [9] B. Leone, B. D. Jackson, J. R. Gao, and T. M. Klapwijk, “Geometric heat trapping in niobium superconductor-insulator-superconductor mixers due to niobium titanium nitride leads”, *Appl. Phys. Lett.*, Vol. **76**, 780 (2000).
- [10] D. C. Mattis, and J. Bardeen, “Theory of the anomalous skin effect in normal and superconducting metals”, *Phys. Rev.*, Vol. **111**, 412 (1958).
- [11] The Jet Propulsion Laboratory, Pasadena, USA, for example in J. W. Kooi, M. Chan, B. Bumble, H. G. LeDuc, P. L. Schaffer, and T. G. Phillips, “180-425 GHz low noise SIS waveguide receivers employing tuned Nb/AlO<sub>x</sub>/Nb tunnel junctions”, *Int. J. Infrared and Millimeter Waves*, Vol. **15**, 783 (1994).
- [12] The Kobe Advanced Research Center, Kobe, Japan, for example in Y. Uzawa, A. Kawakami, S. Miki, and Z. Wang, “Performance of all-NbN quasi-optical SIS mixers for the terahertz band”, *IEEE Trans. Appl. Superconductivity*, Vol. **11**, 183 (2001).
- [13] F. D. Tichelaar at the National Centre for HREM at Delft University of Technology is acknowledged for the investigations performed by transmission electron microscopy and crystallography.
- [14] O. Noroozian, M. Sc. Thesis, Delft University of Technology (2006).
- [15] “Electrical resistivity of pure metals”, in *CRC Handbook of Chemistry and Physics, 88th Edition (Internet Version 2008)*, D. R. Lide, Ed., CRC Press/Taylor and Francis, Boca Raton, FL, USA.
- [16] J. R. Gavaler, J. K. Hulm, M. A. Janocko, and C. K. Jones, “Preparation and superconducting properties of thin films of transition metal interstitial compounds”, *J. Vac. Sci. Technol.*, Vol. **6**, 177 (1969).
- [17] R. Di Leo, A. Nigro, G. Nobile, and R. Vaglio, “Niobium-titanium nitride thin films for superconducting rf accelerator cavities”, *J. Low Temp. Phys.*, Vol. **78**, 41 (1990).
- [18] A. Kawakami, Y. Uzawa, and Z. Wang, “Development of epitaxial NbN/MgO/NbN superconductor-insulator-superconductor mixers for operations over the Nb gap frequency”, *Appl. Phys. Lett.*, Vol. **83**, 3954 (2003).

- [19] P. Dieleman, H. G. Bukkems, T. M. Klapwijk, M. Schicke, and K. H. Gundlach, "Observation of Andreev reflection enhanced shot noise", *Phys. Rev. Lett.*, Vol. **79**, 3486 (1997).
- [20] Calculated using a formula and numbers from: J. K. W. Yang, A. J. Kerman, E. A. Dauler, V. Anant, K. M. Rosfjord, and K. K. Berggren, "Modeling the electrical and thermal response of superconducting nanowire single-photon detectors", *IEEE Trans. Appl. Superconductivity*, Vol. **17**, 581 (2007).
- [21] "Thermal conductivity of metals and semiconductors as a function of temperature", in *CRC Handbook of Chemistry and Physics, 88th Edition (Internet Version 2008)*, D. R. Lide, Ed., CRC Press/Taylor and Francis, Boca Raton, FL, USA.
- [22] J. Li, M. Takeda, Z. Wang, S.-C. Shi, and J. Yang, "Low-noise 0.5 THz all-NbN superconductor-insulator-superconductor mixer for submillimeter wave astronomy", *Appl. Phys. Lett.*, Vol. **92**, 222504 (2008).
- [23] J. W. Kooi, J. A. Stern, G. Chattopadhyay, H. G. LeDuc, B. Bumble, and J. Zmuidzinas, "Low-loss NbTiN films for THz SIS mixer tuning circuits", *Int. J. Infrared Millim. Waves*, Vol. **19**, 373 (1998).
- [24] N. N. Iosad, B. D. Jackson, F. Ferro, J. R. Gao, S. N. Polyakov, P. N. Dmitriev, and T. M. Klapwijk, "Source optimization for magnetron sputter-deposition of NbTiN tuning elements for SIS THz detectors", *Supercond. Sci. Technol.*, Vol. **12**, 736 (1999).
- [25] B. D. Jackson, G. de Lange, W. M. Laauwen, J. R. Gao, N. N. Iosad, and T. M. Klapwijk, "NbTiN/SiO<sub>2</sub>/NbTiN and NbTiN/SiO<sub>2</sub>/Al tuning circuits for 1 THz waveguide SIS mixers", in *Proceedings of the 11th International Symposium on Space THz Technology*, Ed. J. East, 238 (2000).
- [26] P. Dieleman, T. M. Klapwijk, S. Kovtonyuk, and H. van de Stadt, "Direct current heating in superconductor-insulator-superconductor tunnel devices for THz mixing applications", *Appl. Phys. Lett.*, Vol. **69**, 418 (1996).
- [27] M. Bin, M. C. Gaidis, J. Zmuidzinas, T. G. Phillips, and H. G. LeDuc, "Low-noise 1 THz niobium superconducting tunnel junction mixer with a normal metal tuning circuit", *Appl. Phys. Lett.*, Vol. **68**, 1714 (1996).
- [28] M. M. T. M. Dierichs, R. A. Panhuyzen, C. E. Honingh, M. J. de Boer, and T. M. Klapwijk, "Submicron niobium junctions for submillimeter-wave mixers using optical lithography", *Appl. Phys. Lett.*, Vol. **62**, 774 (1993).
- [29] See, for example: T. M. Klapwijk, "Proximity effect from an Andreev perspective", *J. Supercond.*, Vol. **17**, 593 (2004).
- [30] See, for example: V. Y. Belitsky, V. N. Gubankov, V. F. Koshelets, G. A. Ovsyannikov, I. L. Serpuchenko, S. V. Shitov, M. A. Tarasov, and A.

- 
- N. Vystavkin, "Refractory material SIS junction structures", IEEE Trans. Magnetics, Vol. **MAG-23**, 684 (1987).
- [31] D. J. Adelerhof, M. E. Bijlsma, P. B. M. Fransen, T. Weiman, J. Flokstra, and H. Rogalla, "Fabrication of Nb/Al,AlO<sub>x</sub>/Al/Nb Josephson tunnel junctions using reactive ion etching in SF<sub>6</sub>", Physica C, Vol. **209**, 477 (1993).



## Chapter 5

### From aluminum oxide to aluminum nitride tunnel barriers

This Chapter focuses on the tunneling barrier. Tunnel barriers are the most important part of this work, since the tunneling process forms the base under the use of SIS junctions as heterodyne mixers. Up to now, most SIS mixer applications were based on  $\text{AlO}_x$  tunnel barriers. There have been studies of different barrier materials, like MgO and AlN, but they were never created with a reliable process. We introduce a new method to grow AlN tunnel barriers with a high reproducibility and control. In Sec. 5.1, we will explain which properties of tunnel barriers are important in the context of SIS junctions. In Sec. 5.2 it is described how the process to realize  $\text{AlO}_x$  tunnel barriers for SIS mixers has been replaced with the newly developed process for AlN in this research.

## 5.1 Tunnel barriers in SIS junctions

A tunneling barrier is a thin, insulating layer, in an SIS junction sandwiched between two layers of superconducting material, making it literally the ‘I’ in ‘SIS’.

After the prediction of Tucker and Millea [1], Richards *et al.* [2] and Dolan *et al.* [3] were the first to show experimentally that SIS junctions could serve as heterodyne mixers by using quasiparticle tunneling processes. In this Section, we will explain why it is important in this research to have transparent tunnel barriers (Subsection 5.1.1). Furthermore, we will explain the uniqueness of SIS junctions in the analysis of tunnel barriers and motivate the move from  $\text{AlO}_x$  to AlN (Subsection 5.1.2).

### 5.1.1 The importance of transparent tunnel barriers

As argued in Section 3.3, it is important that the SIS mixers have a large bandwidth to meet the requirements of ALMA Band 9. The Bode [4] formula (Eq. 3.2) indicates that this corresponds to the requirement of a low  $RC$  time constant. Using Simmons’ Eq. 3.5 [5] and the parallel plate capacitor Eq. 3.3, we have shown that the  $RC$  time constant is determined only by the barrier properties. These properties are aptly described by  $R_n A$  and  $C_s$ .

$R_n A$  is independent of junction area (Eq. 3.5) and is for an SIS junction inversely proportional to its critical current density  $J_c$ , according to the Ambegaokar-Baratoff [6] relation

$$J_c = \frac{\pi \Delta(T)}{2e R_n A} \tanh \left( \frac{\Delta(T)}{2k_B T} \right). \quad (5.1)$$

$J_c$  is a quantity that characterizes the barrier transparency: the higher  $J_c$ , the higher the transparency. Achieving a wideband response, or a small  $RC$  time, is realized by a low  $R_n A$ , and thus, a high  $J_c$ . Hence, in order to meet the bandwidth requirements, transparent tunnel barriers are needed.

In principle, the tunnel barrier provides us with three knobs to improve the bandwidth performance of SIS mixers:

1. **The barrier thickness  $t_{bar}$ .** Eq. 3.6 shows that  $RC$  decreases exponentially if  $t_{bar}$  is decreased. However, even for achievable thicknesses, this does not provide a possibility for unlimited improvement, since the quality of the tunnel barrier tends to degrade with thickness. This will be further explained in Subsection 5.1.2.
2. **The energy barrier height  $\phi_0$ .** For all realistic values of  $t_{bar}$  and  $\phi_0$  itself, lowering  $\phi_0$  will also lower  $RC$ . The bandwidth can thus be increased if a barrier material is chosen with a lower  $\phi_0$ . That this is not a straightforward choice for SIS junctions will also be explained in Subsection 5.1.2.
3. **The dielectric constant  $\epsilon_r$  of the barrier material.** When the barrier material is chosen, also its  $\epsilon_r$  should be taken into account. A lower  $\epsilon_r$  causes a lower  $RC$  time.

The  $R_n A$  (and thus  $J_c$ ) is determined by the first two points. Because  $RC$  depends strongly on  $t_{bar}$  and  $\phi_0$ , it is crucial to have transparent tunnel barriers to achieve a large bandwidth.

### 5.1.2 The uniformity of tunnel barriers

The unique property of an SIS junction is the fact that it can provide detailed information about the higher order tunneling processes through the barrier. It differs in that respect from normal metal - insulator - normal metal (NIN) junctions.

For bias voltages below  $V_{gap}$ , no current is expected for an SIS junction in the ‘ideal’ case, at  $T = 0$  K. For nonzero temperatures, a small subgap current is present, which can be easily explained by a Fermi-Dirac distribution (at the appropriate temperature) of the quasiparticles in their density of states:  $N_s(E)f(E)$ .

However, in real measurements of SIS junctions, the subgap current is almost always bigger than what can be expected based on the finite temperature distribution. This can be explained by higher order tunneling processes through the barrier, called multiple Andreev reflections (MAR) [7, 8]. With MAR, a particle can tunnel from one electrode to the other for a bias  $V$  between the two electrodes smaller than  $V_{gap}$ . By  $n$  consecutive Andreev reflections (AR) [9], an electron-like particle can either gain energy  $neV$  (if  $n$  is even), enabling it to overcome the superconducting gap  $2\Delta$ , or reflect back as a hole-like particle (if  $n$  is odd), creating a Cooper pair in the other electrode. In general, for voltages

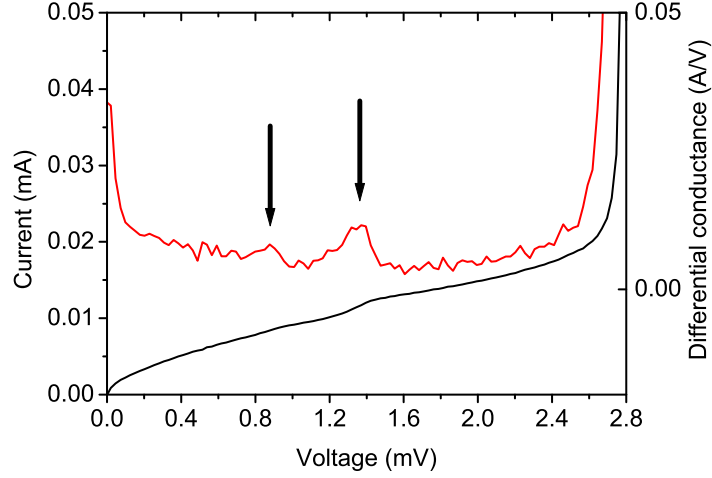


**Figure 5.1:** Example of MAR steps in the current-voltage characteristics of an  $\text{AlO}_x$  SIS junction (full line) and its calculated differential conductance (dotted line). For this junction,  $R_n = 16.4 \Omega$ ,  $R_{sg} = 240 \Omega$  and thus  $Q = 15$ , and  $V_{gap} = 2.78 \text{ mV}$ . The arrows indicate MAR steps.

$V_{gap}/(n+1) < V < V_{gap}/n$ , processes with  $n$  and  $n+1$  AR are possible, transferring a charge of  $(n+1)e$  and  $(n+2)e$ , respectively. This appears in the  $IV$  characteristic of an SIS junction as peaks in the differential conductance  $dI/dV$  at  $V_{MAR,n} = V_{gap}/n$  for all integers  $n \geq 2$ , with a decreasing probability for increasing  $n$ . As a measure for the amount of subgap current, we define the quality factor  $Q$  of a junction as  $Q = R_{sg}/R_n$ , where  $R_{sg}$  is the resistance of the junction for  $V$  between  $V_{gap}/2$  and  $V_{gap}$ . An example of an SIS  $IV$  characteristic with MAR is shown in Fig. 5.1.

If a particle undergoes  $n$  AR, there are  $n+1$  tunneling processes, of electron- and hole-like particles. Therefore, the probability for such a process is  $T^{n+1}$ , with  $T$  the tunneling probability (for one barrier-crossing). As a consequence, an observable amount of MAR can only exist due to pinholes in the tunnel barrier, spots with a locally increased transmissivity, or for thin barriers that have a large overall transparency [8]. SIS junctions with barriers that are sufficiently thick and that have a negligible amount of pinholes, will show no MAR feature. Nevertheless, these barriers can still be very nonuniform, as we will show below.

For thin barriers (meaning, with a high transmissivity), the subgap current, and thus the quality factor  $Q$ , of the SIS junction gives direct information about the lateral uniformity of the barrier. This can be understood as follows: we relate the normal conductance  $G_n$  to a distribution of transparencies  $T_i$ ,

$$G_n \propto \sum_i A_i T_i, \quad (5.2)$$

where  $A_i$  is a fraction of the total area of the tunnel barrier with a uniform transmissivity  $T_i$ , such that  $\sum_i A_i = A$ , the junction area. This distribution of transparencies is not necessarily universal [10], but one based on areas with different transmissivities, resulting from the technological process. This amounts to a situation analogous to superconducting point contacts [11], for which each conduction channel has a different transmission coefficient. For SIS junctions, we write

$$I \propto \sum_i A_i j(V, T_i), \quad (5.3)$$

with  $I$  the total current and  $j$  the voltage-dependent current density per area  $A_i$  given by

$$j(V, T_i) = \sum_m j_m(V, T_i^m). \quad (5.4)$$

Here,  $j_m$  corresponds to the contribution of  $m$ th order tunneling processes, proportional to  $(T_i)^m$ . If we neglect thermal excitations, no first order tunneling processes are possible below  $V_{gap}$ , meaning  $j_1 = 0$ , and the remaining subgap current is due to the higher order terms, which only appear for  $T_i \approx 1$ . Therefore, non-uniformity, causing the emergence of areas with  $T_i \approx 1$ , leads to excessive subgap currents, and thus a low  $Q$ .

For SIS junctions based on amorphous  $\text{AlO}_x$  barriers, the critical current density is limited to about  $20 \text{ kA/cm}^2$ , beyond which large subgap currents emerge [12]. Following the reasoning above, these subgap currents indicate that highly transparent amorphous  $\text{AlO}_x$  barriers are very inhomogeneous. This subject has recently regained attention by the introduction of magnetic tunnel junctions (MTJs), leading to a renewed interest in  $\text{AlO}_x$  barriers. Using different methods, the non-uniformity of amorphous  $\text{AlO}_x$  barriers has been demonstrated by various workers [13, 14, 15].

The local maxima in the transmissivity will dominate the transport properties of a nonuniform barrier. Estimates based on a constant  $\phi$  and  $t_{bar}$  over the barrier are therefore generally lower than anticipated [16, 17, 18]. As a consequence, the use of Simmons' formula (Eq. 3.5) [5] to relate  $R_n$  to a barrier height  $\phi$  and thickness  $t_{bar}$  is inappropriate for non-uniform tunnel barriers, such as amorphous  $\text{AlO}_x$ .

For MTJs, there have been developments to move from using amorphous  $\text{AlO}_x$  to epitaxial magnesium oxide ( $\text{MgO}$ ) with its unique spin-dependent tunneling properties in combination with iron (Fe) electrodes [19, 20]. In the case of Ref. [20], a  $\phi$  (lower than in other literature) is obtained by fitting transmission electron microscopy (TEM) data on  $t_{bar}$  directly with Simmons' formula. In quantum computation, the amorphous tunnel barrier is recognized as an important source of decoherence, leading to the introduction of an epitaxial  $\text{Al}_2\text{O}_3$  barrier [21].

In this research, we study SIS junctions for which we have replaced the commonly used  $\text{AlO}_x$  barriers with epitaxial AlN tunnel barriers. AlN barriers are more uniform than amorphous  $\text{AlO}_x$  barriers, which is demonstrated by their lower subgap currents for similar  $R_n A$  values. With TEM images, the better uniformity of AlN is related to the epitaxial nature of the tunnel barrier (Chapter 7). The lower  $R_n A$  (higher  $J_c$ ) tunnel barriers allow for the design of wider bandwidth SIS mixers (Chapter 8). In the remainder of this Chapter, we will focus on the realization of  $\text{AlO}_x$  tunnel barriers, on the results obtained with AlN in previous work, and on the AlN process we have used, along with typical results.

## 5.2 Realization of tunnel barriers for SIS mixers

Since Josephson's predictions [22] in 1962 of AC and DC supercurrents through junctions with superconducting electrodes (see Chapter 2), lots of types of SIS junctions have been developed, using various superconductors and barrier materials. Many applications were found for Josephson junctions, like SQUIDs (superconducting quantum interference devices), mixers, and in digital logic circuits. Initially, the Josephson effect was used in heterodyne mixing applications [23], but this route proved to be suffering from uncontrollable noise. Quasiparticle mixing [2, 3] on the other hand has turned out to be very successful.

By the beginning of the 1980s, two types of SIS junctions were among the most used: Nb/oxide/Nb and Nb/oxide/Pb (or Pb alloy), because of their good cycling and storage stability and the high  $T_c$  of the superconductors (9.25 K for Nb, and 7.20 K for Pb [24]). Although all-Nb junctions were preferred and various techniques were explored, the niobium oxide was unstable, due to the high reactivity of Nb, resulting in junctions with a low  $Q$  and a lower  $V_{gap}$  than expected [25]. Besides the desired insulator  $\text{Nb}_2\text{O}_5$ , various suboxides ( $\text{NbO}_y$  with varying  $y$ ) are formed in the barrier region, due to the instability of the niobium oxide. Some of these are superconductors with a  $T_c$  lower than Nb, others are highly resistive [26]. The proximity effect [27] makes the entire package superconducting, but  $Q$  and  $V_{gap}$  suffer from its inhomogeneous nature.

A series of papers by Rowell, Gurvitch and coworkers [28, 29, 30] introduced a process in which they sputtered a thin layer of Al onto a base of Nb, which they subsequently oxidized and covered with another layer of Nb, to reliably make all-Nb SIS junctions. This method soon became a standard for a majority of the research on SIS mixers, which it has remained for over 20 years. The details of their work will be discussed in Subsection 5.2.1.

Since 1992, AlN tunnel barriers have been introduced by Shiota *et al.* [31] and investigated by various groups. The main developments are summarized in Subsection 5.2.2.

Finally, in Subsection 5.2.3, we discuss the new method for AlN growth that has been developed in this research. Hopefully, this new method sets a standard

for AlN tunnel barriers, similar to the way the work of Gurvitch *et al.* did for  $\text{AlO}_x$ .

### 5.2.1 $\text{AlO}_x$ tunnel barriers

The main discovery of Gurvitch *et al.* [28, 29, 30] that lead to the standard  $\text{AlO}_x$  tunnel barrier process for all-Nb junctions, was the following: already a very thin (a few nm) layer of Al ‘wets’ the surface of Nb, if it is sputtered directly after it. This means the Nb surface gets completely covered, and its oxidation properties are strongly modified. In this way, the chemically stable Al replaces the unclearly defined package of niobium suboxides. Instead, the layer of Al now takes on the superconducting properties of the underlying Nb due to the superconducting proximity effect [27]. Therefore, tunneling will take place from the proximitized Al to the top Nb (and *vice versa*), and the structure acts as an SIS junction.

We have realized Nb/Al/ $\text{AlO}_x$ /Nb junctions according to Gurvitch’ technique: first, a 100 nm base layer of Nb (DC magnetron sputtered) is covered by DC magnetron sputtering about 7 nm of Al. Then, the sample is transferred to an oxidation chamber, where it is exposed to pure oxygen gas at a pressure of about  $5 \times 10^{-3}$  mbar for 15 to 20 minutes. During this time, the Al oxidizes naturally, growing a layer of  $\text{AlO}_x$ . After the oxidation, a top electrode of 100 nm Nb is sputtered.

For this type of  $\text{AlO}_x$  barrier growth, it has been found [32] that  $J_c$  resulting from the process depends on the oxygen exposure  $E_{O_2}$ , defined as  $E_{O_2} = t_{ox} \times p_{O_2}$ , where  $t_{ox}$  is the oxidation time and  $p_{O_2}$  is the oxygen partial pressure, rather than on  $t_{ox}$  and  $p_{O_2}$  independently. This has been explained by relating the oxide growth to the number of collisions of  $\text{O}_2$  molecules with the oxidizing surface, which is proportional to  $E_{O_2}$ .

### 5.2.2 Previous work on AlN tunnel barriers

In 1992, **Shiota *et al.*** at the Fujitsu Laboratories in Japan were the first to make AlN tunnel barriers [31]. They made Nb/Al-AlN/Nb junctions similarly to Gurvitch’ [30] method, but instead of oxidation in an  $\text{O}_2$  environment, plasma nitridation was used. A plasma was employed, because chemically active nitrogen radicals are needed to create a reaction between Al and N. In the same chamber as the Nb/Al base layer had been deposited,  $\text{N}_2$  was introduced at a pressure of  $2.7 \times 10^{-2}$  mbar. Then, an RF plasma was generated in the reactor for a fixed time, while maintaining the pressure constant. The plasma induced DC bias voltage was -100 V. A schematic drawing of their set-up is shown in Fig. 5.2.

With 10  $\mu\text{m}$  diameter junctions ( $A_j = 79 \mu\text{m}^2$ ), Shiota found a systematic behavior of  $J_c$  as a function of nitridation time  $t_N$ , realizing  $J_c$  in the range 0.7 to 7.0  $\text{kA}/\text{cm}^2$  for  $t_N$  from 80 to 10 s. Their junctions had  $I_c R_{sg} \approx \frac{\pi}{4} V_{gap} Q$  of 20

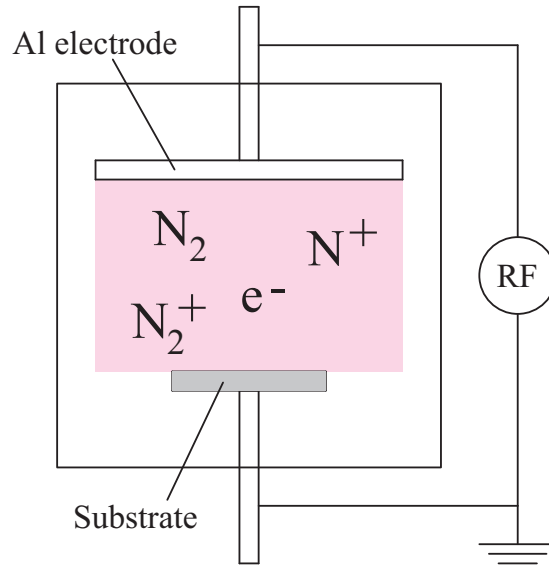


**Figure 5.2:** Schematic image of the conventional AlN growth technique, introduced by Shiota *et al.* [31]. The barrier is grown by nitridation of a thin layer of Al in a nitrogen plasma, created by an RF electric field over parallel plate electrodes in the reactor chamber.

to 40 mV, which corresponds to a  $Q$  from 10 to 20. Further, it was found that their AlN barrier junctions exhibited a better thermal annealing stability than  $\text{AlO}_x$  barrier junctions for temperatures up to 250 °C.

**Wang *et al.*** at the Kansai Advanced Research Center in Japan [33] studied SIS junctions with AlN tunnel barriers and NbN electrodes. In contrast with Shiota *et al.*, they did not use plasma nitridation of a thin Al layer. Instead, the NbN/AlN/NbN trilayer was reactively sputtered from a Nb and an Al target in a  $\text{N}_2$  environment. The AlN layer was grown by sputtering Al in  $\text{N}_2$  at a pressure of  $2.7 \times 10^{-3}$  mbar with an RF power intensity of  $4.6 \text{ W/cm}^2$ . For  $25 \mu\text{m}^2$  junctions, a  $J_c$  of  $8 \text{ kA/cm}^2$  was realized, with  $Q \approx 9$ . Wang *et al.* later further developed their process [34] to obtain a  $Q$  of 4.5 for  $54 \text{ kA/cm}^2$ .

**Dolata *et al.*** at the University of Karlsruhe in Germany [35] used an RF  $\text{N}_2$  plasma at a pressure of  $2.7 \times 10^{-2}$  mbar to reproduce the results of Shiota *et al.*. Varying  $t_N$  from 5 to 60 s,  $J_c$  between 20 and  $0.022 \text{ kA/cm}^2$  was reached, a slightly different dependence than what Shiota *et al.* found. Dolata *et al.* realized large area junctions ( $462 \mu\text{m}^2$ ) and investigated the optical reflectivity change of the Al surface during nitridation and oxidation. They found that nitridation results in a more constant barrier growth, especially in the beginning of the process, and a better definable growth time ( $t_N$ ).

**Kleinsasser *et al.*** at the IBM Corporation in the USA [36] explored Nb/AlN/Nb junctions with higher  $J_c$  values. They also used an RF  $\text{N}_2$  plasma between parallel plates in the main chamber of their deposition system to grow an

AlN tunnel barrier. Taking into account the difference in RF power density, they found almost the same dependence of  $J_c$  on  $t_N$  as Shiota *et al.*. They realized  $1 \mu\text{m}^2$  junctions with  $J_c$  up to  $400 \text{ kA/cm}^2$ , while their AlN junctions had a better  $Q$  than  $\text{AlO}_x$  junctions for  $J_c > 10 \text{ kA/cm}^2$ .

**Kawamura *et al.*** at the California Institute of Technology in the USA [37] and **Bumble *et al.*** at the Jet Propulsion Laboratory in the USA [38] used a method similar to Kleinsasser's [36], but made Nb/AlN/NbTiN SIS junctions. Further, they connected the RF electrode not to the chuck on which the substrate was placed, but to a different place in the reactor. The chuck was grounded. In this way, the density and energy of bombarding ions damaging the tunnel barrier was substantially reduced. They found that high  $J_c$  junctions should be made at room temperature in order to obtain working devices. However, for lower  $J_c$  junctions, annealing in vacuum improved  $Q$ , but made  $J_c$  even lower. SIS junctions with  $R_n A \approx 1 \Omega\mu\text{m}^2$  ( $J_c = 275 \text{ kA/cm}^2$  for the devices, that had  $V_{gap} = 3.5 \text{ mV}$ ) and a quality factor of 5 were realized, although a lot of scatter was observed in  $Q$  for lower values of  $J_c$  [38].

**Iosad *et al.*** in our laboratories [39] minimized the energy and intensity of the ion flux towards the Al surface during nitridation, following Bumble *et al.* [38]. They characterized the AlN barrier formation and correlated the  $\text{N}_2$  plasma characteristics with the properties of the realized SIS junctions. They found that in their case, AlN growth is the result of both Al nitridation and AlN deposition. The nitridation process is a combination of N ion implantation and subsequent diffusion, facilitated by plasma heating.  $10 \mu\text{m}^2$  junctions with  $R_n A = 0.8 \Omega\mu\text{m}^2$  ( $J_c = 175 \text{ kA/cm}^2$  in their case) and a quality of about 4 were realized.

**Kaul *et al.*** at the Jet Propulsion Laboratory [40] used low-energy ion beams from a Kaufman [41] ion source to form AlN tunnel barriers in Nb/AlN/Nb SIS junctions. The AlN barrier was grown by exposing a thin (7 - 9 nm) layer of Al to a beam of N ions from the source. They found a better run-to-run reproducibility compared to methods with RF plasma nitridation and deposition of the barrier by reactively sputtering.  $2.56 \mu\text{m}^2$  SIS junctions with  $J_c = 9.4 \text{ kA/cm}^2$  and  $Q = 13$  were realized.

**Endo *et al.*** at the National Astronomical Observatory of Japan [42] recently used a parallel plate RF plasma in a load-locked chamber for the nitridation of a thin Al layer. In contrast with previous work, they used a two-step ignition and a composite plasma of  $\text{N}_2$  and Ar, and later also He [43], to improve their process reproducibility. However, the realized quality factors were rather low:  $Q = 5$  for  $R_n A = 12 \Omega\mu\text{m}^2$  ( $J_c = 18 \text{ kA/cm}^2$ ).

### 5.2.3 AlN tunnel barriers in this work

The quality of AlN tunnel barriers depends strongly on the damage that is being done by highly energetic ions colliding with the substrate, as previous workers have indicated [38, 39, 40]. We have developed a new method (Zijlstra *et al.*

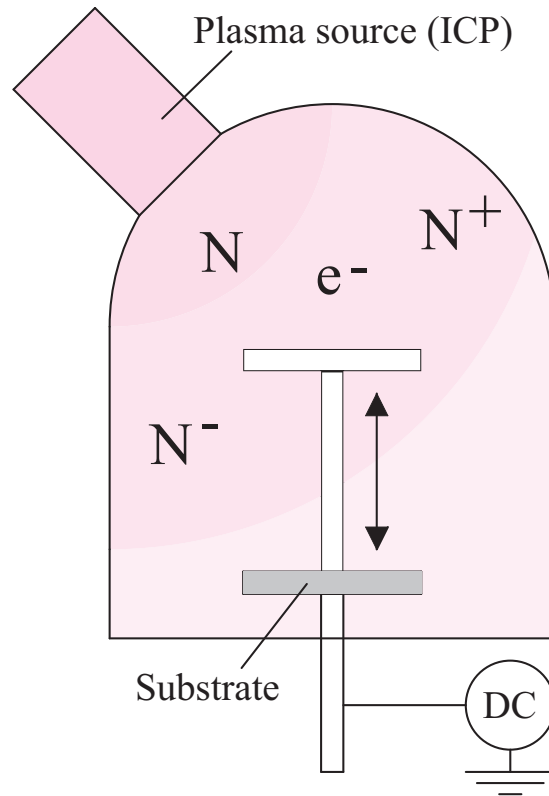


**Figure 5.3:** Schematic image of the nitridation chamber, used in this work. The distance from the substrate to the ICP source can be varied. Optionally, a DC bias voltage can be applied to the chuck.

[44]), using the afterglow region of a nitrogen plasma from an inductively coupled plasma (ICP) source, also called COPRA (controlled plasma reactor), from CCR Technology [45]. This method has been independently studied by Cecil *et al.* [46], but so far without reported SIS devices.

After deposition of a 100 nm layer of Nb and a thin layer of Al ( $\sim 7$  nm), the sample is transferred to a separate nitridation chamber. The 160 mm ICP source is mounted on this chamber, into which the plasma diffuses. The source is supplied with an RF power of about 550 W. To minimize the damage to the AlN barrier, we choose to work in a range of relatively high pressures, typically  $3 \times 10^{-2}$  mbar, reducing the ion energies to a few eV. Further, at these higher pressures we expect a larger fraction of atomic N [45].

In Fig. 5.3, a schematic drawing of the nitridation chamber is shown. The chuck, on which the substrate is mounted, can be DC biased, although no voltage has been applied in this work. Further, its height in the chamber can be varied, thus changing the distance to the ICP source. We have used chuck-source distances between 15 and 30 cm.

Typical results that have been obtained are shown in Fig. 5.4. In this Figure,

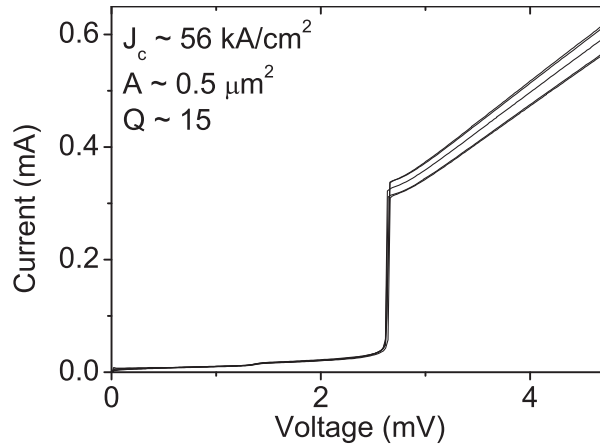


**Figure 5.4:** Typical current-voltage characteristics of Nb/AlN/Nb SIS junctions realized in this work. The  $R_n A$  of these devices, determined by measuring ‘big’  $2.0 \mu\text{m}^2$  junctions, is  $3.7 \Omega\mu\text{m}^2$  (which yields  $J_c \approx 56 \text{ kA/cm}^2$ ). Based on  $R_n \approx 7 \Omega$ , the junction area for these junctions is about  $0.5 \mu\text{m}^2$ .  $Q$  is about 15.

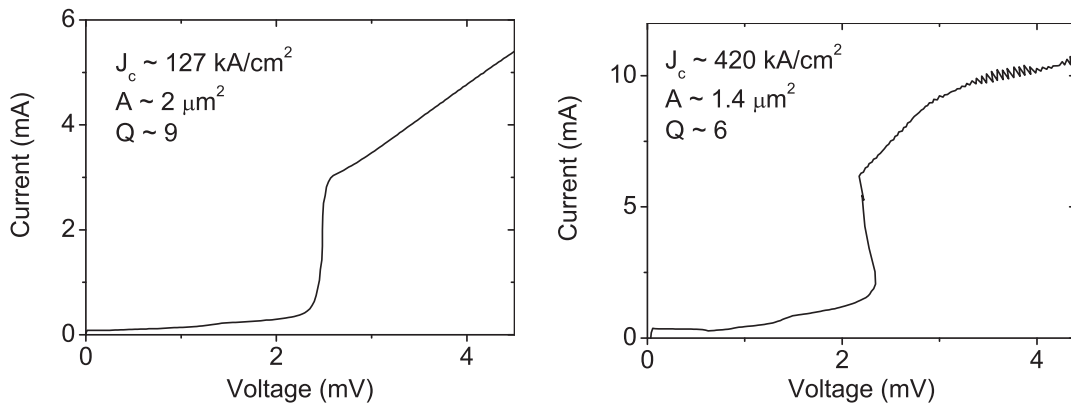


**Figure 5.5:** Current-voltage characteristics of high  $J_c$  SIS junctions with AlN tunnel barriers. (Left) Device with area  $2 \mu\text{m}^2$ , which has  $J_c \approx 130 \text{ kA/cm}^2$  and  $Q \approx 9$ . (Right) Device with area  $1.4 \mu\text{m}^2$  and  $J_c \approx 420 \text{ kA/cm}^2$  still has  $Q \approx 6$ .

$IV$  characteristics are plotted for devices with  $J_c = 56 \text{ kA/cm}^2$  ( $R_n A = 3.7 \Omega\mu\text{m}^2$ ) and  $Q$  larger than 15, realized with  $t_N = 15 \text{ min}$ . By using shorter nitridation times  $t_N$  or increasing the distance from chuck to source, good quality SIS junctions can be realized with very high critical current densities up to several 100s of  $\text{kA/cm}^2$ , as shown in Fig. 5.5.

A detailed analysis of the DC test results of SIS junctions with tunnel barriers realized with our new AlN growth method, along with a TEM analysis of the barriers, can be found in Chapter 7.

## References

- [1] J. R. Tucker and M. F. Millea, “Photon detection in nonlinear tunneling devices”, *Appl. Phys. Lett.*, Vol. **33**, 611 (1978).
- [2] P. L. Richards, T. M. Shen, R. E. Harris, and F. L. Lloyd, “Quasiparticle heterodyne mixing in SIS tunnel junctions”, *Appl. Phys. Lett.*, Vol. **34**, 345 (1979).
- [3] G. J. Dolan, T. G. Phillips, and D. P. Woody, “Low-noise 115-GHz mixing in superconducting oxide-barrier tunnel junctions”, *Appl. Phys. Lett.*, Vol. **34**, 347 (1979).
- [4] H. W. Bode, *Network analysis and feedback amplifier design*, Van Nostrand, New York, USA (1945).
- [5] J. G. Simmons, “Generalized formula for the electric tunnel effect between similar electrodes separated by a thin insulating film”, *J. Appl. Phys.*, **34**, 1793 (1963).
- [6] V. Ambegaokar, and A. Baratoff, “Tunneling between superconductors”, *Phys. Rev. Lett.*, Vol. **10**, 486 (1963); erratum, Vol. **11**, 104 (1963).
- [7] T. M. Klapwijk, G. E. Blonder, and M. Tinkham, “Explanation of subharmonic energy gap structure in superconducting contacts”, *Physica B+C*, Vol. **109-110**, 1657 (1982).
- [8] A. W. Kleinsasser, R. E. Miller, W. H. Mallison, and G. B. Arnold, “Observation of multiple Andreev reflections in superconducting tunnel junctions”, *Phys. Rev. Lett.*, Vol. **72**, 1783 (1994).
- [9] A. F. Andreev, “Thermal conductivity of the intermediate state of superconductors”, *Zh. Eksp. Teor. Fiz.*, Vol. **46**, 1823 (1964).
- [10] K. M. Schep and G. E. W. Bauer, “Universality of transport through dirty interfaces”, *Phys. Rev. Lett.*, Vol. **78**, 3015 (1997).
- [11] E. Scheer, P. Joyez, D. Esteve, C. Urbina, and M. H. Devoret, “Conduction channel transmissions of atomic-size aluminum contacts”, *Phys. Rev. Lett.*, Vol. **78**, 3535 (1997).
- [12] R. E. Miller, W. H. Mallison, A. W. Kleinsasser, K. A. Delin, and E. M. Macedo, “Niobium trilayer Josephson tunnel junctions with ultrahigh critical current densities”, *Appl. Phys. Lett.*, Vol. **63**, 1423 (1993).
- [13] N. Rando, P. Videler, A. Peacock, A. van Dordrecht, and P. Verhoeve, “Transmission electron microscopy and atomic force microscopy analysis of Nb-Al-AlO<sub>x</sub>-Nb superconducting tunnel junction detectors”, *J. Appl. Phys.*, Vol. **77**, 4099 (1995).
- [14] W. H. Rippard, A. C. Perrella, F. J. Albert, and R. A. Buhrman, “Ultrathin aluminum oxide tunnel barriers”, *Phys. Rev. Lett.*, Vol. **88**, 046805 (2002).

- [15] K. M. Lang, D. A. Hite, R. W. Simmonds, R. McDermott, D. P. Pappas, and J. M. Martinis, "Conducting atomic force microscopy for nanoscale tunnel barrier characterization", *Rev. Sci. Instrum.*, Vol. **75**, 2726 (2004).
- [16] For example, T. Imamura and S. Hasuo, "Cross-sectional transmission electron microscopy observation of Nb/AlO<sub>x</sub>-Al/Nb Josephson junctions", *Appl. Phys. Lett.*, Vol. **58**, 645 (1991).
- [17] S. K. Tolpygo, E. Cimpoiasu, X. Liu, N. Simonian, Y. A. Polyakov, J. E. Lukens, and K. K. Likharev, "Tunneling properties of barriers in Nb/Al/AlO<sub>x</sub>/Nb junctions", *IEEE Trans. Appl. Supercond.*, Vol. **13**, 99 (2003).
- [18] Z. Wang, H. Terai, A. Kawakami, and Y. Uzawa, "Interface and tunneling barrier heights of NbN/AlN/NbN tunnel junctions", *Appl. Phys. Lett.*, Vol. **75**, 701 (1999).
- [19] S. S. P. Parkin, C. Kaiser, A. Panchula, P. M. Rice, B. Hughes, M. Samant, and S.-H. Yang, "Giant tunnelling magnetoresistance a room temperature with MgO (100) tunnel barriers", *Nat. Mater.*, Vol. **3**, 862 (2004).
- [20] S. Yuasa, T. Nagahama, A. Fukushima, Y. Suzuki, and K. Ando, "Giant room-temperature magnetoresistance in single-crystal Fe/MgO/Fe magnetic tunnel junctions", *Nat. Mater.*, Vol. **3**, 868 (2004).
- [21] S. Oh, K. Cicak, J. S. Kline, M. A. Sillanpää, K. D. Osborn, J. D. Whittaker, R. W. Simmonds, and D. P. Pappas, "Elimination of two level fluctuators in superconducting quantum bits by an epitaxial tunnel barrier", *Phys. Rev. B*, Vol. **74**, 100502 (2006).
- [22] B. D. Josephson, "Possible new effects in superconductive tunnelling", *Phys. Lett.*, Vol. **1**, 251 (1962).
- [23] Y. Taur, J. H. Claassen, and P. L. Richards, "Josephson junctions as heterodyne detectors", *IEEE Trans. Microwave Theory and Techn.*, Vol. **22**, 1005 (1974).
- [24] L. I. Berger and B. W. Roberts, "Properties of superconductors", in *CRC Handbook of Chemistry and Physics, 88th Edition (Internet Version 2008)*, D. R. Lide, Ed., CRC Press/Taylor and Francis, Boca Raton, FL, USA.
- [25] G. B. Arnold, J. Zasadzinski, and E. L. Wolf, "A resolution of the controversy on tunneling in Nb," *Phys. Lett. A*, vol. 69, 136 (1978).
- [26] J. K. Hulm, C. K. Jones, R. A. Hein, and J. W. Gibson, "Superconductivity in the TiO and NbO systems," *J. Low Temp. Phys.*, vol. 7, 291 (1972).
- [27] T. M. Klapwijk, "Proximity effect from an Andreev perspective", *J. Supercond.*, Vol. **17**, 593 (2004).
- [28] J. M. Rowell, M. Gurvitch, and J. Geerk, "Modification of tunneling barriers on Nb by a few monolayers of Al", *Phys. Rev. B*, Vol. **24**, 2278 (1981).

- [29] M. Gurvitch, J. M. Rowell, H. A. Huggins, M. A. Washington, and T. A. Fulton, “Nb Josephson tunnel junctions with thin layers of Al near the barrier”, 1981 International Electron Devices Meeting, Vol. **27**, 115 (1981).
- [30] M. Gurvitch, M. A. Washington, and H. A. Huggins, “High quality refractory Josephson tunnel junctions utilizing thin aluminum layers”, Appl. Phys. Lett., Vol. **42**, 472 (1983).
- [31] T. Shiota, T. Imamura, and S. Hasuo, “Nb Josephson junction with an  $\text{AlN}_x$  barrier made by plasma nitridation”, Appl. Phys. Lett., Vol. **61**, 1228 (1992).
- [32] A. W. Kleinsasser, R. E. Miller, and W. H. Mallison, “Dependence of critical current density on oxygen exposure in Nb- $\text{AlO}_x$ -Nb tunnel junctions”, IEEE Trans. Appl. Superconductivity, Vol. **5**, 26 (1995).
- [33] Z. Wang, A. Kawakami, Y. Uzawa, and B. Komiyama, “High critical current density NbN/AlN/NbN tunnel junctions fabricated on ambient temperature MgO substrates”, Appl. Phys. Lett., Vol. **64**, 2034 (1994).
- [34] Z. Wang, A. Kawakami, and Y. Uzawa, “NbN/AlN/NbN tunnel junctions with high current density up to  $54 \text{ kA/cm}^2$ ”, Appl. Phys. Lett., Vol. **70**, 114 (1997).
- [35] R. Dolata, M. Neuhaus, and W. Jutzi, “Tunnel barrier growth dynamics of Nb/AlN<sub>x</sub>-Al/Nb Josephson junctions”, Physica C, Vol. **241**, 25 (1995).
- [36] A. W. Kleinsasser, W. H. Mallison, and R. E. Miller, “Nb/AlN/Nb Josephson junctions with high critical current density”, IEEE Trans. Appl. Superconductivity, Vol. **5**, 2318 (1995).
- [37] J. Kawamura, J. Chen, D. Miller, J. Kooi, J. Zmuidzinas, B. Bumble, H. G. LeDuc, and J. A. Stern, “Low-noise submillimeter-wave NbTiN superconducting tunnel junction mixers”, Appl. Phys. Lett., Vol. **75**, 4013 (1999).
- [38] B. Bumble, H. G. LeDuc, J. A. Stern, and K. G. Megerian, “Fabrication of Nb/Al-N<sub>x</sub>/NbTiN junctions for SIS mixer applications”, IEEE Trans. Appl. Superconductivity, Vol. **11**, 76 (2001).
- [39] N. N. Iosad, A. B. Ermakov, F. E. Meijer, B. D. Jackson, and T. M. Klapwijk, “Characterization of the fabrication process of Nb/Al-AlN<sub>x</sub>/Nb tunnel junctions with low  $R_n A$  values up to  $1 \text{ } \Omega \mu\text{m}^2$ ”, Supercond. Sci. Technol., Vol. **15**, 945 (2002).
- [40] A. B. Kaul, A. W. Kleinsasser, B. Bumble, H. G. LeDuc, and K. A. Lee, “Aluminum nitride tunnel barrier formation with low-energy ion beams”, J. Mater. Res., Vol. **20**, 3047 (2005).
- [41] H. R. Kaufman, W. E. Hughes, R. S. Robinson, and G. R. Thompson, “Thirt-eight-centimeter ion source”, Nucl. Instr. Meth. in Phys. Res. B, Vol. **37/38**, 98 (1989).

- 
- [42] A. Endo, T. Noguchi, T. Matsunaga, and T. Tamura, “Development of Nb/Al-AlN<sub>x</sub>/Nb SIS tunnel junctions for submillimeter-wave mixers”, IEEE Trans. Appl. Superconductivity, Vol. **17**, 367 (2007).
- [43] A. Endo, H. Inoue, S. Asayama, T. Noguchi, M. Kroug, and T. Tamura, “Fabrication of aluminum nitride barrier SIS mixer devices using nitrogen plasma diluted by noble gases”, J. Phys: Conf. Ser., Vol. **97**, 012251 (2008).
- [44] T. Zijlstra, C. F. J. Lodewijk, N. Vercruyssen, F. D. Tichelaar, D. N. Loudkov, and T. M. Klapwijk, “Epitaxial aluminum nitride tunnel barriers grown by nitridation with a plasma source”, Appl. Phys. Lett., Vol. **91**, 233102 (2007). *Note: this reference corresponds to Chapter 7.*
- [45] M. Weiler, K. Lang, E. Li, and J. Robertson, “Deposition of tetrahedral hydrogenated amorphous carbon using a novel electron cyclotron wave resonance reactor”, Appl. Phys. Lett., Vol. **72**, 1314 (1998).
- [46] T. W. Cecil, R. M. Weikle, A. R. Kerr, and A. W. Lichtenberger, “Investigation of NbTiN thin films and AlN tunnel barriers with ellipsometry for superconducting device applications”, IEEE Trans. Appl. Superconductivity, Vol. **17**, 3525 (2007).



## Chapter 6

# Optimizing superconducting matching circuits for Nb SIS mixers operating around the gap frequency

The bandwidth and noise temperature of superconducting - insulating - superconducting (SIS) mixers are strongly determined by the matching between antenna and tunnel-junction. Optimal scientific benefit from Band 9 (600 to 720 GHz) of the Atacama Large Millimeter Array requires a proper design of the matching circuit by taking into account the energy gap of the niobium (680 GHz). In preliminary experiments we have found that tapered structures lead to significant improvements, which suggests that a systematic analysis of optimized geometrical shapes might be beneficial. The tuning circuits are analyzed using a model, which includes the Mattis-Bardeen theory for the surface impedance of Nb and which allows arbitrary shapes. We will present simulations and experimental results focusing on the transmission efficiency, which can conveniently be evaluated experimentally by using a Fourier Transform Spectrometer. We will show how the shape influences the transmission efficiency and relate it to observed noise temperatures of the mixers.

---

Most of this Chapter has been published as: C. F. J. Lodewijk, O. Noroozian, D. N. Loudkov, T. Zijlstra, A. M. Baryshev, F. P. Mena, and T. M. Klapwijk, "Optimizing superconducting matching circuits for Nb SIS mixers operating around the gap frequency", *IEEE Trans. Appl. Superconductivity*, Vol. **17**, No. 2, 375 (2007).

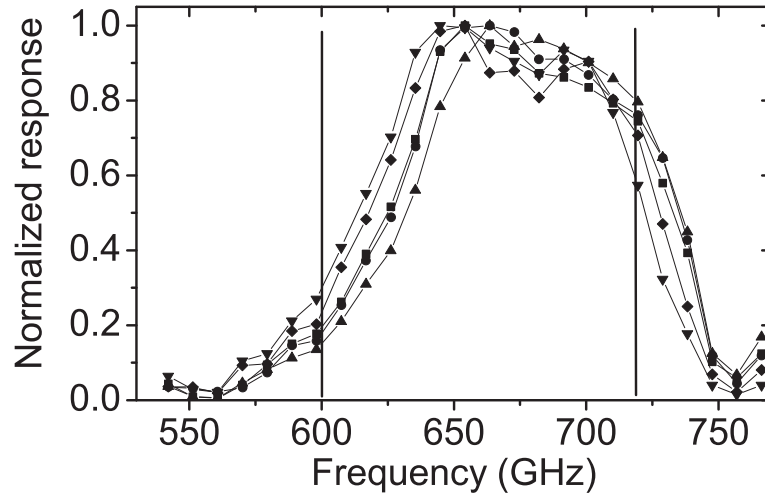


**Figure 6.1:** Normalized DC current response of identical SIS devices as a function of frequency, measured with a Fourier Transform Spectrometer. Vertical lines: ALMA Band 9.

## 6.1 Introduction

The aim of the research in this Chapter is to get adequate coverage of Band 9 of the Atacama Large Millimeter Array (ALMA) and a similar response for all 80 devices, using the established niobium technology with Nb/ $\text{AlO}_x$ /Nb SIS junctions and a Nb/ $\text{SiO}_2$ /Nb microstrip tuning circuit. The latter is needed to match the antenna impedance  $Z_{ant}$  [1].

The astronomical observation time is determined by the sensitivity of the detector, represented by the noise temperature  $T_N$ . Since the transmission efficiency  $T$  is a measure for the power coupling from the probe point to the SIS junction, we expect that a higher  $T$  results in a lower input noise temperature of the receiver, if the mixer conversion gain remains constant.

The transmission efficiencies of the matching circuits are evaluated using a Fourier Transform Spectrometer (FTS). We have measured the FTS response of several SIS devices with identical parameters. Five of those responses are shown in Fig. 6.1. Obviously, the spread is about 30 GHz, in spite of their equality.

## 6.2 Matching circuit model and antenna impedance

The data in Fig. 6.1 were taken on devices that all had the same tuning circuit design and of which the normal resistance varied between  $22.8 \Omega$  and  $23.9 \Omega$ . This can be translated in a variation in the junction area (see Section 6.3) between

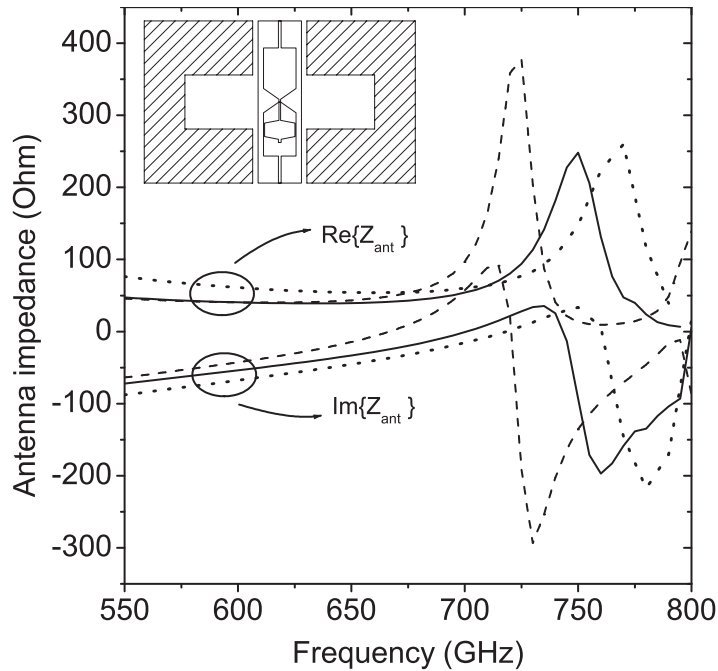


**Figure 6.2:** Real and imaginary part of the antenna impedance, as calculated with HFSS. Graphs show the calculation for the designed antenna position (nominal) and for a  $20 \mu\text{m}$  vertical shift in the channel (dashed line). Also shown is the impedance for a  $5 \mu\text{m}$  thinner than nominal substrate (dotted line). Inset: positioning of device chip in waveguide.

$0.83$  and  $0.87 \mu\text{m}^2$ , which causes a spread of about  $5 \text{ GHz}$ . The variation shown in Fig. 6.1 is too large to expect comparable noise temperatures over the full bandwidth.

The incoming radiation is coupled to the devices via a horn antenna attached to a waveguide. The SIS device chip is manually mounted in a channel to assure that the probe point is in the middle of the waveguide. (See inset of Fig. 6.2.)

The mounting has two possible uncertainties. Firstly, the accuracy with which the device is mounted in the substrate channel is in our case  $\pm 20 \mu\text{m}$  horizontally and vertically from the middle. The dashed line in Fig. 6.2, calculated with HFSS, shows the effect of a  $20 \mu\text{m}$  vertical shift on  $Z_{ant}$ . Secondly, the quartz substrate thickness, which is thinned before mounting from  $200 \mu\text{m}$  to the nominal design value of  $40 \mu\text{m}$ , with a limited accuracy of  $\pm 8 \mu\text{m}$ . The effect of a  $5 \mu\text{m}$  thinner substrate on  $Z_{ant}$  is shown by the dotted line in Fig. 6.2. It can be seen that these changes cause substantial scatter in the antenna impedance over the whole band, especially pronounced above  $700 \text{ GHz}$ .

To simulate the behavior of the Nb/SiO<sub>2</sub>/Nb matching circuits, we use a model that calculates for each frequency point the surface impedance  $Z_s$  of Nb microstrips in the local limit using the Mattis-Bardeen theory of the anomalous

skin effect [2] for the complex conductivity  $\sigma$  with an appropriate normal conductivity  $\sigma_n$  and gap energy  $2\Delta$  of the top and bottom superconducting layer of the microstripline (see Section 6.3):

$$Z_s = \sqrt{\frac{i\omega\mu_0}{\sigma}} \coth(\sqrt{i\omega\mu_0\sigma}d), \quad (6.1)$$

where  $d$  is the thickness of the microstrip and  $\omega$  is the angular frequency;  $\mu_0$  represents the permeability of free space. The series impedance per unit length  $Z'_{ser}$  of a part of the microstripline is now the sum of the geometrical inductance and the surface impedance of the top and bottom superconductor:

$$Z'_{ser} = \frac{Z_{s,bot} + Z_{s,top}}{W_i} + \frac{i\omega\mu_0d_d}{W_i}, \quad (6.2)$$

with  $W_i$  the width of the part of the microstripline (see also Fig 6.3), and  $d_d$  the thickness of the dielectric layer. The parallel admittance per unit length  $Y'_{par}$  is formed by the capacitance of the dielectric layer:

$$Y'_{par} = \frac{i\omega\epsilon_r\epsilon_0W_i}{d_d}, \quad (6.3)$$

where  $\epsilon_r$  is the dielectric constant of the dielectric layer and  $\epsilon_0$  is the permittivity of free space. The corrections proposed by Yassin and Withington [3] are smaller than the variations caused by the changes in antenna impedance. Using standard transmission line theory [4], for each part of the microstripline a propagation constant  $\gamma = \sqrt{Z'_{ser}Y'_{par}}$  and a characteristic impedance  $Z_0 = \sqrt{Z'_{ser}/Y'_{par}}$  can be derived; using these two parameters and the length  $L_i$  of a microstripline section (Fig. 6.3) a transmission (or ABCD) matrix is defined.

For the complete microstripline, the transmission matrix can be calculated by matrix multiplication. For a strip line consisting of  $n$  parts, this yields  $M_{tot} = M_1.M_2.(...).M_n$ , where the  $M_i$ 's are the individual ABCD matrices.

The total transmission of electromagnetic radiation of a certain frequency from the RF probe to the SIS junction is found as follows. A matrix  $M_{j,im}$  is calculated for the imaginary part of the junction impedance  $i \times \Im\{R_n/(1 + i\omega R_n C_j)\} = -i\omega R_n^2 C_j/(1 + \omega^2 R_n^2 C_j^2)$  (with  $R_n$  the junction normal resistance and  $C_j$  the junction capacitance) and a matrix  $M_{a,im}$  for the imaginary part of the antenna impedance [4]. From this, a final transmission matrix  $X$  is calculated:  $X = M_{j,im}.M_{tot}.M_{a,im}$ . Using the real part of the junction impedance,  $R_j = R_n/(1 + \omega^2 R_n^2 C_j^2)$ , and the real part of the antenna impedance,  $R_a$ , the total transmission efficiency  $T(f)$  at frequency  $f$  reads

$$T(f) = \frac{4R_j R_a}{|R_a X_{1,1} + X_{1,2} + R_j R_a X_{2,1} + R_j X_{2,2}|^2}, \quad (6.4)$$

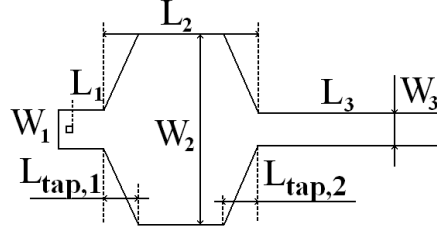


**Figure 6.3:** Schematic picture of the tuning structure. The microstripline is defined by the widths  $W_i$  and lengths  $L_i$  of its sections, as well as the tapering lengths  $L_{tap,i}$ .

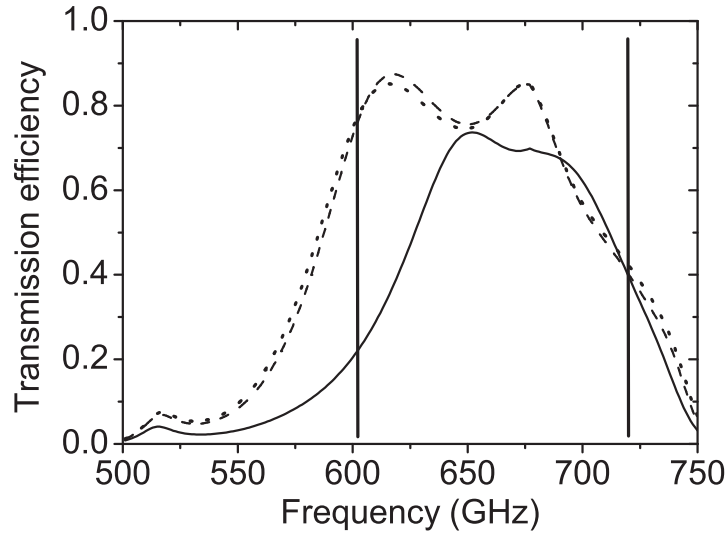


**Figure 6.4:** Calculated transmission efficiencies for non-optimized design (full line), optimized rectangular design (dashed) and optimized tapered design (dotted). In the calculation,  $\sigma_n = 1.0 \times 10^7$  S/m and the empirical antenna impedance have been used. Vertical lines indicate the ALMA band of interest.

where the  $X_{i,j}$ 's are the matrix elements of the final transmission matrix  $X$ .

Apart from the HFSS antenna impedance, we have also used an empirical antenna impedance. The real and imaginary parts of the empirical antenna impedance are exponential and polynomial approximations to the actual impedances. They are derived by an iterative search (starting from the initial HFSS results) that minimizes the error between the average of five of the FTS measurements in Fig. 6.1 and simulation. This empirical impedance accounts for scatter in the actual antenna impedance and absorbs model uncertainties like  $\sigma$  and discontinuities in the Nb microstriplines.

In order to match the circuit to the band, we have optimized the geometrical shape of the microstripline. Optimization is done for the highest average

**Table 6.1:** Average transmission efficiency,  $T_{avg}$ , and useful bandwidth  $B_W$  for three designs, calculated with empirical antenna impedance and HFSS simulated antenna impedance.

Design	Empirical antenna		HFSS antenna	
	$T_{avg}$	$B_W$ (GHz)	$T_{avg}$	$B_W$ (GHz)
Non-optimized previous	54%	99	53%	94
Optimized rectangular	73%	103	72%	103
Optimized linear tapering	73%	103	72%	103

transmission efficiency, given by

$$T_{avg} = \int_{\Delta f} T(f) df / \Delta f, \quad (6.5)$$

where  $\Delta f$  is the frequency range of interest. By investigating the 8-dimensional space set by the lengths and widths that define the shape of the microstripline (see Fig. 6.3), the optimal  $T_{avg}$  is sought.

In Fig. 6.4, the simulation results for a non-optimized previous design [1] (full line) are compared with those of a linearly tapered (dotted) and rectangular (dashed) optimized design. The band coverage of the optimized designs is clearly better.

In Table 6.1, the average transmission efficiency and useful bandwidth, in Band 9, of the previous design is compared with that of two optimized designs. (Fig. 6.3: a rectangular design is one with  $L_{tap,i} = 0$  for  $i = 1, 2$ .) It is evident that the expected increase in  $T_{avg}$  is about 20% for the optimized designs, irrespective of whether the tuning microstripline takes a rectangular or linearly tapered shape.

### 6.3 Materials and devices

The mixers incorporate a multisection microstripline that tunes out the capacitance of the SIS junction. The structures consist of a superconducting ground plane with a thickness of 200 nm Nb, 5 nm Al, an about 1 nm thick layer of  $\text{AlO}_x$  as the tunnel barrier and a 500 nm Nb top wire. A 250 nm layer of  $\text{SiO}_2$  separates ground plane and top wire. Contact pads are made of 50 nm thick Au.

The normal resistance-area product ( $R_n A$ ) is determined by measuring the normal resistance of a big ( $25 \mu\text{m}^2$ ) area junction. We use barriers with  $R_n A$

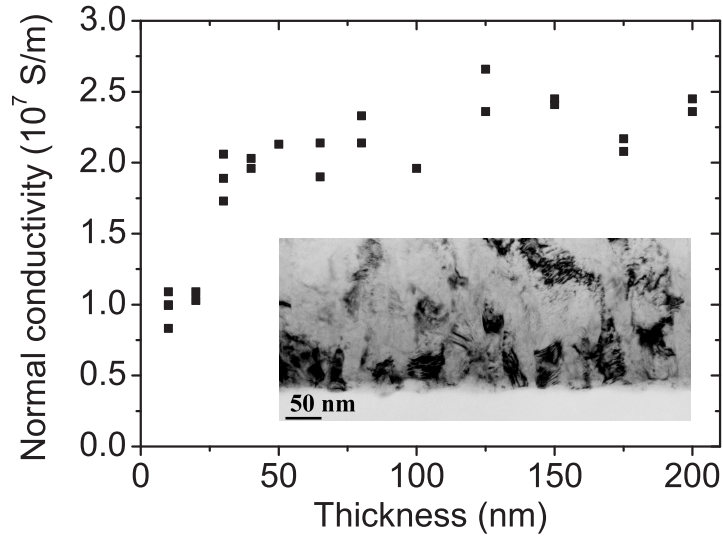


**Figure 6.5:** Four point measurements of normal conductivity of niobium at 10 K as a function of thickness. Data were taken from Hall bar structures which were deposited on top of a 250 nm layer of SiO<sub>2</sub>. Inset shows a bright field transmission electron micrograph of Nb layer on top of SiO<sub>2</sub>, showing the increase in grainsize over the thickness.

down to  $20 \Omega\mu\text{m}^2$ . The area of the small junctions, defined by electron-beam lithography, is determined from the measurement of  $R_n$ . Knowing this area, the junction capacitance is fixed by the specific capacitance of the junction barrier, for which we have consistently used  $80 \text{ fF}/\mu\text{m}^2$ .<sup>i</sup>

DC four point measurements of 200nm Nb lines at a temperature of about 10K, just above the critical temperature ( $T_c$ ) of Nb, have yielded for the normal conductivity  $\sigma_{n,DC} = 2.5 \times 10^7 \text{ S/m}$  ( $4.0 \mu\Omega\text{cm}$ ). However, when we compare our simulations with FTS results, we find that  $\sigma_{n,RF} = 1.0 \times 10^7 \text{ S/m}$  ( $10 \mu\Omega\text{cm}$ ) fits best with our data.<sup>i</sup> We attribute this to the fact that at high frequencies, most current is concentrated in a thin part of the Nb line, on top of the dielectric SiO<sub>2</sub>, where the normal conductivity is lower than the bulk value. This is supported by the data in Fig. 6.5, where  $\sigma_n$  for a Nb Hall bar structure on top of a layer of 250 nm SiO<sub>2</sub> is measured just above  $T_c$  for different film thicknesses  $t$ . In Fig. 6.5 it is apparent that  $\sigma_n$  decreases for small  $t$  for which one can notice the agreement with our FTS-fitted  $\sigma_{n,RF} = 1.0 \times 10^7 \text{ S/m}$ . This is further substantiated by a transmission electron micrograph in the inset of Fig. 6.5, where we can see an increase in grainsize over the thickness.<sup>ii</sup>

<sup>i</sup>Our most recent views on the use of the device parameters in our modeling are discussed in Section 8.3 and summarized in Section 8.7.

<sup>ii</sup>We have recently found out that the RF normal conductivity of the *bottom* superconductor also differs substantially from the DC value. For more details, see Section 8.2.

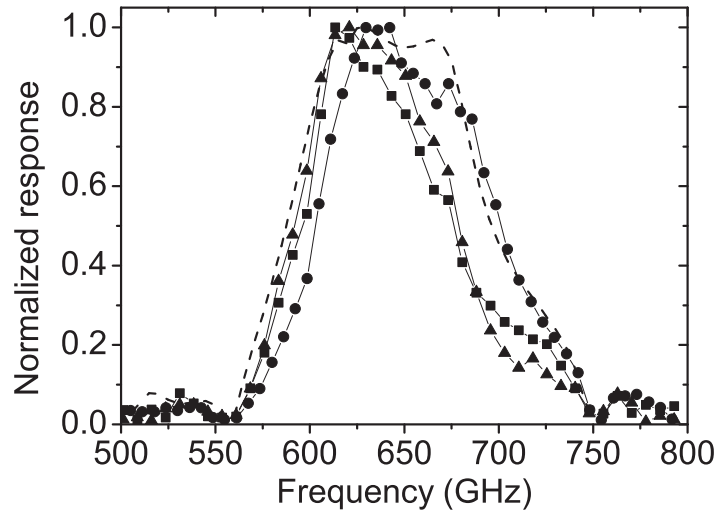


**Figure 6.6:** Fourier Transform Spectrometry measurements of three optimized linearly tapered designs (line+symbol) compared with model simulation with the device parameters inferred, taking into account atmospheric transmission, optics and SIS responsivity (dashed).

## 6.4 Test results

We have fabricated devices with optimized rectangular and tapered designs. The frequency response has been determined using a Fourier Transform Spectrometer (FTS) by measuring the changes produced by the incoming light in the bias current at a particular chosen bias voltage which is selected to be close to the gap voltage in the IV curve.

In Fig. 6.6, results of three devices with an optimized linearly tapered design are presented (line+symbol). The  $R_n A$  is  $25.6 \Omega \mu\text{m}^2$ , while the average  $R_n$  of the junctions is  $31.7 \pm 0.5 \Omega$ . Clearly, the spread in FTS responses is of the same order as in Fig. 6.1.

The noise temperature of the mixer, the accompanying optics and IF chain [5] has been measured using the standard Y-factor method. The resulting uncorrected DSB noise temperatures  $T_N$  at different frequencies are presented in Fig. 6.7.

The noise temperatures  $T_N$  of devices with a non-optimized design (empty symbols) are compared with devices with an optimized design (filled symbols). The data shown by empty squares are from previous measurements, the empty triangles represent recent measurements of a different device with the same design. For frequencies below 630 GHz, the new optimized design has a  $T_N$  of almost the same level as the best results of the non-optimized design. At higher frequencies, the non-optimized design still has the best noise temperatures.

For comparing simulations with FTS measurements, several effects due to

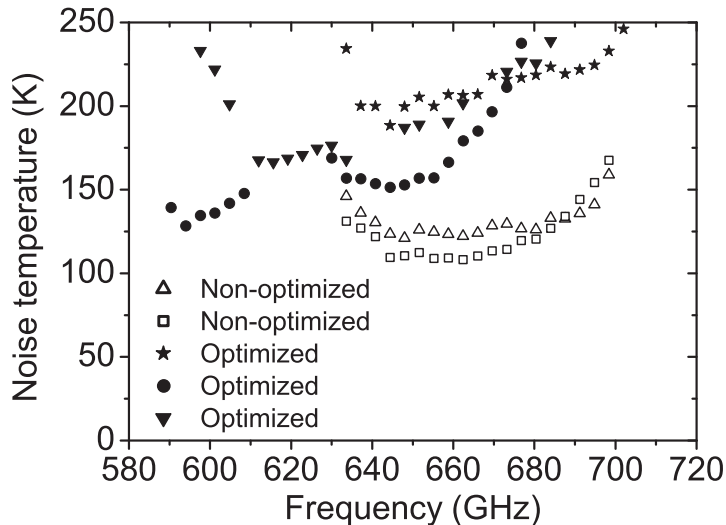


**Figure 6.7:** Noise temperature measurements of non-optimized designs (empty symbols) compared with optimized designs (filled symbols). Although the  $T_{avg}$  of the non-optimized devices is lower, their  $T_N$  shows a better result.

non-ideal measurement have been taken into account in the simulation, namely the beamsplitter and cryostat windows transmissions, laboratory atmospheric transmission [6], and  $1/f$  dependence of direct detection responsivity of the SIS junction [7]. The simulation result is shown in Fig. 6.6 (dashed line). We find a good agreement with data when using actual device parameters,  $\sigma_{n,RF} = 1.0 \times 10^7$  S/m and the empirical antenna impedance.

## 6.5 Conclusions and discussion

We have analyzed the use of Nb/ $\text{AlO}_x$ /Nb SIS junctions with Nb/ $\text{SiO}_2$ /Nb matching circuits to get full band coverage. We conclude it is hardly possible to get adequate band coverage using nominally identical devices for all 50 telescopes. This originates in the fundamental limitation of the bandwidth ( $\sim 100$  GHz) [8] by the  $RC$ -constant of the junction and the losses in the Nb microstriplines at frequencies above the gap.

A possible solution to this is using junctions with higher current density barriers, e.g. AlN, which are expected to have a larger bandwidth [9]. To investigate this hypothesis further, we have optimized a design for a high current density junction, assuming a  $R_n A$  of  $5 \Omega \mu\text{m}^2$  and a  $C_s$  of  $80 \text{ fF}/\mu\text{m}^2$ .<sup>iii</sup> The result is shown by the dash-dotted line in Fig. 6.8, together with an optimized curve for

<sup>iii</sup>Our most recent views on the use of the device parameters in our modeling are discussed in Section 8.3 and summarized in Section 8.7.

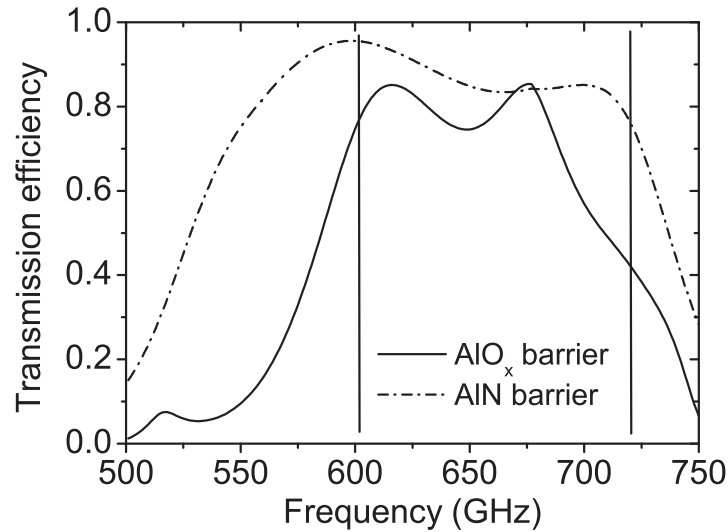


**Figure 6.8:** Transmission efficiency of an optimized design for an  $\text{AlO}_x$  barrier (full line) and for an AlN barrier (dash dot). The vertical lines indicate the band from 600 to 720 GHz.

an  $\text{AlO}_x$  junction (full line). Clearly, the AlN curve has a much wider bandwidth and will be able to accommodate the variations in antenna impedance.

In summary, it has been demonstrated that by proper optimization, an average transmission efficiency of the order of 70% can be achieved, irrespective of whether the tuning circuit takes a rectangular or tapered shape. We have found that the normal conductivity of Nb used in the RF model is lower than the DC conductivity. We relate this to the fact that there is an inhomogeneous conductivity over the thickness. Despite of the fact that an optimized geometry has a 20% higher average transmission efficiency we do not find an improved noise temperature. The mixer conversion gain should be included in the model for a proper noise analysis [10].

## References

- [1] C. F. J. Lodewijk, M. Kroug, T. M. Klapwijk, F. P. Mena, A. M. Baryshev, and W. Wild, “Improved design for low noise Nb SIS devices for Band 9 of ALMA (600 - 720 GHz)”, in Proc. of the 16th Int. Symp. on Space THz Techn., 42 (2005).
- [2] D. C. Mattis and J. Bardeen, “Theory of the Anomalous Skin Effect in Normal and Superconducting Metals”, Phys. Rev., vol. 111, 412 (1958).
- [3] G. Yassin and S. Withington, “Electromagnetic models for superconducting millimetre-wave and sub-millimetre-wave microstrip transmission lines”, J. Phys. D: Appl. Phys. Vol. **28**, 1983 (1995).

- 
- [4] D. M. Pozar, *Microwave Engineering*, John Wiley and Sons, USA (1998).
  - [5] A. Baryshev, E. Lauria, R. Hesper, T. Zijlstra, and W. Wild, “Fixed-tuned waveguide 0.6 THz SIS mixer with wide band IF”, ALMA memo 429 (2002).
  - [6] The program that calculates the atmospherical transmission has ben provided by J. R. Pardo-Carrion, Departamento de Astrofisica Molecular e Infraroja, Consejo Superior de Investigaciones Cientificas, Madrid, Spain.
  - [7] M. C. Gaidis, H. G. LeDuc, M. Bin, D. Miller, J. A. Stern, and J. Zmuidzinas, “Characterization of Low-Noise Quasi-Optical SIS Mixers for the Submillimeter Band”, IEEE Trans. Microw. Theory Techn., Vol. **44**, 1130 (1996).
  - [8] A. R. Kerr, “Some fundamental and practical limits on broadband matching to capacitive devices, and the implications for SIS mixer design”, IEEE Trans. Microw. Theory Tech., Vol. **43**, 2 (1995).
  - [9] J. Kawamura, D. Miller, J. Chen, J. Zmuidzinas, B. Bumble, H. G. LeDuc, and J. A. Stern, “Very high-current-density Nb/AlN/Nb tunnel junctions for low-noise submillimeter mixers”, Appl. Phys. Lett., Vol. **76**, 2119 (2000).
  - [10] J. R. Tucker and M. J. Feldman, “Quantum detection at millimeter wavelengths”, Rev. Mod. Phys., Vol. **57**, 1055 (1985).



## Chapter 7

# Epitaxial aluminum-nitride tunnel barriers grown by nitridation with a plasma source

High critical current-density (10 to 420 kA/cm<sup>2</sup>) superconductor-insulator-superconductor tunnel junctions with aluminum nitride barriers have been realized using a remote nitrogen plasma from an inductively coupled plasma source operated in a pressure range of 10<sup>-3</sup> to 10<sup>-1</sup> mbar. We find a much better reproducibility and control compared to previous work. From the current-voltage characteristics and cross-sectional TEM images it is inferred that, compared to the commonly used AlO<sub>x</sub> barriers, the poly-crystalline AlN barriers are much more uniform in transmissivity, leading to a better quality at high critical current-densities.

---

Most of this Chapter has been published as: T. Zijlstra, C. F. J. Lodewijk, N. Vercruyssen, F. D. Tichelaar, D. N. Loudkov, and T. M. Klapwijk, "Epitaxial aluminum-nitride tunnel barriers grown by nitridation with a plasma source", *Appl. Phys. Lett.*, Vol. **91**, 233102 (2007).

## 7.1 Introduction

Quantum technology based on superconducting or magnetic metals uses nanometer thick tunnel barriers. Many routes to quantum computation are based on aluminum with aluminum oxide barriers. Niobium devices use a proximitized layer of aluminum with a similar oxide [1]. Magnetic tunnel junctions have recently moved from using amorphous aluminum oxide to epitaxial magnesium oxide with its unique spin-dependent properties [2, 3]. In quantum computation the amorphous tunnel barrier has surfaced as an important source of decoherence leading to the introduction of an epitaxial aluminum oxide barrier [4, 5]. On the other hand highly transmissive tunnel barriers are urgently needed for sub-millimeter mixers in order to achieve a high bandwidth [6], in electronic refrigeration to maximize the cooling power [7] and in high density magnetic memory devices [8].

## 7.2 Uniformity of tunnel barriers

It has been demonstrated that a major problem of amorphous  $\text{AlO}_x$  barriers is that they are laterally inhomogeneous [9, 10]. We take this into account by using a distribution of transparencies  $T_n$  by writing for the voltage-independent normal conductance:

$$G \propto \sum_n A_n T_n, \quad (7.1)$$

with  $A_n$  a fraction of the total area of the tunnel barrier with an assumed uniform transmissivity  $T_n$ . Hence, we do not assume a universal distribution of transparencies [11, 12] but one which is related to a distribution of areas with different transmissivities, resulting from the technological process. For superconducting tunnel junctions (SIS) this amounts to a situation analogous to superconducting quantum point contacts [13]:

$$I \propto \sum_n A_n j(V, T_n), \quad (7.2)$$

with  $I$  the total current and  $j(V, T_n)$  the voltage-dependent current-density per area  $A_n$ .  $j$  contains contributions of different orders proportional to  $T_n$ ,  $T_n^2$ ,  $T_n^3$ , etcetera, reflecting multiple Andreev reflections ( $j(V, T_n) = j_1(V, T_n) + j_2(V, T_n^2) + j_3(V, T_n^3) + \dots$ ). For the commonly used low current-density tunnel barriers most  $A_n$  have  $T_n$  of the order of  $10^{-4}$ . Since for SIS junctions first order tunneling  $j_1$  leads to a zero subgap current, the remaining subgap current is due to the higher order terms ( $j_2, j_3, \dots$ ), which only appear for  $T_n \approx 1$ . Non-uniformity, causing the emergence of areas with  $T_n \approx 1$ , thus leads to excessive subgap currents. Therefore the critical current density of amorphous aluminum oxide barriers is limited to 20 kA/cm<sup>2</sup> [14]. We will demonstrate that aluminum nitride barriers are superior to aluminum oxide barriers with respect to barrier uniformity.

## 7.3 Barrier realization procedure

In the work reported here a very good reproducibility is realized by using the afterglow region of a nitrogen plasma from an inductively coupled plasma source (COPRA) (see for example Weiler [15]), from CCR technology. The plasma provides the energy to split the  $N_2$  molecules into N radicals, needed for the growth of AlN. The source is mounted on a vacuum chamber. The plasma is created in the source and diffuses into the chamber. We have chosen to work in a range of high pressures ( $2 \times 10^{-3}$  mbar to  $1 \times 10^{-1}$  mbar), for two reasons. First, we expect at these higher pressures a larger fraction of atomic N. Secondly, the ion energies in this regime are as low as a few eV, which minimizes damage to the barrier-formation. This is different from recent work, where the plasma process not only provides the chemically active species but also creates damage by highly energetic ions [16, 18, 17, 19, 20] (although usable routes have been reported [18]). In addition many other plasma techniques suffer from instabilities, resulting in a poor process reproducibility.

The devices are fabricated on a 2 inch oxidized silicon or fused quartz substrate. All metal layers are deposited by magnetron sputtering in the process chamber of a Kurt Lesker system. First, a 100 nm Nb monitor layer is deposited, after which a ground plane pattern is optically defined. Subsequently, a bilayer of 100 nm Nb and about 7 nm Al is deposited. Without breaking the vacuum, the substrate is then transferred to a nitridation chamber, where the Al is exposed to the nitrogen plasma for several minutes, producing a layer of AlN. The substrate is then again *in vacuo* transferred to the process chamber, where a top electrode of 200 nm Nb is deposited. The lateral dimensions of the multilayer of Nb/Al/AlN/Nb are patterned by lift-off. Junctions are defined by e-beam lithography with a negative e-beam resist (SAL-601) layer and reactively ion etched (RIE) with a  $SF_6/O_2$  plasma using the AlN as an etch-stop, followed by a mild anodization (5 V). The junction resist pattern is used as a self-aligned lift off mask for a dielectric layer of 250 nm  $SiO_2$ . A 500 nm Nb/50 nm Au top layer is deposited and Au is etched with a wet etch in a KI/I<sub>2</sub> solution using an optically defined mask. Finally, using an e-beam defined top wire mask pattern, the layer of Nb is etched with a  $SF_6/O_2$  RIE, which finishes the fabrication process.

## 7.4 Reproducibility of results

The fabrication process used provides a very good reproducibility. There is reproducibility within one fabrication run, illustrated by the similarity of junctions on a produced wafer. Scatter in the normal resistance  $R_n$  of the junctions is caused by variation in the junction area  $A$ , due to uncertainties in junction definition, and variation in the barrier-specific  $R_n A$  value. For 34 junctions, of which 14 are shown in Fig. 7.1, the standard deviation,  $\sqrt{\sum_{i=1}^m (R_{n,i} - \langle R_n \rangle)^2 / (m - 1)}$ ,

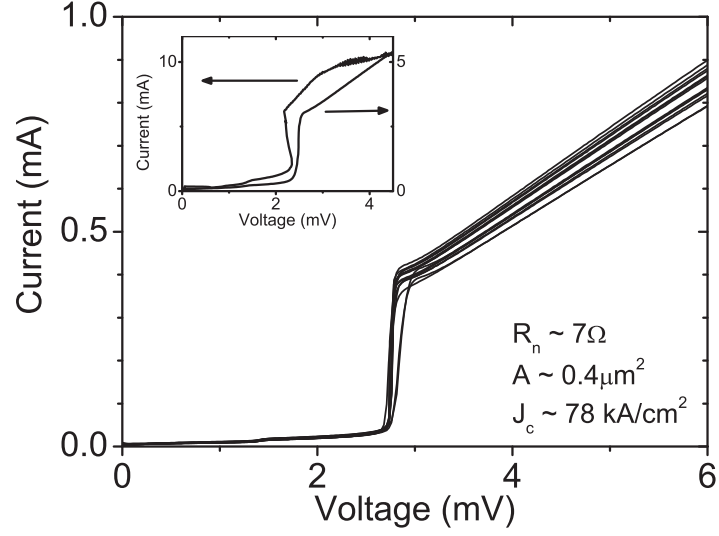


**Figure 7.1:** Current-voltage characteristics of a typical batch of Nb/AlN/Nb junctions. Junction area is about  $0.4 \mu\text{m}^2$ , for a normal resistance,  $R_n$ , of  $6.8 \Omega$  (critical current density  $\sim 78 \text{ kA/cm}^2$ ). The Josephson current has been suppressed with a magnetic field. Inset shows IV characteristics of SIS junctions with  $J_c$  of  $130 \text{ kA/cm}^2$  and  $420 \text{ kA/cm}^2$ . For the latter thermal heating causes gap-suppression and back-bending.

with  $m$  the number of junctions, of  $R_n$  has been determined to be 3.3 % relative to the average,  $\langle R_n \rangle = 6.8 \Omega$ . The peak-to-peak variation amounts to  $\pm 6 \%$ . By measuring four big junctions (two of  $1 \mu\text{m}^2$  and two of  $2 \mu\text{m}^2$ ), the value of  $R_n A$  has been found to be  $2.8 \Omega \mu\text{m}^2$  (corresponding to a critical current density  $J_c \approx 78 \text{ kA/cm}^2$ ). Assuming perfect junction definition (which is most likely not the case), the standard deviation of  $R_n A$  within one fabrication run is at most 3.3 %. Based on the average  $R_n$ ,  $A$  is  $0.4 \mu\text{m}^2$ .

We also find a good reproducibility from run to run. We have made several batches, varying the nitridation time  $t_N$  from 9 to 60 minutes. About half of the batches has been made with a low position of the chuck (30 cm distance to the plasma source) in the nitridation chamber, the other half with a higher position (15 cm distance to the plasma source). In Fig. 7.2, we plot the  $R_n A$  product of the batches as a function of  $t_N$  for the large chuck-source distance (squares) and for the small chuck-source distance (diamonds). The dashed lines indicate a dependence  $R_n A \propto t_N^k$ , with  $k = 1.4$ . Obviously, there is a systematic dependence on nitridation time, indicating a well-behaving process. By varying the nitridation time and/or the chuck position, we can realize any desired  $R_n A$  value between  $0.5 \Omega \mu\text{m}^2$  and  $10 \Omega \mu\text{m}^2$ .

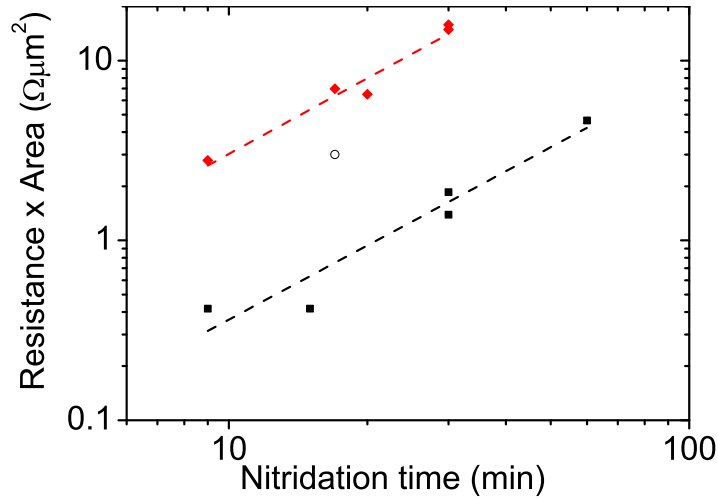


**Figure 7.2:**  $R_n A$  product as a function of nitridation time,  $t_N$ , for nine different fabricated batches. The squares represent data for a 30 cm chuck-source distance, whereas the diamonds indicate a 15 cm chuck-source distance. The open circle represents the junctions of Fig. 7.1. Dashed lines indicate both a dependence  $R_n A \propto t_N^{1.4}$ .

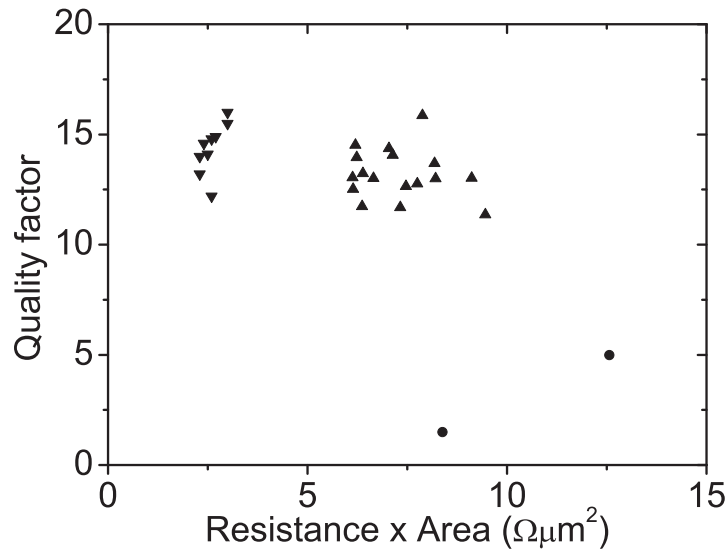


**Figure 7.3:** Quality factor as a function of  $R_n A$  product for two batches of Nb/AlN/Nb junctions (up- and down-pointing triangles). Also indicated are  $\text{AlO}_x$  data from Miller *et al.* [14] (filled circles).

## 7.5 Analysis of barrier uniformity

The quality factor  $Q$ , defined as  $R_{sg}/R_n$ , where  $R_{sg}$  is the subgap resistance, gives an indication of the subgap leakage through the tunnel barrier. In Fig. 7.3,  $Q$

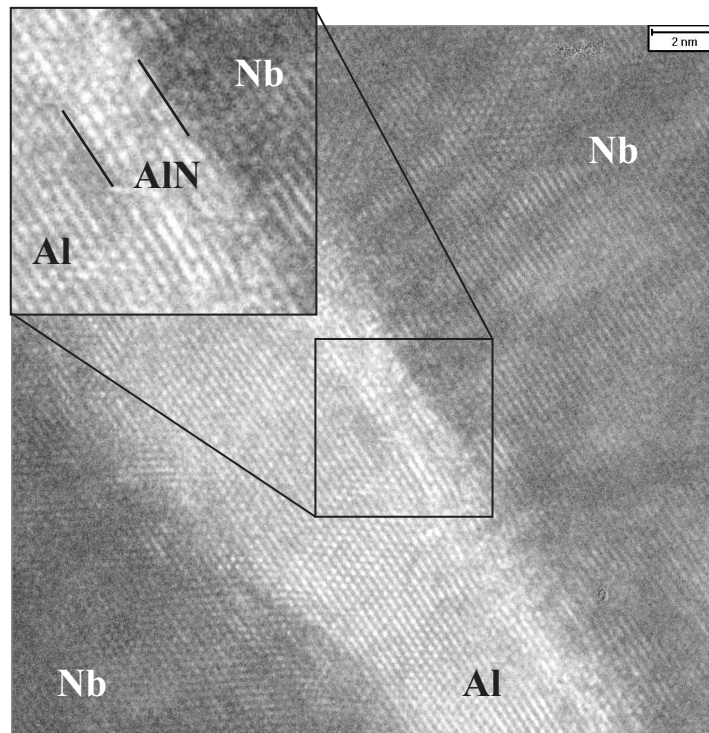


**Figure 7.4:** High resolution transmission electron microscope (HRTEM) micrographs of an AlN dielectric barrier deposited on an Al layer (bright region) between Nb electrodes (dark regions). The bar in the top-right corner represents a length of 2 nm.

has been plotted for two different batches of AlN based junctions, together with data on  $\text{AlO}_x$  from Miller *et al.* [14]. In contrast to these  $\text{AlO}_x$  devices, it is evident that  $Q$  is higher than 10 for all AlN devices. The lower subgap currents prove that our AlN barriers have a lower density of areas with  $T_n \approx 1$ , in other words a better uniformity.

As shown in Fig. 7.2, we reach  $R_n A$  products as low as  $0.4 \Omega \mu\text{m}^2$ , corresponding to a  $J_c$  of  $420 \text{ kA}/\text{cm}^2$ . For such high current densities, heating effects decrease the superconducting gap voltage of the junction in the form of back-bending (Fig. 7.1 Inset). Up to at least  $130 \text{ kA}/\text{cm}^2$ , this effect remains hidden, but is still present. This indicates that for these AlN barriers the maximum critical current density is no longer limited by the materials control of the barrier, but by the intrinsic physical process of nonequilibrium in the electrodes. Consequently, a future detailed statistical evaluation of reproducibility and control has to take into account the distortions of the  $IV$  curves by heating.

Using high-resolution transmission electron microscopy (HRTEM) we find that the AlN-barrier is grown epitaxially (Fig. 7.4). The barrier is visible as a region with higher transmission (most bright region) and in a small difference in lattice spacing for Al and AlN. The images clearly indicate epitaxial alignment

of the crystalline structure of the AlN with the underlying Al crystal. The lattice plane distances of the planes parallel to the surface were measured in various locations and identified as either  $\{0002\}$  or  $\{1\bar{1}01\}$  planes in the hexagonal AlN phase, with spacing  $2.49 \pm 0.06$  Å and  $2.37 \pm 0.06$  Å respectively. An averaged thickness of the barrier of about  $1.5 \pm 0.5$  nm is found. For these devices the  $R_n A$  value is about  $16 \Omega \mu\text{m}^2$ . Obviously, in contrast to the commonly used  $\text{AlO}_x$ , the AlN tunnel barrier has a crystalline nature with a thickness of about 6 lattice planes, which may be the cause of the better uniformity.

## 7.6 Conclusion

Epitaxial aluminum-nitride tunnel barriers have been grown, at ambient temperature, using a plasma-source to generate chemically active nitrogen. This method shows significantly better reproducibility than other AlN growth techniques have shown in the past. Compared to the conventionally used aluminum oxide barriers, much better quality current-voltage characteristics are observed for high critical current densities, which is attributed to a spatially more uniform transmissivity of the epitaxial tunnel barrier.

## References

- [1] M. Gurvitch, M. A. Washington, and H. A. Huggins, “High quality refractory Josephson tunnel junctions utilizing thin aluminum layers”, *Appl. Phys. Lett.* **42**, 472 (1983).
- [2] S. S. P. Parkin, C. Kaiser, A. Panchula, P. M. Rice, B. Hughes, M. Samant, S.-H. Yang, “Giant tunnelling magnetoresistance at room temperature with MgO (100) tunnel barriers”, *Nature Materials* **3**, 862 (2004).
- [3] S. Yuasa, T. Nagahama, A. Fukushima, Y. Suzuki, and K. Ando, “Giant room-temperature magnetoresistance in single-crystal Fe/MgO/Fe magnetic tunnel junctions”, *Nature Materials* **3**, 868 (2004).
- [4] S. Oh, K. Cicak, R. McDermott, K. B. Cooper, K. D. Osborn, R. W. Simmonds, M. Steffen, and D. P. Pappas, “Low-leakage superconducting tunnel junctions with a single-crystal  $\text{Al}_2\text{O}_3$  barrier”, *Superc. Sci. Technol.* **18**, 1396 (2005).
- [5] S. Oh, K. Cicak, J. S. Kline, M. A. Sillanpää., K. D. Osborn, J. D. Whitaker, R. W. Simmonds, and D. P. Pappas, “Elimination of two level fluctuators in superconducting quantum bits by an epitaxial tunnel barrier”, *Phys. Rev. B* **74**, 100502(R)(2006).

- [6] J. Kawamura, D. Miller, J. Chen, J. Zmuidzinas, B. Bumble, H. G. LeDuc, and J. A. Stern, “Very high-current-density Nb/AlN/Nb tunnel junctions for low-noise submillimeter mixers”, *Appl. Phys. Lett.* **76**, 2119 (2000).
- [7] F. Giazotto, T. T. Heikkila, A. Luukanen, A. M. Savin, J. P. Pekola, “Opportunities for mesoscopics in thermometry and refrigeration: physics and applications”, *Rev. Mod. Phys.* **78**, 217 (2006).
- [8] K. Tsunekawa, D. D. Djayaprawira, S. Yuasa, M. Nagai, H. Maehara, S. Yamagata, E. Okada, N. Watanabe, Y. Suzuki, and K. Ando, “Huge magnetoresistance and low junction resistance in magnetic tunnel junctions with crystalline MgO barrier”, *IEEE Trans. Magn.* **42**, 103 (2006).
- [9] W. H. Rippard, A. C. Perrella, F. J. Albert, and R. A. Buhrman, “Ultrathin aluminum oxide tunnel barriers”, *Phys. Rev. Lett.* **88**, 046805 (2002).
- [10] K. M. Lang, D. A. Hite, R. W. Simmonds, R. McDermott, D. P. Pappas, and J. M. Martinis, “Conducting atomic force microscopy for nanoscale tunnel barrier characterization”, *Rev. Sci. Instr.* **75**, 2726 (2004).
- [11] K. M. Schep, and G. E. W. Bauer, “Universality of transport through dirty interfaces”, *Phys. Rev. Lett.* **78**, 3015 (1997).
- [12] Y. Naveh, V. Patel, D. V. Averin, K. K. Likharev, and J. E. Lukens, “Universal distribution of transparencies in highly conductive Nb/AlO<sub>x</sub>/Nb junctions”, *Phys. Rev. Lett.* **85**, 5404 (2000).
- [13] E. Scheer, P. Joyez, D. Esteve, C. Urbina, and M. H. Devoret, “Conduction channel transmission of atomic-size aluminum contacts”, *Phys. Rev. Lett.* **78**, 3535 (1997).
- [14] R. E. Miller, W. H. Mallison, A. W. Kleinsasser, K. A. Delin, and E. M. Macedo, “Niobium trilayer Josephson tunnel junctions with ultrahigh critical current densities”, *Appl. Phys. Lett.* **63**, 1423 (1993).
- [15] M. Weiler, K. Lang, E. Li, J. Robertson, “Deposition of tetrahedral hydrogenated amorphous carbon using a novel electron cyclotron wave resonance reactor”, *Appl. Phys. Lett.* **72**, 1314 (1998).
- [16] T. Shiota, T. Imamura and S. Hasuo, “Nb Josephson junction with an AlN<sub>x</sub> barrier made by plasma nitridation”, *Appl. Phys. Lett.* **61**, 1228 (1992).
- [17] Z. Wang, A. Kawakami, and Y. Uzawa, “NbN/AlN/NbN tunnel junctions with high current density up to 54 kA/cm<sup>2</sup>”, *Appl. Phys. Lett.* **70**, 114 (1997).
- [18] B. Bumble, H. G. LeDuc, J. A. Stern and K.G. Megerian, “Fabrication of Nb/Al-N<sub>x</sub>/NbTiN junctions for SIS mixer applications”, *IEEE Trans. Appl. Superconduct.* **11**, 76 (2001).

- 
- [19] A. B. Kaul, A. W. Kleinsasser, B. Bumble, H. G. LeDuc and K. A. Lee, “Aluminum nitride tunnel barrier formation with low-energy nitrogen ion beams”, *J. Mater. Res.* **20**, 3047 (2005).
- [20] N. N. Iosad, A. B. Ermakov, F. E. Meijer, B. D. Jackson, and T. M. Klapwijk, “Characterization of the fabrication process of Nb/Al-AlN<sub>x</sub>/Nb tunnel junctions with low  $R_nA$  values up to  $1 \Omega\mu\text{m}^2$ ”, *Supercond. Sci. Technol.* **15**, 945 (2002).



## Chapter 8

# Bandwidth limitations of Nb/AlN/Nb SIS mixers around 700 GHz

We study, using niobium-technology, the bandwidth of SIS mixers operating at frequencies close to the energy-gap frequency. Microstriplines of niobium - silicon dioxide - niobium have different properties for the top and bottom superconductor, which we find to depend on the used fabrication process. Replacing the  $\text{AlO}_x$  tunnel barrier by AlN, the bandwidth increases by 53 %. The measurements, using a Fourier Transform Spectrometer (FTS) and performed in ambient air, demonstrate that the bandwidth is no longer limited by the tuning circuit but by the atmospheric absorption of radiation. Excellent noise temperatures are found over a full band of 600 to 720 GHz.

---

Most of this Chapter has been submitted with authors C. F. J. Lodewijk, T. Zijlstra, S. Zhu, F. P. Mena, A. M. Baryshev, and T. M. Klapwijk, to IEEE Trans. Appl. Superconductivity.

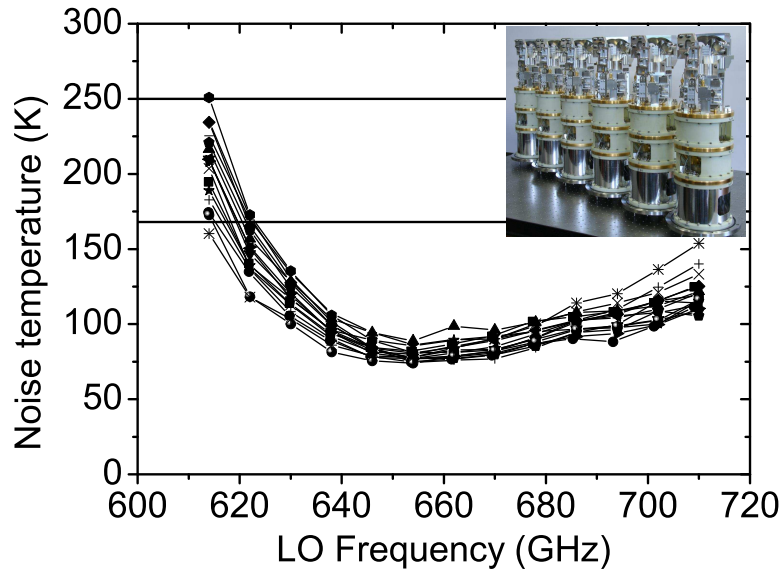


**Figure 8.1:** Uncorrected double sideband (DSB) noise temperature as a function of local oscillator (LO) frequency for 8 prototype cartridges of ALMA Band 9. Different symbols represent different cartridges and polarizations; all devices are based on Nb/AlO<sub>x</sub>/Nb SIS mixers. Specifications (full horizontal lines) of 80% of Band 9 below 168 K and below 250 K at all frequencies are met for all devices, in spite of a clear degradation of  $T_n$  at the lower end of the band. (Inset: six completed Band 9 cartridges in our laboratories.)

## 8.1 Introduction

In the superconducting technology of Band 9 (602 to 720 GHz) of the Atacama Large Millimeter Array (ALMA), we have chosen to work with the robust Nb SIS mixers and a Nb/SiO<sub>2</sub>/Nb tuning circuit. The latter is needed to match the antenna impedance ( $Z_{ant}$ ) to the SIS junction impedance [1], which is characterized by the junction's normal state resistance  $R_n$  in parallel with its capacitance  $C$ .

Although the specifications for Band 9 can be met with aluminum oxide tunnel barriers, an intrinsically wider band coverage would be beneficial. The noise temperature ( $T_n$ ) results for eight prototype Band 9 SIS mixers are shown in Fig. 8.1. The horizontal lines indicate the required and the hoped for noise temperatures. The results are obviously within the specifications. However, a flat response over the full band width is desirable. Also, the location of minimum noise temperature depends on unavoidable variations in the device-technology. High critical current density aluminum nitride devices have a low  $R_n C$  time constant, which would enable a desirable larger bandwidth, provided the matching circuit is not limiting [1].

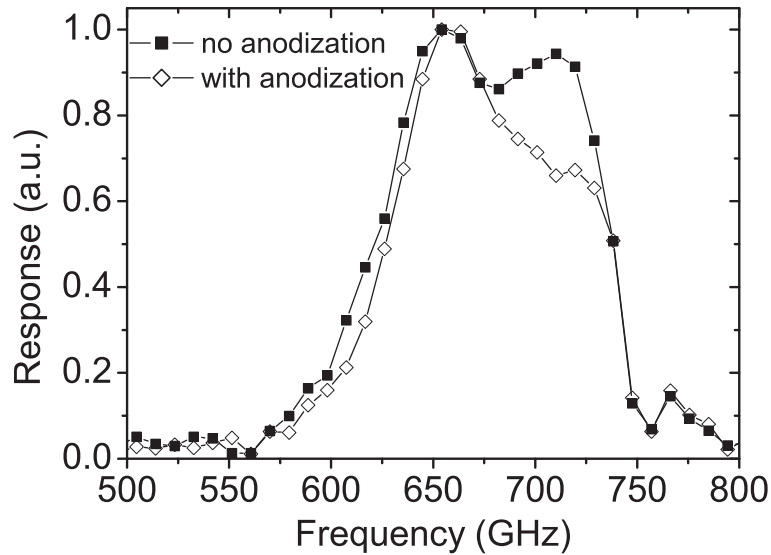


**Figure 8.2:** Effect of anodization on the frequency response of an SIS device. Normalized photoresponse of a device without anodization (full squares) and with anodization (open diamonds), measured with a Fourier Transform Spectrometer (FTS).

## 8.2 Properties of Nb microstriplines

For superconducting niobium with an energy gap  $2\Delta$  of 2.8 meV, the gap-frequency is 680 GHz. Hence, losses appear stronger in the range of Band 9, which is particularly important for the tuning circuit. This circuit, used to match  $Z_{ant}$  with the junction impedance, is realized with a Nb/SiO<sub>2</sub>/Nb microstripline. Information about the quality of the niobium is partially derived from the tunneling current-voltage ( $IV$ ) characteristics, but it does not provide information about the niobium on both sides of the dielectric. In particular,  $2\Delta$  and the normal conductivity  $\sigma_n$  are essential parameters in the evaluation of the frequency-dependent behavior of the microstripline. In our case, the bottom superconductor consists of a multilayer of 200 nm DC magnetron sputtered Nb, a 6 nm DC sputtered thin layer of Al, and the tunnel barrier (1 nm AlO<sub>x</sub> or AlN). For the completed microstripline, there is a 250 nm layer of RF sputtered SiO<sub>2</sub> and a top Nb layer of 500 nm.

The importance of the quality of the niobium of the microstriplines became more strongly apparent in a series of batches of Nb/AlO<sub>x</sub>/Nb SIS devices, in which a previously assumed innocent anodization step was added after the reactive ion etching process to define the junctions. Unfortunately, these devices showed a deteriorated performance at the higher frequency end, demonstrated in Fig. 8.2, although the DC  $IV$  characteristics revealed no sign of degraded niobium properties.

The anodization process, carried out up to a voltage of 10 V, leads to a full

oxidation of the Al layer, used to make the tunnel barrier. Consequently, the bottom Nb layer is also chemically reacting with oxygen atoms. As a result, the microstripline will be a multilayer of Nb/NbO<sub>y</sub>/AlO<sub>x</sub>/SiO<sub>2</sub>/Nb, where the index  $y$  may vary as a function of height. In other words, the dielectric has become a complicated package and the interface between the dielectric layer and the superconducting metal is quite different.

In tunneling experiments with anodized tunnel barriers it has been shown [2] that the energy gap of the Nb is lower than the bulk value. This finding is in line with the fact, known from tunnel junctions based on a standard niobium-oxidation process [3, 4] that the insulating niobium-oxide evolves into the niobium through a poorly conducting layer of suboxides of niobium, which become superconducting through the proximity-effect. Hence, it is justified to assume a lower  $2\Delta$  between 2.8 to 2.5 meV for the bottom Nb layer when we apply anodization in our processing. Note that this occurs without deterioration of the tunneling IV curve, because the Al and Nb layer below the junction area are not anodized.

Furthermore, it is known that the normal resistivity ( $\rho_n$ ) and critical temperature ( $T_c$ ) of NbO<sub>y</sub> depend strongly on  $y$  [5]. For  $y > 1$ ,  $\rho_n$  increases rapidly from 2  $\mu\Omega\text{cm}$  to 65  $\mu\Omega\text{cm}$  at  $y = 1.5$ . Over this range the  $T_c$  remains almost constant at about 1.4 K. Therefore, if anodization is used, and a layer of NbO<sub>y</sub> is created, the bottom layer of the microstripline is likely to have a much higher  $\rho_n$  (lower  $\sigma_n$ ).

A model that includes a lower  $\sigma_n$  and  $2\Delta$  for the bottom superconductor of the microstripline qualitatively explains the depressed FTS response for the anodized device in Fig. 8.2. We conclude that adding anodization to improve the edge-isolation of tunnel junctions may have a deteriorating effect on the microstriplines, which would in particular be harmful at frequencies around the gap-frequency of the superconductor. In addition, the microwave response of microstriplines built with a bilayer of niobium and aluminum does not necessarily comply with the standard Mattis-Bardeen theory. It has been shown, at the lower frequency of about 10 GHz, that for thick enough aluminum (tens of nanometers) the surface impedance of the Nb/Al bilayers does not agree with that of bare Nb samples [6]. It is to be expected that at higher frequencies similar deviations should already occur for thinner aluminum layers.

In the frequency range studied here the conclusion is that in evaluating the microstripline, the normal state conductivity and the energy gap of the top and bottom superconductors should be assumed to be different and dependent on the growth specifics and possibly the post-processing of the material.

### 8.3 Bandwidth of SIS mixers

Apart from the quality of the materials used for the microstripline and the position of the SIS device in the waveguide, determined by both the mounting of the

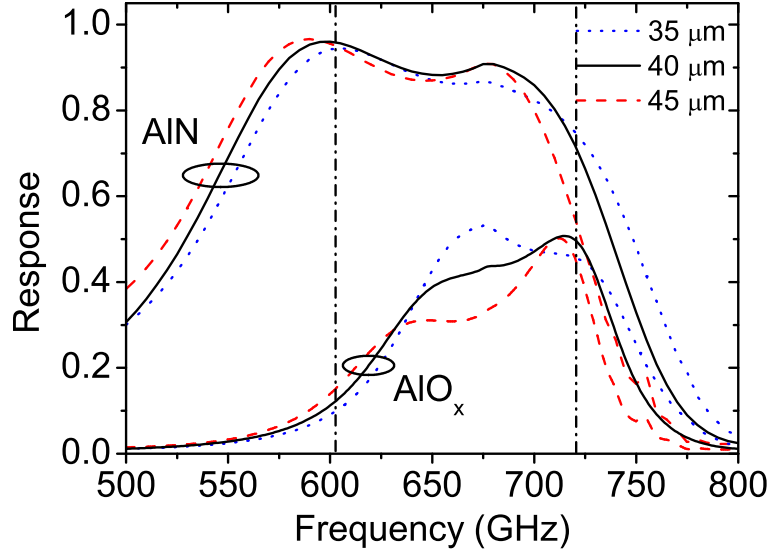


**Figure 8.3:** Substrate thickness dependence of the frequency response of SIS devices (calculated). Curves are for a substrate thickness of  $35 \mu\text{m}$  (dotted lines),  $40 \mu\text{m}$  (nominal, full lines), and  $45 \mu\text{m}$  (dashed lines). The curves for  $\text{AlO}_x$  and  $\text{AlN}$  tunnel barriers are indicated. The frequency range of ALMA Band 9 (602 to 720 GHz) is indicated with dash-dotted lines.

chip and the thickness of the substrate [1], the critical current density  $J_c$  of the tunnel barrier itself is the dominant parameter in the bandwidth.

The tunnel barrier defines the  $RC$  time constant, which limits the bandwidth of a device matched to a source impedance by [7]:

$$\ln\left(\frac{1}{\Gamma_{max}}\right) \Delta f = \frac{1}{2RC}, \quad (8.1)$$

where  $\Gamma_{max}$  is the maximum reflection coefficient over a bandwidth  $\Delta f$ . A wide  $\Delta f$  is achieved by a low  $RC$  product of the SIS junction, which in its turn is set by the tunnel barrier transparency. This transparency can be characterized by  $J_c$  [8]:

$$J_c = \frac{\pi}{2} \frac{\Delta}{eR_n A}, \quad (8.2)$$

with  $e$  the charge of an electron and  $A$  the area of the SIS junction.

Increasing the critical current density of  $\text{AlO}_x$  barriers leads to SIS junctions with poor quality  $IV$  characteristics for  $J_c$  above  $20 \text{ kA/cm}^2$  [9]. At this relatively low critical current density, or relatively high  $R_n A$  value the subgap current increases rapidly indicating that a substantial fraction of the tunnel barrier area carries higher order tunneling terms, i.e. contains parts with transmissivities close to unity.

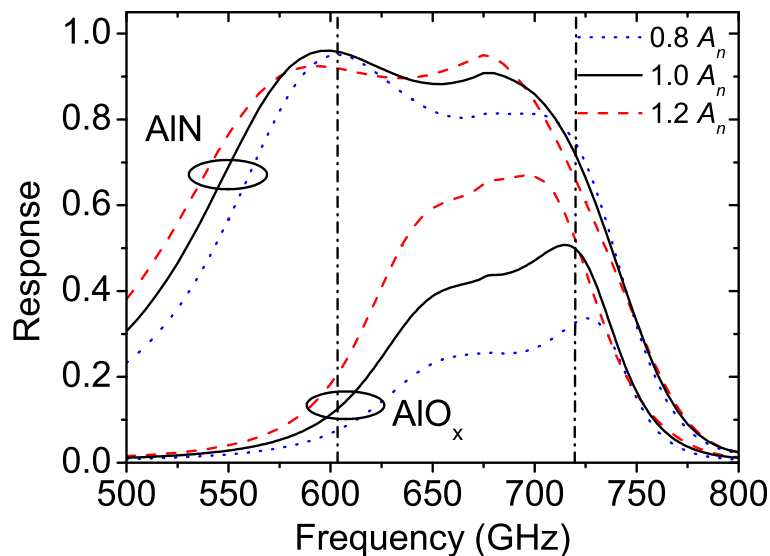


**Figure 8.4:** Junction area dependence of the frequency response of SIS devices (calculated). Curves are for a nominal junction area ( $A_n$ , full lines), a 20% reduced junction area (dotted lines), and a 20% increased junction area (dashed lines). For  $\text{AlO}_x$ , the  $A_n$  is  $1.0 \mu\text{m}^2$ , for  $\text{AlN}$ ,  $A_n$  is  $0.50 \mu\text{m}^2$ . The frequency range of ALMA Band 9 (602 to 720 GHz) is indicated with dash-dotted lines.

A route towards higher critical current densities, achieved by replacing  $\text{AlO}_x$  with  $\text{AlN}$ , was first identified by Shiota *et al.* [10] and subsequently explored by others [11], [12]. We have recently developed a technological route to  $\text{AlN}$  devices suitable for SIS mixers [13] using an ICP approach that was also described in [14] and identified that in comparison to  $\text{AlO}_x$  the  $\text{AlN}$  tunnel barriers have much more uniform tunneling properties. Mixing devices based on  $\text{AlN}$  barriers, using a different technological process, have recently been reported at frequencies from 275 to 425 GHz [15].

In order to test the sensitivity to variations in fabrication parameters, we have studied the transmission efficiency of SIS devices using a model reported before [1]. Unless indicated, we use the following parameters for our simulations:  $R_n A = 25 \Omega\mu\text{m}^2$ ,  $A = 1.0 \mu\text{m}^2$ , specific capacitance  $C_s = 65 \text{ fF}/\mu\text{m}^2$  for  $\text{AlO}_x$ , and  $R_n A = 6.0 \Omega\mu\text{m}^2$ ,  $A = 0.50 \mu\text{m}^2$ , and  $C_s = 60 \text{ fF}/\mu\text{m}^2$  for  $\text{AlN}$  tunnel barriers (see Section 8.4). The parameters of the microstripline are  $\sigma_{n,b} = 0.8 \times 10^7 \text{ S/m}$  for the bottom Nb and  $\sigma_{n,t} = 0.9 \times 10^7 \text{ S/m}$  for the top Nb, with the energy gaps set at the optimal value of 2.8 meV, unless indicated otherwise.

In Fig. 8.3, the influence of a variation of the substrate thickness is shown, for SIS junctions with an  $\text{AlO}_x$  and with an  $\text{AlN}$  tunnel barrier. Clearly, the substrate thickness plays an important role for the  $\text{AlO}_x$  devices, but has less an effect on the much wider bandwidth of the  $\text{AlN}$  devices.

Fig. 8.4 shows the calculated response for SIS junctions with variations in the

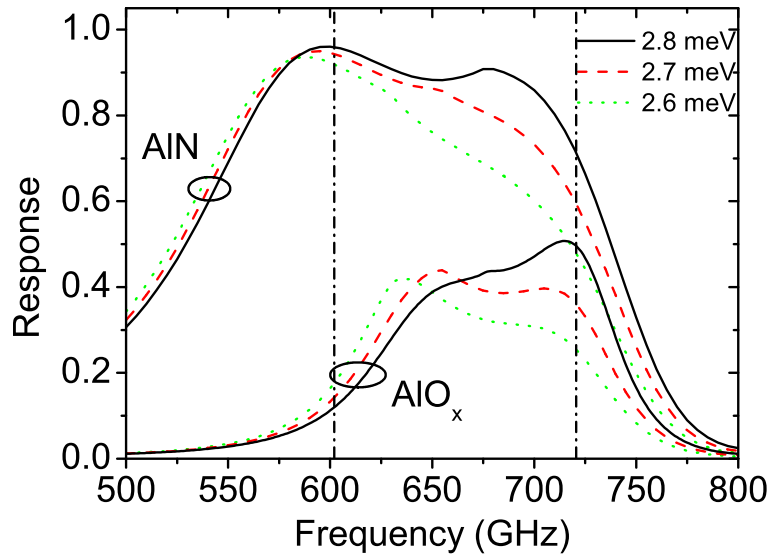


**Figure 8.5:** Microstripline energy gap dependence of the frequency response of SIS devices (calculated). Curves are for microstriplines for which both top and bottom superconductor have an equal  $2\Delta$  of 2.8 meV (full lines), a  $2\Delta$  of 2.7 meV (dashed lines), and a  $2\Delta$  of 2.6 meV (dotted lines). Calculations corresponding to  $\text{AlO}_x$  and  $\text{AlN}$  tunnel barriers are indicated. The frequency range of ALMA Band 9 (602 to 720 GHz) is indicated with dash-dotted lines.

area A. Whereas there is a sizable difference in response for the  $\text{AlO}_x$  devices, the bandwidth performance of  $\text{AlN}$  is hardly affected.

Finally, in Fig. 8.5, the dependence of the transmission efficiency on  $2\Delta$  is shown. Although the response of the  $\text{AlN}$  devices remains higher than that of the  $\text{AlO}_x$  devices, a degradation at the higher end of the band is clearly visible and undesirable. This indicates that despite the intrinsically wider bandwidth of  $\text{AlN}$  devices, it is crucial to maintain high quality niobium for the microstriplines.

## 8.4 Bandwidth evaluation

A set of SIS devices with a tuning circuit suitable for Band 9 of ALMA has been realized with  $\text{AlN}$  tunnel barriers, using our recently introduced method [13]. All devices contain a multisection  $\text{Nb}/\text{SiO}_2/\text{Al-Nb}$  microstripline, to tune out the capacitance of the SIS junction. The transmission efficiency of a device is evaluated using a Fourier Transform Spectrometer (FTS) by measuring the changes in the DC current produced by the incoming light for a bias voltage of 2.5 mV.

The device is mounted onto a waveguide backpiece. The device has the following parameters:  $R_n = 7.1 \Omega$ ,  $A = 0.52 \mu\text{m}^2$ , the ratio of the subgap resistance

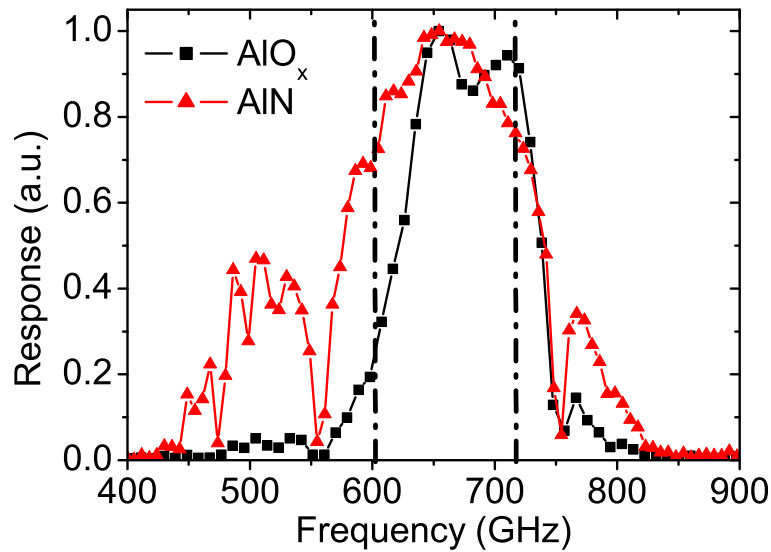


**Figure 8.6:** Normalized photoresponse of two devices, measured with an FTS. The triangles are for a device with an AlN tunnel barrier, whereas the squares show the best achievable result for a device with an AlO<sub>x</sub> tunnel barrier. The dash-dotted lines indicate ALMA Band 9. Minima in the response are due to water absorption.

to the normal resistance  $Q = 15$ , and the gap voltage  $V_g = 2.64$  mV.  $J_c$  for this device is  $56$  kA/cm<sup>2</sup>. The FTS data, taken at a temperature of  $4.2$  K, are shown in Fig. 8.6 (triangles). The FTS setup is operated in air, leading to the water absorption lines at the edges of the band. In the same graph, one of the best available FTS results for an AlO<sub>x</sub> based SIS device, selected for one of the prototype cartridges of Band 9, is shown (squares).

The full width half maximum (FWHM) bandwidth of the AlN device is about  $168$  GHz, whereas the FWHM bandwidth of the AlO<sub>x</sub> device is around  $116$  GHz. Obviously, the bandwidth of the AlN device is about  $45\%$  larger than that of the AlO<sub>x</sub> device. A good response is obtained over the full targeted band. In order to allow a fair comparison, care has been taken to position the devices in identical positions in the waveguide.

In Fig. 8.6, there are clearly minima in the response, due to the absorption of radiation by water vapor in the atmosphere, in particular at  $560$  and  $750$  GHz. In order to compare the FTS data with model calculations we subtract the atmospheric transmission from the data.<sup>i</sup> Fig. 8.7 shows the same FTS measurement results as Fig. 8.6 corrected for the atmospheric transmission [16]. The triangles show the corrected response for the AlN device, the squares indicate the corrected response for the AlO<sub>x</sub> device. The full line is the model fit for the AlN

<sup>i</sup>Note that this approach differs from the method described in Section 6.4, where the *modeling* includes the atmospheric transmission. Here, the *data* are modified to subtract the effect of the atmosphere.

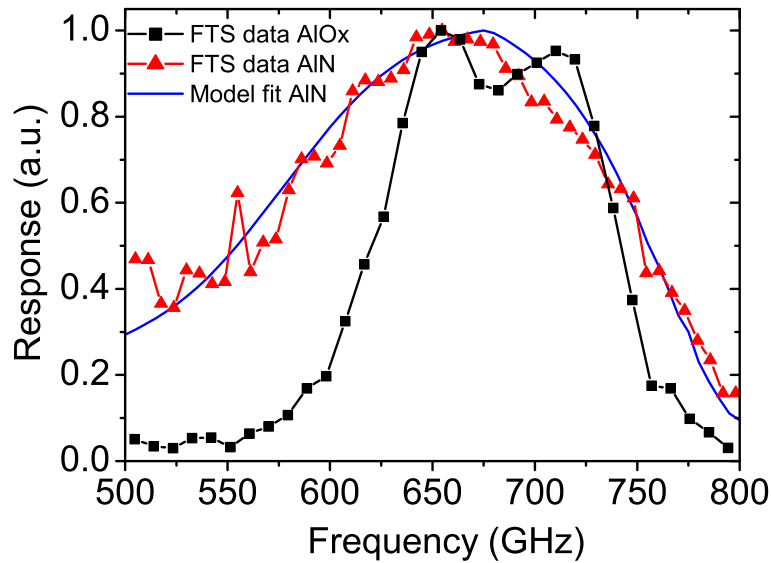


**Figure 8.7:** FTS measurement results, corrected for the atmospheric transmission. The triangles are for an AlN device, the squares for an AlO<sub>x</sub> device. The full line shows the simulated response for the AlN device, using real device parameters. All curves are normalized to their maximum.

device, based on its measured device parameters. The specific capacitance of the SIS junction, used as a fitting parameter, is determined to be  $60 \text{ fF}/\mu\text{m}^2$ . Based on a permittivity of AlN of 8.8 [17], this corresponds to a tunnel barrier thickness of 1.3 nm, which is well within the tolerance of the Transmission Electron Microscope analysis in [13], which yields  $1.5 \pm 0.5 \text{ nm}$ .

From Fig. 8.7, we can correct the FWHM bandwidth for water absorption. The AlN device has a bandwidth of 187 GHz, the AlO<sub>x</sub> device yields 122 GHz. Hence, the use of AlN has improved the bandwidth by 53 %.

## 8.5 Noise temperature

The same AlN based device has been mounted in a standard ALMA Band 9 test cartridge. The noise temperature of the mixer, the accompanying optics and the Intermediate Frequency (IF) chain [18] has been evaluated using the standard Y-factor method. The resulting uncorrected DSB noise temperatures at different local oscillator (LO) frequencies are presented in Fig. 8.8 (triangles pointing upwards). In the same graph, the average of the 16 traces for the prototype cartridges in Fig. 8.1, obtained with AlO<sub>x</sub> based SIS devices, are shown with squares. AlN results reported earlier, based on an unoptimized tuning circuit [19] are indicated by the triangles pointing downwards.

For the AlO<sub>x</sub> devices, the minimum noise temperature is 79.5 K and the

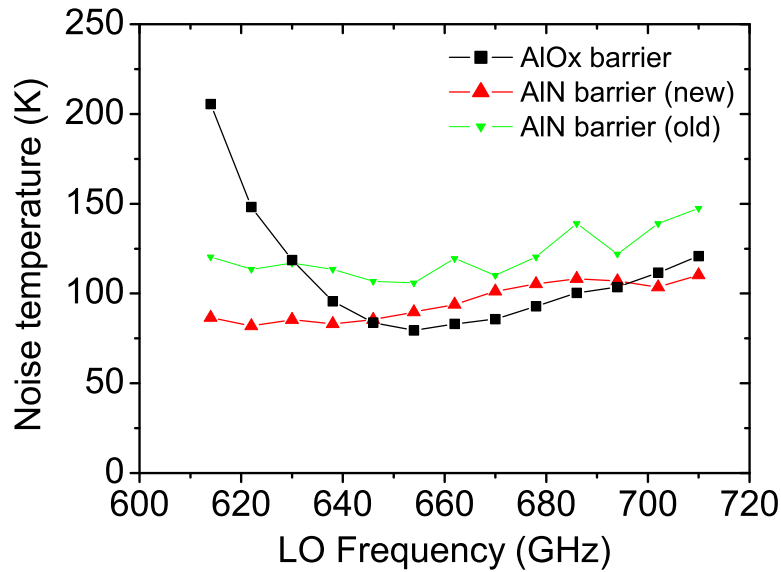


**Figure 8.8:** Uncorrected DSB noise temperature of an SIS mixer with an AlN tunnel barrier (triangles pointing up), earlier AlN results [19] (triangles pointing down) and the average of the traces of Fig. 8.1, for an SIS with an AlO<sub>x</sub> tunnel barrier (squares), in the frequency range of ALMA Band 9.

average over the full band is 110 K. On the other hand, the newest AlN devices have a minimum noise temperature of 82.0 K, whereas the average over Band 9 is 96 K.

Evidently, the noise temperature of the newest AlN SIS mixers is much flatter over the full ALMA Band 9 than for the best AlO<sub>x</sub> mixers, while practically maintaining the same low value.

## 8.6 Conclusion

The optimal astronomical use of the Band 9 frequency window of the Atacama Large Millimeter Array is dependent on a few material parameters of the superconducting mixing devices. We find that the energy gaps of the bottom and the top superconductor of tuning microstriplines, which can not be inferred from DC SIS measurements, are dependent on the process route and may limit the band coverage. The normal conductivity of these superconducting layers is determined by the fabrication process as well, and is in general different for the top and the bottom layer. The use of an anodization step in the processing will deteriorate the performance of the tuning microstriplines, due to a degradation in  $\sigma_n$  and  $2\Delta$ .

The use of AlN tunnel barriers in SIS devices leads to a sizable gain in the FWHM bandwidth, which, after correction for the atmospheric transmission,

amounts to about 53 % in comparison to  $\text{AlO}_x$  devices. Heterodyne measurements reveal that the AlN SIS devices have an uncorrected DSB noise temperature which is comparably low at the optimum frequency, but much lower than the  $\text{AlO}_x$  mixers currently in the prototype Band 9 cartridges at the other frequencies of the band.

## 8.7 Final remarks

In this Thesis, a large part of the research has been dedicated to establishing a model that can reliably predict the frequency response of an SIS junction with tuning microstriplines. In order to achieve maximum transparency about the material parameters that should be used, we tabulate them below. The parameters have been found by critical analysis of the physical processes characteristic for the high frequency response, as described in Sections 6.3 and 8.2.

It should be noted that the parameters quoted here apply to the devices processed in this research, and are therefore not necessarily universal. Instead, each change (or difference) in the fabrication procedure should lead to a careful re-analysis of the relevant material parameters.

Parameter	Value
Gap energy bottom superconductor (Nb)	2.8 meV
Gap energy top superconductor (Nb)	2.8 meV
Normal conductivity bottom superconductor (Nb)	$0.8 \times 10^7$ S/m
Normal conductivity top superconductor (Nb)	$0.9 \times 10^7$ S/m
Specific capacitance $\text{AlO}_x$	65 fF/ $\mu\text{m}^2$
Specific capacitance AlN	60 fF/ $\mu\text{m}^2$
Normal resistance times area $\text{AlO}_x$ (typical range)	20-30 $\Omega\mu\text{m}^2$
Normal resistance times area AlN (typical range)	2-10 $\Omega\mu\text{m}^2$
Dielectric constant $\text{SiO}_2$	3.8

## References

- [1] C. F. J. Lodewijk, O. Noroozian, D. N. Loudkov, T. Zijlstra, A. M. Baryshev, F. P. Mena, and T. M. Klapwijk, "Optimizing superconducting matching circuits for Nb SIS mixers operating around the ap frequency," *IEEE Trans. Appl. Superconductivity*, Vol. **17**, 375 (2007). *Note: this reference corresponds to Chapter 6.*
- [2] J. Aponte, E. Rivera, A. Sa Neto, and M. Octavio, "Anodized niobium as barrier for Josephson tunnel junctions," *J. Appl Phys.*, Vol. **62**, 700 (1987).
- [3] G. B. Arnold, J. Zasadzinski, and E. L. Wolf, "A resolution of the controversy on tunneling in Nb," *Phys. Lett. A*, Vol. **69**, 136 (1978).

- [4] J. M. Rowell, M. Gurvitch, and J. Geerk, "Modification of tunneling barriers on Nb by a few monolayers of Al," *Phys. Rev. B*, Vol. **24**, 2278 (1981).
- [5] J. K. Hulm, C. K. Jones, R. A. Hein, and J. W. Gibson, "Superconductivity in the TiO and NbO systems," *J. Low Temp. Phys.*, Vol. **7**, 291 (1972).
- [6] M. S. Pambianchi, S. N. Mao, and S. M. Anlage, "Microwave surface impedance of proximity-coupled Nb/Al bilayer films," *Phys. Rev. B*, Vol. **52**, 4477 (1995).
- [7] H. W. Bode, *Network analysis and feedback amplifier design*, New York, USA: Van Nostrand, Sec. 16.3 (1945).
- [8] V. Ambegaokar and A. Baratoff, "Tunneling between superconductors," *Phys. Rev. Lett.*, Vol. **10**, 486 (1963).
- [9] R. E. Miller, W. H. Mallison, A. W. Kleinsasser, K. A. Delin, and E. M. Macedo, "Niobium trilayer Josephson tunnel junctions with ultrahigh critical current densities," *Appl. Phys. Lett.*, Vol. **63**, 1423 (1993).
- [10] T. Shiota, T. Imamura, and S. Hasuo, "Nb Josephson junction with an AlN<sub>x</sub> barrier made by plasma nitridation," *Appl. Phys. Lett.*, Vol. **61**, 1228 (1992).
- [11] A. W. Kleinsasser, W. H. Mallison, and R. E. Miller, "Nb/AlN/Nb Josephson junctions with high critical current density," *IEEE Trans. Appl. Superconductivity*, vol. 5, 2318 (1995).
- [12] B. Bumble, H. G. LeDuc, J. A. Stern, and K. G. Megerian, "Fabrication of Nb/Al-N<sub>x</sub>/NbTiN junctions for SIS mixer applications," *IEEE Trans. Appl. Superconductivity*, vol. 11, 76 (2001).
- [13] T. Zijlstra, C. F. J. Lodewijk, N. Vercreyssen, F. D. Tichelaar, D. N. Loudkov, and T. M. Klapwijk, "Epitaxial aluminum nitride tunnel barriers grown by nitridation with a plasma source," *Appl. Phys. Lett.*, Vol. **91**, 233102 (2007). *Note: this reference corresponds to Chapter 7.*
- [14] T. W. Cecil, R. M. Weikle, A. R. Kerr, and A. W. Lichtenberger, "Investigation of NbTiN thin films and AlN tunnel barriers with ellipsometry for superconducting device applications," *IEEE Trans. Appl. Superconductivity*, vol. 17, 3525 (2007).
- [15] J. W. Kooi, A. Kovcs, M. C. Sumner, G. Chattopadhyay, R. Ceria, D. Miller, B. Bumble, H. G. LeDuc, J. A. Stern, and T. G. Phillips, "A 275-425-GHz tunerless waveguide receiver based on AlN-barrier SIS technology," *IEEE Trans. Microwave Theory and Techn.*, Vol. **55**, 2086 (2007).
- [16] The program that calculates the atmospheric transmission has been provided by J. R. Pardo-Carrion, Departamento de Astrofísica Molecular e Infraroja, Consejo Superior de Investigaciones Científicas, Madrid, Spain.
- [17] L. M. Sheppard, "Aluminum nitride: a versatile but challenging material," *Am. Ceram. Soc. Bull.*, Vol. **69**, 1801 (1990).

- 
- [18] A. Baryshev, E. Lauria, R. Hesper, T. Zijlstra, and W. Wild, “Fixed-tuned waveguide 0.6 THz SIS Mixer with Wide band IF,” ALMA memo 429 (2002).
  - [19] C. F. J. Lodewijk, T. Zijlstra, D. N. Loudkov, T. M. Klapwijk, F. P. Mena, and A. M. Baryshev, “Wideband AlN-based SIS devices for frequencies around 700 GHz,” in Proc. 18th Int. Symp. on Space THz Technology, Ed. A. Karpov, paper 10-1, 256 (2007).



# Summary

## Bandwidth coverage of niobium based superconducting tunnel devices

Mankind has always been intrigued by the origin of the universe we live in. To gather more knowledge about this origin, many interesting things can be learnt from the observation of stars in the sub-millimeter part of the electromagnetic spectrum. The presence of characteristic molecules unveils the evolution of the early universe and the formation of stars and planetary systems. The Atacama Large Millimeter/submillimeter Array is being built to take a big step forward in the many questions there are. It will consist of up to 80 telescopes with heterodyne receivers in the frequency range of 30 to 950 GHz, placed in a Chilean desert on a 5000 m altitude plateau to minimize the absorption of astronomical signals by the atmosphere. In this Thesis, research is described that has been done to develop superconductor - insulator - superconductor (SIS) junctions for Band 9 of ALMA, which runs from 602 to 720 GHz. For heterodyne detection in this frequency range, SIS detectors are the most sensitive.

An SIS junction consists of two superconducting electrodes, separated by an insulating tunnel barrier. Superconductivity is characterized by the absence of electrical resistance under certain conditions, like a temperature below the critical temperature ( $T_c$ ), and can be explained by the pairing of electrons into one macroscopic quantum ground state, due to an increased electron-phonon interaction. A perturbation, for example a bias voltage or an electromagnetic wave, can create excitations from the ground state in the form of quasiparticles, if its energy is larger than the superconducting energy gap  $2\Delta$ . For an SIS junction, if a magnetic field is applied to suppress the effect of tunneling Cooper pairs, the current-voltage response is characterized by a strong non-linearity at the onset of quasiparticle-tunneling. If an SIS junction is used as a heterodyne mixer, this non-linearity is exploited to downconvert high frequency signals to a lower intermediate frequency (IF) by mixing them with a known local oscillator (LO) signal. Thus, a high frequency signal can be detected.

In Chapter 3, it is explained that Band 9 has been chosen because of the large scientific potential (and the possibility of ‘early science’) for the Dutch astronomical community, as well as the large experience in the development of SIS mixers for this frequency range in the consortium of Delft University of

Technology and SRON Netherlands Institute for Space Research.

Further, the two main requirements for ALMA Band 9 relevant for this research, the bandwidth and the noise temperature, are analyzed. The specification for the bandwidth is determined by the atmospheric transmission at the site of ALMA, characterized by the absorption of radiation at certain frequencies, mainly due to the presence of water molecules. To meet the bandwidth requirement, SIS junctions need to have a low resistance times area ( $RC$ ) time, which corresponds to having a high critical current density. The specification for the noise temperature is determined by the general ALMA requirement to obtain a sub-milliJansky flux density sensitivity within 10 minutes integration time. To meet this requirement, SIS devices have to be optimized by increasing the transmission of the signal and reducing the noise. The transmission of the signal is increased by proper design of the antenna and the tuning circuit, and by the realization of SIS junctions with a high responsivity. The noise is decreased by minimizing the losses in the tuning circuit and reducing the noise added by the SIS junction, for example due to multiple Andreev reflections (MAR).

Chapter 4 describes the SIS devices used in this research. After a description of the layout, the choice of the different materials is motivated: the substrate is made of fused quartz, the junctions consist at first of niobium - aluminum oxide - niobium (Nb/ $\text{AlO}_x$ /Nb), but are replaced by niobium - aluminum nitride (AlN) - niobium in this research, the microstriplines are made of niobium - silicon dioxide ( $\text{SiO}_2$ ) - niobium, and the contact pads are made of gold. For the microstriplines, the RF normal conductivity of the top layer of Nb deviates from the DC normal conductivity because of a degraded quality of the Nb on top of the  $\text{SiO}_2$ . In Chapter 8, it is explained that also the bottom layer of Nb can have a lower RF normal conductivity. Further in Chapter 4, the possibilities of using other materials than the ones in this research are explored. Finally, the process to realize SIS devices is described in detail.

In Chapter 5, we focus on the tunneling barrier of SIS junctions. In order to obtain wide bandwidth SIS junctions, it is important to have transparent tunnel barriers, with a high critical current density. If a tunnel barrier becomes more transparent, the effect of non-uniformity becomes more apparent. Due to non-uniformity, there will be more locations with a transmissivity close to 1, permitting a higher probability of higher-order tunneling processes due to MAR. These processes cause the emergence of higher a subgap current through the junctions, in other words a lower quality factor and a reduced performance of the SIS as a heterodyne mixer.

To achieve a higher transparency while maintaining a high quality, there have been studies to replace the commonly used tunnel barrier  $\text{AlO}_x$  with different materials, like MgO and AlN, but they were never created with a reliable process. After a summary of past work on AlN tunnel barriers, we introduce in Section 5.2 our newly developed process to grow AlN tunnel barriers. In contrast with others, we use a nitrogen plasma in the afterglow region of an inductively coupled plasma

source, at relatively high pressures, to reduce the ion energies in the plasma and thus the damage to the tunnel barrier. We find a very reproducible process, with good quality SIS junctions up to high critical current densities.

In Chapter 6, we analyze the performance of Nb/ $\text{AlO}_x$ /Nb SIS junctions with tuning circuits as heterodyne detectors for ALMA Band 9. We measure the bandwidth coverage with a Fourier Transform Spectrometer (FTS) and find a large spread in the response. We describe a theoretical model to simulate the transmission efficiency of the SIS devices, and we find that the RF normal conductivity of the Nb layer on top of the  $\text{SiO}_2$  is about  $1.0 \times 10^7$  S/m, supported by conductivity measurements of Nb films with varying thickness and by transmission electron microscope (TEM) images. We use the model to optimize the geometry of the tuning microstriplines. We measure the response of optimized devices, and still find a large variation. Also, noise temperature measurements show for the majority of the relevant frequency band no improvement over non-optimized devices. We conclude that, to improve the band-coverage significantly, SIS junctions with a high critical current density (realized with AlN tunnel barriers) should be used.

Chapter 7 reports on the development of a new method to grow these high critical current density AlN tunnel barriers. Using a remote nitrogen plasma from an inductively coupled plasma source at high pressures, a much better reproducibility and control is found compared to previous work. From DC tunneling characteristics and cross-sectional TEM images, it is concluded that, compared to the commonly used  $\text{AlO}_x$  barriers, the AlN barriers are much more uniform in transmissivity, leading to a better quality at high critical current densities. The TEM images indicate an epitaxial alignment of the AlN lattice planes, which may be the cause for the better uniformity.

Finally, in Chapter 8, we study the application of AlN tunnel barriers grown with the newly developed method in SIS mixers for ALMA Band 9, and compare their behavior both in simulation and experiment with  $\text{AlO}_x$  based SIS junctions. We find that microstriplines of Nb/ $\text{SiO}_2$ /Nb have different properties for top and bottom superconductor, depending on the fabrication process. With FTS measurements, we find that the bandwidth of SIS devices increases by 53 % if the  $\text{AlO}_x$  tunnel barrier is replaced by AlN, demonstrating that the bandwidth is no longer limited by the the tuning circuit or the SIS junction, but by the atmospheric absorption of radiation. Using AlN, a noise temperature is obtained which is as low as the best  $\text{AlO}_x$  noise temperatures, but much flatter over the targeted band.

SIS devices that have been developed in the research of this Thesis are currently being used in the Carbon Heterodyne Array of the Max Planck Institute (CHAMP+), an astronomical instrument on the Atacama Pathfinder Experiment (APEX) telescope in Chile, near the location of ALMA. Further, the first eight prototype cartridges for ALMA Band 9 are equipped with  $\text{AlO}_x$  SIS devices realized in this research. SRON and Delft University of Technology have been contracted to build the remaining 72 cartridges, which will be upgraded with AlN

SIS mixers, developed in the research of this Thesis, thereby greatly enhancing the performance of the ALMA instrument.

Chris Lodewijk  
Delft, December 2008

# Samenvatting

## Bandbreedte van niobium supergeleidende tunneljuncties

De mens is altijd al geïntrigeerd geweest door de oorsprong van het universum. Om meer over deze oorsprong te weten te komen, kunnen we vele interessante dingen leren door de observatie van sterren en planeten in het sub-millimeter deel van het elektromagnetische spectrum. De aanwezigheid van karakteristieke moleculen vertelt ons meer over hoe het vroege universum zich heeft geëvolueerd en hoe sterren en planeten zijn ontstaan. De Atacama Large Millimeter/submillimeter Array (ALMA) wordt gebouwd om een grote stap voorwaarts te nemen in de vele vragen die er bestaan. ALMA zal bestaan uit maximaal 80 schotelantennes met heterodyne ontvangers in het frequentiegebied van 30 tot 950 GHz. Deze antennes komen in een Chileense woestijn te staan op een hoogte van circa 5000 m, om de absorptie van astronomische signalen door de atmosfeer te minimaliseren. In dit proefschrift wordt het onderzoek beschreven dat gedaan is om supergeleider - isolator - supergeleider (SIS) juncties te ontwikkelen voor Band 9 van ALMA, die loopt van 602 tot 720 GHz. SIS juncties zijn de gevoeligste heterodyne detectoren voor dit frequentiegebied.

Een SIS junctie bestaat uit twee supergeleidende elektrodes, die worden gescheiden door een isolerende tunnelbarrière. Karakteristiek voor supergeleiding is de afwezigheid van elektrische weerstand onder bepaalde omstandigheden, waaronder een temperatuur onder de kritische temperatuur ( $T_c$ ). Supergeleiding ontstaat doordat een verhoogde elektron-fonon interactie ervoor zorgt dat elektronen paren vormen, genaamd Cooper paren, die op hun beurt één macroscopische, quantummechanische grondtoestand vormen. Een verstoring van die grondtoestand, bijvoorbeeld een bias spanning of een elektromagnetische golf, kan excitaties vanuit de grondtoestand creëren in de vorm van quasideeltjes, als de energie van de verstoring groter is dan de supergeleidende energie  $2\Delta$ . Wanneer een magnetisch veld wordt gebruikt om het effect van tunnelende Cooper paren te onderdrukken, heeft de stroom-spanning karakteristiek van een SIS junctie een sterke niet-lineariteit bij de inschakeling van het tunnelen van quasideeltjes. Wanneer een SIS junctie als een heterodyne mixer wordt gebruikt, wordt deze niet-lineariteit gebruikt om signalen met een hoge frequentie te converteren naar signalen met een lagere frequentie, de intermediaire frequentie (IF), door ze te mixen met een bekend signaal van een lokale oscillator (LO). Op deze manier kan

een signaal met een hoge frequentie worden gedetecteerd.

In Hoofdstuk 3 wordt uitgelegd dat Band 9 is gekozen vanwege de grote wetenschappelijke potentie (en de mogelijkheid van ‘vroeg wetenschap’) voor de Nederlandse astronomische gemeenschap, en vanwege de grote ervaring in het ontwikkelen van SIS mixers die er bestaat in het consortium van de Technische Universiteit Delft en het SRON Nederlands Instituut voor Ruimte Onderzoek.

Verder worden de twee belangrijkste eisen voor ALMA Band 9 geanalyseerd die relevant zijn voor dit onderzoek: de bandbreedte en de ruistemperatuur. De specificatie voor de bandbreedte wordt bepaald door de atmosferische transmissie ter hoogte van ALMA, gekarakteriseerd door de absorptie van straling bij bepaalde frequenties, voornamelijk door de aanwezigheid van watermoleculen. Om aan de bandbreedte-eis te voldoen, moeten SIS juncties een lage weerstand maal capaciteit ( $RC$ ) tijd hebben, wat overeenkomt met een hoge kritische stroomdichtheid. De specificatie voor de ruistemperatuur wordt bepaald door de algemene ALMA eis om een sub-milliJansky flux dichtheid gevoeligheid te bereiken binnen 10 minuten integratietijd. Om aan deze eis te voldoen, moeten de SIS detectoren worden geoptimaliseerd door de transmissie van het signaal te vergroten en de ruis te onderdrukken. De transmissie van het signaal wordt groter wanneer er een passend ontwerp van de antenne en het afstemmingscircuit is, en SIS juncties met een grote gevoeligheid. De ruis kan worden onderdrukt door de verliezen in het afstemmingscircuit te minimaliseren en door te zorgen dat er geen extra ruis wordt toegevoegd door de SIS junctie, bijvoorbeeld door meervoudige Andreev reflecties (MAR).

Hoofdstuk 4 beschrijft de SIS detectoren die in dit onderzoek zijn gebruikt. Na een feitelijke omschrijving van de opbouw van de detectoren, worden de keuzes voor de verschillende materialen gemotiveerd: het substraat is gemaakt van kwarts, de juncties bestaan uit niobium - aluminium oxide - niobium ( $Nb/AlO_x/Nb$ ), later vervangen door niobium - aluminium nitride ( $AlN$ ) - niobium, de microstriplijnen bestaan uit niobium - silicium dioxide ( $SiO_2$ ) - niobium en de contactvlakken zijn gemaakt van goud. Voor de microstriplijnen wijkt de RF (hoge frequentie) normale geleidbaarheid van de bovenste laag Nb af van de DC (gelijkstroom) normale geleidbaarheid, omdat de kwaliteit van het Nb minder is op het  $SiO_2$ . In hoofdstuk 8 wordt uitgelegd dat ook de onderste laag Nb een lagere RF normale geleidbaarheid kan hebben. In het vervolg van hoofdstuk 4 worden de mogelijkheden onderzocht om andere materialen dan in dit onderzoek te gebruiken. Tenslotte wordt het proces om SIS detectoren te realiseren in detail beschreven.

In Hoofdstuk 5 verleggen we de aandacht naar de tunnelbarrière van SIS juncties. Om SIS juncties met een grote bandbreedte te verkrijgen, is het belangrijk om transparante tunnelbarrières hebben, met een grote kritische stroomdichtheid. Als een tunnelbarrière transparanter wordt, wordt het effect van niet-uniformiteit beter waarneembaar. Immers, vanwege de niet-uniformiteit zullen er meer plaatsen zijn met een transmissiecoëfficiënt dichtbij 1, waardoor de kans op hogere

orde tunnelprocessen (door middel van MAR) groter wordt. Deze processen veroorzaken dan weer een hogere stroom door de juncties bij spanningen beneden de supergeleidende energie (subgap stroom), met andere woorden een lagere kwaliteitsfactor en een mindere prestatie van de SIS als een heterodyne mixer.

Er zijn studies geweest om een hogere transparantie te bereiken zonder vermindering van de kwaliteitsfactor van de SIS junctie. In deze studies heeft men de gebruikelijke tunnelbarrière  $\text{AlO}_x$  vervangen door andere materialen, zoals magnesium oxide ( $\text{MgO}$ ) en aluminium nitride ( $\text{AlN}$ ), maar nooit werd er een betrouwbaar proces gevonden. Na een samenvatting van verleden werk met  $\text{AlN}$  tunnelbarrières, introduceren we in Paragraaf 5.2 ons nieuw ontwikkelde proces om  $\text{AlN}$  tunnelbarrières te groeien. In tegenstelling tot anderen, gebruiken wij een stikstof plasma in het nagloeingsgebied van een inductief gekoppelde plasmabron, bij een relatief hoge druk om de ionenenergie in het plasma te verminderen en zo de schade aan de tunnelbarrière te beperken. We vinden een zeer reproduceerbaar proces, dat goede kwaliteit SIS juncties oplevert tot en met hoge kritische stroomdichtheden.

In Hoofdstuk 6 analyseren we hoe  $\text{Nb}/\text{AlO}_x/\text{Nb}$  SIS juncties met een afstemschakeling presteren als heterodyne detectoren voor ALMA Band 9. We meten de bandbedekking met een Fourier Transformatie Spectrometer (FTS) en vinden een grote spreiding in de respons. We beschrijven een theoretisch model om de transmissie efficiëntie van de SIS detectoren te simuleren, en we vinden dat de RF normale geleidbaarheid van de Nb laag bovenop het  $\text{SiO}_2$  ongeveer  $1 \times 10^7$  S/m is, onderbouwd door geleidbaarheidsmetingen van Nb films met een verschillende diktes en door transmissie elektronen microscoop (TEM) beelden. We gebruiken het model om de geometrie van de microstriplijnen te optimaliseren. Wanneer we de respons van geoptimaliseerde detectoren meten, vinden we nog steeds een grote spreiding. Verder laten ruistemperatuur metingen voor het grootste deel van de relevante band geen verbetering zien ten opzichte van niet-geoptimaliseerde detectoren. We concluderen dat er SIS juncties met een hoge kritische stroomdichtheid (gerealiseerd met  $\text{AlN}$  tunnelbarrières) gebruikt moeten worden om de bandbreedte significant te verbeteren.

Hoofdstuk 7 rapporteert over de ontwikkeling van een nieuwe methode om zulke  $\text{AlN}$  tunnelbarrières met een hoge kritische stroomdichtheid te groeien. Door een plasma te gebruiken van een inductief gekoppelde plasmabron bij een hoge druk, wordt een veel betere reproduceerbaarheid en controleerbaarheid gevonden dan in eerder werk. Uit DC tunnelkarakteristieken en TEM afbeeldingen van de dwarsdoorsnede wordt geconcludeerd dat, vergeleken met de gewoonlijk gebruikte  $\text{AlO}_x$  tunnelbarrières, de  $\text{AlN}$  barrières een veel uniformere transmissiecoëfficiënt hebben, wat leidt tot een betere kwaliteit bij hoge kritische stroomdichtheden. De TEM beelden tonen een epitaxiale uitlijning van de  $\text{AlN}$  roostervlakken, wat de reden kan zijn voor de betere uniformiteit.

In Hoofdstuk 8 tenslotte bestuderen we de toepassing van  $\text{AlN}$  tunnelbarrières die gegroeid zijn met de nieuw ontwikkelde methode in SIS mixers voor ALMA

Band 9, en vergelijken we hun gedrag zowel in simulatie als in experiment met op  $\text{AlO}_x$  gebaseerde SIS juncties. We vinden dat Nb/ $\text{SiO}_2$ /Nb microstriplijnen verschillende eigenschappen hebben voor de onderste en bovenste supergeleider, afhankelijk van het fabricage proces. Met FTS metingen vinden we dat de bandbreedte van SIS detectoren met 53 % toeneemt als de  $\text{AlO}_x$  tunnelbarrière wordt vervangen door AlN. Tevens laten deze metingen zien dat de bandbreedte niet langer wordt beperkt door het afstemcircuit of de SIS junctie, maar door de atmosferische absorptie van straling. Met AlN wordt een ruistemperatuur bereikt die even laag is als de beste  $\text{AlO}_x$  ruistemperaturen, maar veel vlakker over de bedoelde frequentieband.

SIS detectoren die ontwikkeld zijn voor het onderzoek van dit proefschrift worden momenteel gebruikt in het Carbon Heterodyne Array of the Max Planck Institute (CHAMP+), een astronomisch instrument op de Atacama Pathfinder Experiment (APEX) telescoop in Chili, in de buurt van de locatie van ALMA. Verder zijn de eerste acht prototype ‘cartridges’ voor Band 9 uitgerust met  $\text{AlO}_x$  SIS detectoren die voor dit onderzoek zijn gerealiseerd. SRON en de Technische Universiteit Delft zijn gecontracteerd om ook de overige 72 cartridges te bouwen. Deze zullen worden vernieuwd met de AlN SIS mixers die ontwikkeld zijn in het onderzoek van dit proefschrift, waardoor de prestaties van het ALMA instrument enorm zullen verbeteren.

Chris Lodewijk  
Delft, december 2008

# Curriculum Vitae

Chris Franciscus Jessica Lodewijk

- 19-11-1979      Born in Hulst, the Netherlands
- 1992-1998      Grammar school  
Reynaert College, Hulst, the Netherlands
- 1998-2004      M. Sc. in Applied Physics  
Delft University of Technology, the Netherlands  
Graduate research at Quantum Transport group  
under supervision of Prof. dr. ir. L. P. Kouwenhoven  
Subject: *Transport in short segments of carbon nanotubes  
with electrodes fabricated by electromigration*  
Received scholarship for highly promising first year  
students (“Sterbeurs”, Delft University of Technology, 1998)
- 2004-2008      Ph. D. research  
Delft University of Technology, the Netherlands  
Supervision of Prof. dr. ir. T. M. Klapwijk  
Subject: *Bandwidth coverage of niobium based  
superconducting tunnel devices*
- 2008-present    Experimental physicist  
MAPPER Lithography, Delft, The Netherlands  
Research into detection and removal of contamination  
in electron beam lithography systems



## List of refereed publications

1. F. P. Mena, J. W. Kooi, A. M. Baryshev, C. F. J. Lodewijk, R. Hesper, G. Gerlofsma, T. M. Klapwijk, and W. Wild  
*A sideband-separating heterodyne receiver for the 600-720 GHz band*  
Submitted to IEEE Transactions on Microwave Theory and Techniques (2008).
2. C. F. J. Lodewijk, T. Zijlstra, S. Zhu, F. P. Mena, A. M. Baryshev, and T. M. Klapwijk  
*Bandwidth limitations of Nb/AlN/Nb SIS mixers around 700 GHz*  
Submitted to IEEE Transactions on Applied Superconductivity (2008).
3. F. P. Mena, J. W. Kooi, A. M. Baryshev, C. F. J. Lodewijk, R. Hesper, W. Wild, and T. M. Klapwijk  
*An SIS-based sideband-separating heterodyne mixer optimized for the 600 to 720 GHz band*  
Journal of Physics: Conference series, Vol. **97**, 012331 (2008).
4. T. Zijlstra, C. F. J. Lodewijk, N. Vercruyssen, F. D. Tichelaar, D. N. Loudkov, and T. M. Klapwijk  
*Epitaxial aluminum-nitride tunnel barriers grown by nitradation with a plasma source*  
Applied Physics Letters, Vol. **91**, 233102 (2007).
5. C. F. J. Lodewijk, O. Noroozian, D. N. Loudkov, T. Zijlstra, A. M. Baryshev, F. P. Mena, and T. M. Klapwijk  
*Optimizing superconducting matching circuits for Nb SIS mixers operating around the gap frequency*  
IEEE Transactions on Applied Superconductivity, Vol. **17**, 375 (2007).
6. E. Onac, F. Balestro, B. Trauzettel, C. F. J. Lodewijk, and L. P. Kouwenhoven  
*Shot-noise detection in a carbon nanotube quantum dot*  
Physical Review Letters, Vol. **96**, 026803 (2006).



## List of conference papers

1. C. F. J. Lodewijk, E. van Zeijl, T. Zijlstra, D. N. Loudkov, F. P. Mena, A. M. Baryshev, and T. M. Klapwijk  
*Bandwidth of Nb/AlN/Nb SIS mixers suitable for frequencies around 700 GHz*  
To appear in Proceedings of the 19th International Symposium on Space Terahertz Technology (2008).
2. J. Bout, A. Baryshev, F. P. Mena, R. Hesper, B. Jackson, W. Wild, C. F. J. Lodewijk, D. Ludkov, T. Zijlstra, E. van Zeijl, T. M. Klapwijk  
*AlN barrier junctions in submm heterodyne receiver: operational aspects*  
To appear in Proceedings of the 19th International Symposium on Space Terahertz Technology (2008).
3. A. Baryshev, F. P. Mena, J. Adema, R. Hesper, B. Jackson, G. Gerlofsma, M. Bekema, K. Keizer, H. Schaeffer, J. Barkhof, C. F. J. Lodewijk, D. Ludkov, T. Zijlstra, E. van Zeijl, T. M. Klapwijk, and W. Wild  
*ALMA Band 9 cartridge*  
To appear in Proceedings of the 19th International Symposium on Space Terahertz Technology (2008).
4. F. P. Mena, J. Kooi, A. M. Baryshev, C. F. J. Lodewijk, T. M. Klapwijk, and W. Wild  
*RF Performance of a 600 - 720 GHz sideband-separating mixer with all-copper micromachined waveguide mixer block*  
To appear in Proceedings of the 19th International Symposium on Space Terahertz Technology (2008).
5. C. F. J. Lodewijk, T. Zijlstra, D. N. Loudkov, T. M. Klapwijk, F. P. Mena, and A. M. Baryshev  
*Wideband AlN-based SIS devices for frequencies around 700 GHz*  
Proceedings of the 18th International Symposium on Space Terahertz Technology, Ed. A. Karpov, 256 (2007).

6. A. M. Baryshev, R. Hesper, F. P. Mena, B. D. Jackson, J. Adema, J. Barkhof, W. Wild, M. Candotti, M. Whale, C. Lodewijk, D. Loudkov, T. Zijlstra, and T. M. Klapwijk  
*Performance of ALMA band 9 receiver series*  
Proceedings of the 18th International Symposium on Space Terahertz Technology, Ed. A. Karpov, 164 (2007).
7. A. M. Baryshev, F. P. Mena, R. Hesper, C. F. J. Lodewijk, D. N. Loudkov, and T. M. Klapwijk  
*Measurement of in-RF and out-RF band saturation of SIS mixer*  
Proceedings of the 18th International Symposium on Space Terahertz Technology, Ed. A. Karpov, 160 (2007).
8. T. Zijlstra, C. F. J. Lodewijk, D. N. Loudkov, and T. M. Klapwijk  
*High current-density aluminum-nitride tunnel barriers grown by plasma nitridation from a remote plasma source*  
Proceedings of the 18th International Symposium on Space Terahertz Technology, Ed. A. Karpov, 113 (2007).
9. F. P. Mena, J. Kooi, A. M. Baryshev, C. F. J. Lodewijk, T. M. Klapwijk, R. Hesper, and W. Wild  
*Construction and characterization of a sideband-separating heterodyne mixer for band 9 of ALMA*  
Proceedings of the 18th International Symposium on Space Terahertz Technology, Ed. A. Karpov, 39 (2007).
10. A. M. Baryshev, F. P. Mena, R. Hesper, T. Zijlstra, C. F. J. Lodewijk, W. Wild, and T. M. Klapwijk  
*A waveguide NbTiN SIS mixer for THz array applications*  
Joint 31st International Conference on Infrared and Millimeter Waves and 14th International Conference on Terahertz Electronics, 392 (2006).
11. F. P. Mena, A. M. Baryshev, J. Kooi, C. F. J. Lodewijk, G. Gerlof-sma, R. Hesper, and W. Wild  
*Side-band-separating heterodyne mixer for band 9 of ALMA*  
Joint 31st International Conference on Infrared and Millimeter Waves and 14th International Conference on Terahertz Electronics, 522 (2006).
12. A. M. Baryshev, R. Hesper, F. P. Mena, B. D. Jackson, J. Adema, H. Schaeffer, J. Barkhof, W. Wild, M. Candotti, C. Lodewijk, D. Loudkov, T. Zijlstra, O. Noroozian, and T. M. Klapwijk  
*Design and development of a 600-720 GHz receiver for ALMA Band 9*  
Proceedings of the 17th International Symposium on Space Terahertz Technology, Eds. A. Maestrini and G. Beaudin, 89 (2006).

- 
13. F. P. Mena, A. M. Baryshev, J. Kooi, G. Gerlofsma, C. F. J. Lodewijk, R. Hesper, and W. Wild  
*Side-band-separating heterodyne mixer for band 9 of ALMA*  
Proceedings of the 17th International Symposium on Space Terahertz Technology, Eds. A. Maestrini and G. Beaudin, 40 (2006).
  14. A. M. Baryshev, R. Hesper, B. D. Jackson, P. Mena, J. Barkhof, T. Zijlstra, C. Lodewijk, G. Gerlofsma, J. Adema, R. Rivas, K. Keizer, M. Bekema, A. Koops, W. Wild, and T. M. Klapwijk  
*Design and performance of the 600-720 GHz ALMA band 9 Cartridge*  
Joint 30th International Conference on Infrared and Millimeter Waves and 13th International Conference on Terahertz Electronics, Vol. **1**, 70 (2005).
  15. A. M. Baryshev, J. Kooi, F. P. Mena, C. F. J. Lodewijk, and W. Wild  
*Design of a side-band-separating heterodyne mixer for band 9 of ALMA*  
Joint 30th International Conference on Infrared and Millimeter Waves and 13th International Conference on Terahertz Electronics, Vol. **2**, 463, (2005).
  16. C. F. J. Lodewijk, M. Kroug, T. M. Klapwijk, F. P. Mena, A. M. Baryshev, and W. Wild  
*Improved design for low noise Nb SIS devices for Band 9 of ALMA (600 - 720 GHz)*  
Proceedings of the 16th International Symposium on Space Terahertz Technology, Eds. M. Ingvarson, J. Stake, and H. Merkel, 42 (2005).
  17. F. P. Mena, J. Kooi, A. M. Baryshev, C. F. J. Lodewijk, and W. Wild  
*Design of a side-band-separating heterodyne mixer for band 9 of ALMA*  
Proceedings of the 16th International Symposium on Space Terahertz Technology, Eds. M. Ingvarson, J. Stake and H. Merkel, 191 (2005).





*'k Vind het prachtig dat u iets gelooft  
Wat door een man van vroeger is beloofd  
Maar u leest zo slecht*  
T. Acda and P. de Munnik, 2002.

*You can't always get what you want,  
But if you try sometime, yeah,  
You just might find you get what you need!*  
M. Jagger and K. Richards, 1969.

*Nightswimming deserves a quiet night  
I'm not sure all these people understand*  
B. Berry, P. Buck, M. Mills, and M. Stipe, 1992.



